**SANDIA REPORT**
SAND2001-8099
Unlimited Release
Printed December 2000

# Physics-based Modeling of Brittle Fracture: Cohesive Formulations and the Application of Meshfree Methods

P. A. Klein, J. W. Foulk, E. P. Chen, S. A. Wimmer, and H. Gao

Prepared by
Sandia National Laboratories
Albuquerque, New Mexico 87185 and Livermore, California 94550

Sandia is a multiprogram laboratory operated by Sandia Corporation, a Lockheed Martin Company, for the United States Department of Energy under Contract DE-AC04-94AL85000.



Sandia National Laboratories

Issued by Sandia National Laboratories, operated for the United States Department of Energy by Sandia Corporation.



Available to DOE and DOE contractors from
U.S. Department of Energy
Office of Scientific and Technical Information
P.O. Box 62
Oak Ridge, TN 37831

Telephone: (865)576-8401
Facsimile: (865)576-5728
E-Mail: reports@adonis.osti.gov
Online ordering: http://www.doe.gov/bridge

Available to the public from
U.S. Department of Commerce
National Technical Information Service
5285 Port Royal Rd
Springfield, VA 22161

Telephone: (800)553-6847
Facsimile: (703)605-6900
E-Mail: orders@ntis.fedworld.gov
Online order: http://www.ntis.gov/ordering.htm

SAND2001-8099
Unlimited Release
Printed December 2000

# Physics-based modeling of brittle fracture: cohesive formulations and the application of meshfree methods

P.A. Klein J.W. Foulk E.P. Chen
Science-based Materials Modeling Department
Sandia National Laboratories
P.O. Box 0969
Livermore, CA 94551

S.A. Wimmer
Multifunctional Materials Branch
Naval Research Laboratory
4555 Overlook Avenue SW
Washington, DC 20375-5343

H. Gao
Division of Mechanics and Computation
Department of Mechanical Engineering
Stanford University
Stanford, CA 94305

**Abstract**

Simulation of generalized fracture and fragmentation remains an ongoing challenge in computational fracture mechanics. There are difficulties associated not only with the formulation of physically-based models of material failure, but also with the numerical methods required to treat geometries that change in time. The issue of fracture criteria is addressed in this work through a cohesive view of material, meaning that a finite material strength and work to fracture are included in the material description. In this study, we present both surface and bulk cohesive formulations for modeling brittle fracture, detailing the derivation of the formulations, fitting relations, and providing a critical assessment of their capabilities in numerical simulations of fracture. Due to their inherent adaptivity and robustness under severe deformation, meshfree methods are especially well-suited to modeling fracture behavior. We describe the application of meshfree methods to both bulk and surface approaches to cohesive modeling. We present numerical examples highlighting the capabilities and shortcomings of the methods in order to identify which approaches are best-suited to modeling different types of fracture phenomena.

**Keywords:** finite element method, fracture mechanics, cohesive modeling, meshfree methods.

# Contents

## List of Figures

# 1 Introduction

Classical approaches to fracture mechanics are limited because they lack a physics-based description of the failure process. In this report, we refer to approaches based on linear elastic fracture mechanics (LEFM) as "classical" although the point singularity model of the crack tip originally proposed in 1920 by Griffith[37] precedes the earliest cohesive studies of fracture by only a few years. Regardless of the age of the two approaches, LEFM is certainly classical in the sense that it relies on material behavior that is linear to within distances from the crack tip at which the characteristic tip singularity dominates the stress and strain fields. As such, all contributions to the fracture energy are represented with single parameter, typically expressed as a critical stress intensity factor or energy release rate. These failure criteria are phenomenological, and any dependence of the failure criterion on effects like the near tip stress state or loading rate must also be incorporated in a phenomenological way. Under many conditions, an energy release rate can be difficult to calculate or can become poorly defined as the zone of material exhibiting inelastic response grows. With classical approaches, behavior as fundamental as the crack propagation direction must be selected, or imposed, based on *ad hoc* assumptions. Moreover, the fracture path instabilities observed during dynamic propagation of cracks are among the phenomena that have not yet been thoroughly explained, making formulation of a phenomenological crack tip model impossible. Finally, classical approaches require pre-existing, crack-like flaws. The nucleation of these flaws cannot be treated directly.

A cohesive view of material addresses these shortcomings by incorporating a cohesive strength and finite work to fracture in the description of material behavior itself. Introducing the essential physics of the fracture process has the promise of resulting in simulation methods in which fracture occurs "criteria free". Fracture develops as a natural part of the solution of initial/boundary value problems, and the fracture path and speed are an outcome of the simulations, not predefined simulation parameters. At the same time, cohesive approaches complicate the simulation of fracture because a physics-based approach implies some physics-based understanding and characterization of the fracture process zone. Depending on the material system, the fracture processes may be numerous and complicated. The only character of cohesive zone behavior that seems common across various failure modes is that these process zones are small, from near the angstrom length scale in ideally brittle crystals to the micron scale in polymers. This inherently small scale of the fracture processes implies considerable computational effort is required for even academic simulations of fracture. For this work, we will consider only brittle fracture, which we define to mean that all dissipation during the fracture process is associated directly with the creation of new free surfaces. The bulk material does not exhibit any rate or history dependence. This definition does not restrict our study to small strains. All of the approaches in this work are generalized to finite strains.

The goal of this work is to compare several cohesive approaches to modeling fracture that have been proposed recently, cohesive surface formulations and a bulk cohesive formulation. For each approach, we briefly outline the underlying theory. However, our focus is on the capabilities, shortcomings, and applicability of each approach to modeling different aspects of fracture behavior. This report also provides a guide for selecting the model parameters to represent specific materials. A portion of this report focuses on numerical and implementation issues. In particular, we will focus on the application of so-called "meshfree methods" to the simulation of fracture. In themselves, these methods do not provide phenomenological or physical theories of fracture. Instead, the methods prove useful because they have a number of advantages over traditional finite element

methods in treating problems for which geometry of the simulation domain changes with time.

## 1.1 Background

Although the cohesive zone approach to modeling fracture has recently become a very active area of research, the basic ideas behind the approach were established some time ago. As early as 1933, Prandtl[72] employed a cohesive traction relation to predict the length of debonded zone between two slender beams. Barenblatt[6] proposed a cohesive zone model that accounted for finite strength in the interaction forces between atoms near a crack tip. Dugdale[24] used a similar cohesive model to treat yielding in a plastic strip in front of a crack tip. Willis[93] considered a cohesive force zone in front of a dynamically propagating crack. So-called "nodal release" methods for modeling fracture by splitting nodes along the fracture path within a finite element setting also appeared more than twenty years ago[44, 49, 82]. More recently, these methods have evolved into approaches for which cohesive surfaces are introduced adaptively along element interfaces. Ortiz *et al.* have used an adaptive approach for a variety of simulations of dynamic fracture and fragmentation in both two[15, 16] and three[70, 81] dimensions. Use of a network cohesive surfaces for simulating generalized fracture within a finite element setting was pioneered by Xu and Needleman[95, 96]. In their oft-cited work, they formulate the integration of the contributions from a network of cohesive surfaces to the statement of virtual work. They also present a mixed-mode traction-separation relationship that has been widely used in the study of brittle fracture. In their work[95], they demonstrate that the method is capable of qualitatively reproducing aspects of dynamic fracture, such as crack tip instabilities and branching.

This work is not intended as a comparison of cohesive surface constitutive models. In focusing on the general capabilities of modeling fracture with cohesive surfaces, we consider only rate-independent models. However, we do acknowledge that a growing body of literature is devoted to incorporating additional effects. The cohesive relation proposed by Xu and Needleman does not account for rate effects in the fracture process. Although much research has focused on modeling the rate effects in the bulk behavior of materials, fewer works have addressed rate effects in cohesive crack growth. Knauss and Losi[48] proposed a rate-dependent cohesive surface relation incorporating viscoelasticity and damage. In addition, Knauss[48] addressed crazing in thermoplastic polymers within the context of the model. Yoon and Allen[98] proposed a cohesive relation in the form of a single hereditary integral for a linear viscoelastic material. The model relies on an internal state variable which reflects the damage state of the cohesive zone. Other rate-dependent models have been proposed by Rahul-Kumar *et al.* [73], Costanzo and Walton[22], and Lee and Prakash[53].

In all the examples cited thus far, the cohesive view of material is captured by surface constitutive relations that describe the evolution of tractions generated across the faces of a crack as a function of the opening displacements. In contrast to these approaches, a virtual internal bond (VIB) model[34] with randomized cohesive interactions between material particles has been proposed as an integration of continuum models with cohesive surfaces and atomistic models with interatomic bonding. This approach differs from an atomistic model in that a phenomenological "cohesive force law" is assumed to act between "material particles" which are not necessarily atoms. It also differs from a cohesive surface model in that, rather than imposing a cohesive law along a prescribed set of discrete surfaces, a randomized network of cohesive bonds is statistically incorporated into the constitutive response of the material via the Cauchy-Born rule, by equating

the strain energy function on the continuum level to the potential energy stored in the cohesive bonds due to an imposed deformation. The approach could be viewed as an attempt to provide a more physical basis for the hyperelastic constitutive laws used in finite strain continuum mechanics. Although the model presently suffers from a lack of regularization for the localized modes that appear, simulations using the model have produced new insights into the origin of crack tip instabilities and branching[47].

## 1.2 Overview of cohesive approaches

Section 1 mentions cohesive surface approaches both in terms of adaptively inserted surfaces and a network of surfaces active, or present, in the initial geometry. The surface approaches differ not only in implementation, but also in the view each takes of the cohesive failure process. These surface approaches, as well as the bulk cohesive approach represented by the VIB model, can be compared by considering how each treats the progression of failure. We divide the failure process into four stages, as illustrated in Figure 1.1. The location of material at the four stages is indicated

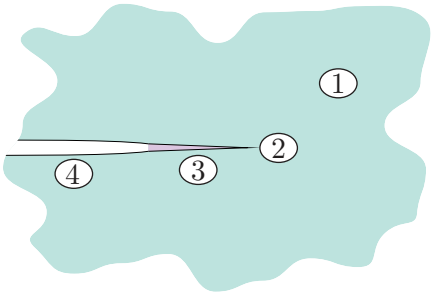


Figure 1.1: A four stage view of modeling failure with markers (1) through (4) denoting the location of each stage around a moving crack tip.

with markers in the figure. In summary, the four stages represent:

(1) Smooth field, or regular part, of the material response.

(2) Initiation, or first appearance, of the localized deformation mode.

(3) Evolution of the failure mode from initiation to complete failure.

(4) Complete failure and the appearance of new free surfaces.

For each stage, a modeling approach must determine the constitutive relations governing the response of the material as well as the conditions that mark the transition to the next stage. Stage 2 is actually a transition state, but is considered separately here because it represents a marked change in the behavior of the material. The approaches to modeling fracture considered in this report show different strengths within each stage and in transitions between stages. Stage 1 requires accurate representation of regular deformations. Since most of the approaches have developed as enhancements to solving smooth field problems, this stage usually does not present any difficulties. Moreover, the incorporation of a finite material strength should in principle remove the burden of resolving the singular fields associated with linear elastic fracture mechanics. However, difficulties with this stage do arise with the cohesive surface network approach. The active network introduces

fictitious compliance that results in a pathological mesh dependence. Section 2.1.3 presents a more detailed analysis of this problem. It is also worthwhile to remark that molecular dynamics fails to be a practical method for the analysis of fracture behavior because of difficulties associated with treating stage 1. Molecular dynamics does serve as a model technique for simulating complicated material behavior. Once the parameters of the interatomic force laws have been determined, stages 1 through 4 occur without any additional theoretical assumptions or implementation details. Any number of deformation processes arise and evolve through the course of a simulation.

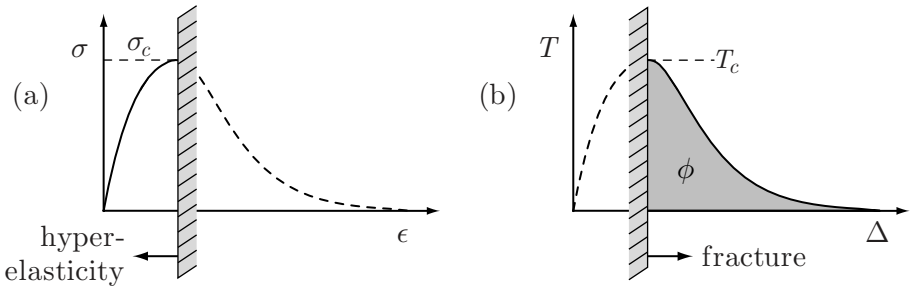


Figure 1.2: Constitutive relations in cohesive modeling of failure represented by (a) $\sigma(\epsilon)$ for stage 1 and (b) $T(\Delta)$ for stage 2.

Stage 2 is the transition from smooth to localized modes of deformation. This stage represents a bifurcation point in the material behavior, a point after which an intrinsic material length scale emerges. Section A.3 discusses how this point may be identified under multidimensional states of deformation at finite strains for a hyperelastic material. In one dimension, the bifurcation occurs at the point of a horizontal tangent on the "stress-strain" curve, identified with $\sigma_c$ in Figure 1.2 (a). Beyond the bifurcation point, the "softening" portion of the stress response is an instability that localizes deformation to a length scale determine by the material. The dissipation associated with fracture occurs within this localized zone. For the case of brittle fracture, the material outside of the zone unloads reversibly. One approach to treating this localized mode is to assume that the zone shrinks to a width of zero measure. At this limit, the constitutive response of the mode is described by a traction-separation relation, shown as $T(\Delta)$ in Figure 1.2 (b). This approximation is the basis for cohesive surface approaches to predicting stage 3 behavior. Section 2.1.2 describes a number of cohesive surface relations. The validity of this assumption depends on how this intrinsic material scale compares with other relevant length scales, whether from the geometry or the application of loading. The VIB model produces a stress response with continuously reducing stiffness leading to a bifurcation representative of a randomized network of cohesive bonds, as depicted in one dimension by Figure 1.2 (a). The authors are unaware of any other bulk constitutive models that display the same behavior. Therefore, if the hyperelastic response for stage 1 is derived from strictly polyconvex strain energy potentials, the transition point at stage 2 must be chosen by assumption. We might assume that the localized failure mode appears at a critical hoop stress, traction, or strain energy density. The choice of initiation criterion will determine the crack propagation direction as well as the appearance of any branching phenomenon. The effect of stage 2 parameters for adaptive insertion of cohesive surfaces is investigated in the calculations presented in Section 4.4. An adaptive approach with an arbitrarily selected stage 2 initiation condition allows bulk and surface constitutive models to be selected nearly independent of each other. The disadvantage of this approach is that fracture behavior, which we intended to model "criteria free" by incorporating

a cohesive view, becomes strongly dependent on our choice of the failure initiation condition. With standard finite element methods, element boundaries are the natural location for the insertion of cohesive surfaces. This constraint leads to a mesh dependence that we have tried to address with the incorporation of meshfree methods.

In reality, materials do not exhibit "perfect localization". This difference is illustrated in Fig-

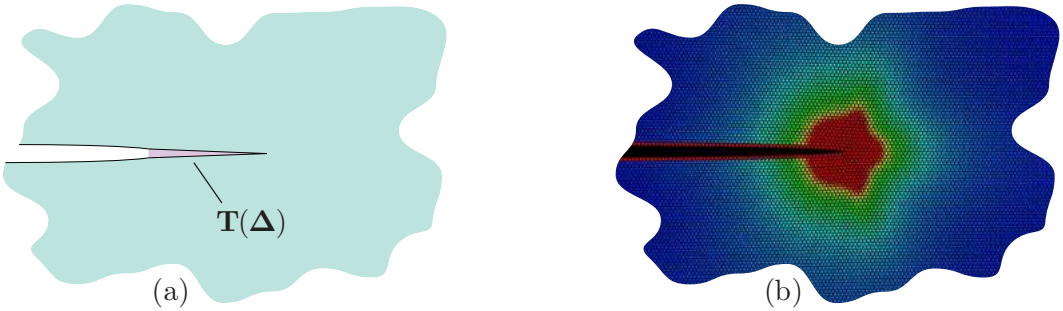


Figure 1.3: Cohesive crack tips: (a) cohesive zone model characterized by a traction-separation relations $\mathbf{T}(\boldsymbol{\Delta})$ and (b) atomistic view of higher-order displacement gradients motivating a nonlocal continuum approach.

ures 1.3 (a) and (b). With cohesive surface approaches, all fracture processes act only across a surface. Figure 1.3 (b) shows the norm of the higher-order gradient of the displacement field $\sqrt{u_{i,jk}\, u_{i,jk}}$ around a crack tip subject to mode I loading in a two-dimensional, triangular lattice under the influence of a simple pair potential. Though not representative of any real material, this atomistic model provides a detailed view of the tip displacement fields resulting from highly nonlinear and nonlocal interactions that is difficult to obtain by other means. Higher-order displacement gradient dependencies introduce an intrinsic length scale, regularizing the localized mode. The figure illustrates that the regularization acts not only across the fracture surface, but in region surrounding the crack tip. In a sense, the region closest to the tip acts as a cohesive volume where dissipation mechanisms associated with fracture are active. This difference may prove important in modeling fracture in microsystems since the overall dimensions of the structures are very small. More importantly, a cohesive bulk constitutive model incorporating higher-order gradient regularization passes from stage 1 to stage 3 without requiring numerical procedures to pinpoint the transition state, stage 2. Issues associated with actively tracking fracture surfaces are eliminated.

The current form of the VIB model described in Section 2.2 lacks regularization leading to a pathological mesh dependence in the localized mode. We have begun development of a higher-order gradient, regularizing enhancement to the VIB model[35]; however, the work is still in its preliminary stages. Despite the lack of regularization, the model does allow us to study the effects of nonlinear continuum response under conditions of dynamic fracture in brittle materials that are unavailable with any other approach. As alluded to above, we have also begun to investigate the application of the VIB model in an adaptive cohesive surface approach. As depicted in Figure 1.2, the cohesive bulk response (a) complements the cohesive surface response (b) in that the former is not valid after the bifurcation point marked by $\sigma_c$ while the latter is invalid before it.

The cohesive surface network also avoids the issue of selecting and tracking a stage 2, failure initiation condition by making the entire network active in the initial geometry. Of the approaches

considered in this report, the cohesive surface network approach is linked most directly to the finite element method: all element interfaces are bound together with cohesive tractions. In principle, the bulk constitutive models govern stage 1 deformations while the surface constitutive models govern the stage 3 behavior. In reality, the response for stages 1, 2, and 3 are a composite of the bulk and surface models. The composite behavior presents problems for two reasons. First, the effective response is difficult to predict. In Section 2.1.3, we derive the effective modulus for a one-dimensional cohesive surface network in the undeformed state. Calculating the effective modulus for a multidimensional network subject to general states of deformation would be considerably more difficult. Second, the effective properties of the network are mesh dependent, changing as a function of mesh design and element size. As described in Section 4.3, we are unable to produce convergent results for mixed-mode fracture simulations using the cohesive surface network approach though others have produced more promising results for modeling fracture in ductile materials[83], assuming that the cohesive strength is very low.

From a practical point of view, the insertion of a cohesive surface network results in a considerable increase in the model size. Although sometimes termed "double-noding" of the mesh, the number of "duplicates" needed for every node depends on the topology of the mesh. A separate node is needed for every bulk element that converges on a particular vertex of the mesh. For a regular mesh of quadrilateral elements, the number of nodes increases by a factor of four. A regular mesh of equilateral triangles sees an increase of six. The factor of increase tends to become larger as the number of spatial dimensions increases. A regular mesh of hexahedral elements sees an increase of eight, while a mesh of tetrahedral elements could see an increase of a factor of twelve or more.

This report does not address issues associated with treating stage 4, interactions between newly created free surfaces. Fracture surface interactions would be expected under mixed-mode loading conditions without a strong opening component or under conditions of extensive fragmentation. In this report, we have limited our examples to cases for which the opening mode displacements avoids contact between the crack faces. Cohesive surface elements within a standard finite element framework coincide with element boundaries, so fracture leaves behind a well-defined surface geometry where traditional methods for enforcing contact constraints may be applied. Issues arising from inserting cohesive surfaces in a meshfree domain are discussed in Section 3.3. Although the representation of the displacement field is different when using meshfree methods, traditional approaches for enforcing contact constraints should be applicable with some modifications. With bulk cohesive approaches, fracture runs through the elements, not between them. Within a finite element framework, some additional implementation details would need to be addressed to construct a representation of the free surface along the fracture path. With meshfree methods, this construction is admitted naturally.

## 1.3 Role of meshfree methods in cohesive modeling

Notably, none of the approaches mentioned in Section 1.2 are based explicitly on meshfree methods. Meshfree methods do not in themselves provide theories of material behavior or fracture. They simply provide a representation for the unknown fields based solely on nodal information, rather than element-based constructions provided by standard finite element methods. However, meshfree methods do possess a number of properties that make them especially well-suited for modeling fracture and fragmentation. Section 3 describes the meshfree formulations used for this study. This study is not intended to provide a comprehensive review of the state of the art in meshfree

methods. The attributes we identify as reasons for considering meshfree methods to model fracture are as follows:

(1) **Natural adaptivity.** With standard finite element techniques, the nodal shape functions and therefore the representation of the displacement field is defined over subdomains, or elements, with a pre-defined geometries and nodal topologies. Since cracks produce discontinuities in the displacement field, they must be explicitly represented in the computational mesh. With meshfree methods, the representation of the displacement field is based only on local collections of nodes. The set of nodes used to construct the displacement field at any point may contain an arbitrary number of nodes; moreover, this set may be modified to exclude nodes falling across a line of discontinuity. In this way, evolving discontinuities can be naturally embedded in the displacement field. Furthermore, $h$ refinement can be implemented by "sprinkling" more particles in the region needing higher resolution while $p$-like refinement is available through local modifications to the parameters of the nodal shape functions[57, 55].

(2) **Reduced "texture bias".** Ideally, numerical results should show little effects of discretization. In practice, numerical methods can never be entirely free from discretization effects even though the formulations are convergent. This observation is especially true in situations involving bifurcations. The appearance of cracks may be viewed as a bifurcation. Since the support of the nodal shape functions with meshfree methods can be selected to be isotropic, circular in two dimensions and spherical in three dimensions, simulations of localized modes of deformation have a reduced tendency to follow the "texture" of the spatial discretization[54]. Furthermore, cracks, or other discontinuities in the displacement field, are not restricted to propagate along element boundaries.

(3) **Improved robustness under large deformations.** Under large deformations, standard finite elements may become twisted or inverted. These deformations are physically inadmissible. However, certain representations of the displacement field are more susceptible to introducing these errors in the mapping from the reference to the deformed configuration. Due to the more diffuse, or non-local, character of the meshfree shape functions, they display a higher resistance against errors of this type[17, 60].

(4) **Smoothness.** With the recent interest in the simulation of localized deformation and deformation in very small structures, nonlocal constitutive models have re-emerged as an active area of research. Many of these models introduce intrinsic material length scales through the use of strain gradients or gradients in the deformation gradient. Models of this type require representations of the displacement field that are at least $C^1$ in order to produce convergent results. Standard finite element approximations to the displacement field are $C^0$. Higher-order finite elements are smoother on the element interiors, but are still $C^0$ across element interfaces. $C^1$ approximations of the displacement field have been constructed in two dimensions under the assumption of infinitesimal strains[94] through the introduction of rotational degrees of freedom for every node. However, the approach introduces a large number of degrees of freedom, requires reformulation for application to three-dimensional problems, and has not been developed for the case of finite strains. With meshfree methods, the displacement field can be constructed to be arbitrarily smooth. Higher-order gradients of the displacement field follow from simple differentiation of the expressions for the nodal shape functions. The $C^k$ representation of the displacement field allows construction of a

strictly displacement-based implementation for higher-order gradient theories, even at finite deformations.

(5) **Inherent multiscale capability (RKPM).** The Reproducing Kernel Particle Method (RKPM) is formulated within the framework of wavelet theory. As a result, the method can make use of the multi-resolution character of wavelets to produce a hierarchical, multiscale solution[57, 59]. We have not taken advantage of these feature of RKPM. However, the capability for assigning different constitutive behavior to displacement field features with different characteristic length scales appears to be a very promising approach for simulating fracture and other forms of highly localized deformation[61].

Researchers in the meshfree community often cite other advantages of meshfree methods that we consider secondary in the study of fracture. The lack of a mesh is omitted from the list above because our current implementation makes use of a background grid to integrate the weak form of the governing equations. Implementations of this type are sometimes referred to as "semi-meshfree". We use standard mesh generation tools to create the integration grids for our calculations. The need for this background grid can be removed with the move to node-based integration schemes. A number of these have already been developed[8, 19, 18], and this area remains an active topic of research. Methods making use of nodal integration schemes are often referred to as "truly meshfree". We do not find this distinction useful because the properties of the shape functions and the list of advantages given above is the same regardless of the integration scheme used. Our experience with meshfree methods indicates that they work most-efficiently when the node, or particle, distribution is uniform or varying smoothly. For highly irregular particle distributions, we find that the number of particles contributing to the field at any point must generally increase in order to insure that all points in the domain are sufficiently covered. Moreover, we have not studied effect of particle distribution on numerical errors; however, Dolbow and Belytschko[23] have shown that integration errors grow with grid-based integration schemes as the particle spacing becomes highly irregular. The proposed nodal integration schemes of Chen *et al.* [19, 18] display accuracy that appears less sensitive to particle distribution than grid-based integration. For complicated geometries or situations for which the particle distribution needs to be carefully controlled, software for generating high quality finite element meshes represent the best tools for producing regular or smoothly varying particle distributions.

Of the modeling approaches described in Section 1.2, only the cohesive surface network approach is intimately linked to the finite element method. Certainly, a network of cohesive surfaces could be introduced into the initial state of a meshfree domain, but this would fail to take advantage of the inherent adaptivity provided by meshfree methods. In this study, the network approach is not used with meshfree methods. Meshfree methods are used as an integral part of the adaptive approach with cohesive surfaces. The implementation of this procedure is discussed in Section 3.4. Adaptive approaches to modeling fracture may also be implemented using standard finite element methods; however, these are not considered here because of the difficulty associated with modifying the mesh topology to account for growing cracks. Finally, the VIB model is a bulk constitutive model that can be used with standard finite element methods as well as with meshfree methods. In this study, we use the model with meshfree methods because they display less "texture bias" and because of their robustness under conditions of dynamic fracture.

## 1.4 Outline of this report

The remainder of this report proceeds in the following order. We describe the surface and bulk cohesive formulations in detail in Section 2. Section 2.1.1 describes the element level equations associated with cohesive surfaces. Section 2.1.2 presents several rate-independent cohesive surface relations. Sections 2.1.3 and 2.1.4 provide an analysis of the mesh dependencies that arise with the cohesive surface network approach. Section 2.2 describes the Virtual Internal Bond (VIB) model, an attempt to embed cohesive behavior within a bulk constitutive model. Sections 2.2.1 , 2.2.3, and 2.2.4 describe how the VIB model parameters can be selected to exhibit particular material behavior. Section 3 describes the meshfree formulations studied in this report. In particular, Section 3.3 describes the changes needed to the standard formulation of cohesive surface elements for application to a meshfree domain. The implementation of adaptively inserted cohesive surfaces in a meshfree domain is described in Section 3.4. Section 4 presents four numerical studies of modeling fracture with cohesive approaches. Section 4.1 studies the source of numerical errors in cohesive modeling with simulations of fracture in a double-cantilever beam specimen. In Section 4.2, three-dimensional peel simulations in mica are compared with experimental observations. Section 4.3 investigates the reliability of cohesive approaches for modeling generalized fracture under dynamic conditions for mixed-mode loadings. Section 4.4 studies the behavior of the various cohesive approaches under conditions for which the crack propagates at its terminal velocity. A summary and topics for ongoing development are presented in Sections 5 and 6, respectively. Finally, Section A provides supporting discussion on the kinematics of large deformations, Green elastic theory of hyperelastic materials, and presents the governing equations of elastodynamics solved for the numerical examples.

# 2 Cohesive formulations

In this section, we present the formulations of both surface and bulk cohesive models. The description of the surface models includes the development of the element level relations as well as an overview of the cohesive surface relations used in this study. We also discuss the origin of numerical artifacts arising from the application of the surface formulation with a network approach. The description of the bulk cohesive model covers only the development of the constitutive relations. We also outline some analysis of the model response that is needed to fit the model parameters to particular material behavior.

## 2.1 Cohesive surface formulation

The description of the cohesive surface formulation is presented in two parts. First, we present the expressions element force vector and its consistent tangent stiffness. This element formulation allows all constitutive behavior to be evaluated in an local coordinate frame defined with respect to the deforming surface facets. The following section describes the rate-independent cohesive models used for the numerical examples presented in this study.

### 2.1.1 Element formulation

At every point along a cohesive surface, we define a local coordinate frame which resolves the opening displacements across the surface into normal and shear components. As shown in Figure 2.1, this coordinate frame is not uniquely defined for finite deformations. We choose to define

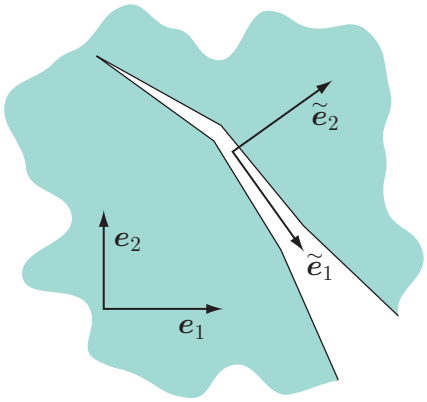


Figure 2.1: Local coordinate frame $\tilde{\mathbf{e}}_i$ constructed along the surface where $\mathbf{e}_i$ is the global cartesian frame.

this coordinate system with respect to the mid-plane between the displaced surfaces. Alternately, this frame may be fixed to the upper or lower facet. The discussion that follows is independent of the particular choice of local coordinate system though we present specific expressions for the mid-plane. Let the transformation of the gap vector from its representation in the global coordinate frame $\boldsymbol{\Delta}$ to its local representation $\tilde{\boldsymbol{\Delta}}$ in a frame defined with respect to the cohesive surface be given by

$$\tilde{\boldsymbol{\Delta}} = \mathbf{Q}^{\mathrm{T}}\,\boldsymbol{\Delta}. \tag{2.1}$$

The transformation resolves the opening displacement into normal and shear components relative to the current orientation of the surface. This distinction allows for the definition of mixed-mode, surface constitutive relations that show a dependence on the character of the opening displacement. In a variational setting, the contribution to the virtual work from cohesive surface elements is

$$\delta w^{\text{CSE}} = \int_{\Gamma_0} \mathbf{T} \cdot \delta \boldsymbol{\Delta} \, d\Gamma, \tag{2.2}$$

where the integration domain $\Gamma_0$ is defined in the undeformed configuration and $\delta\boldsymbol{\Delta}$ is the variation in the surface opening displacement. We review the formulation of several surface constitutive models in Section 2.1.2. The discussion that follows applies to all displacement-driven cohesive relations $\tilde{\mathbf{T}}(\tilde{\boldsymbol{\Delta}})$ defined in the local surface frame. From (2.1), the traction in the global coordinate frame is given by the transformation

$$\mathbf{T} = \mathbf{Q}\,\tilde{\mathbf{T}}. \tag{2.3}$$

With these preliminaries, we derive the expressions for the element level nodal force and stiffness contributions arising from discretization of the cohesive surfaces. Assuming the displacement field is expressed in terms of an expansion of nodal values and shape functions, the opening displacement vector may be written as

$$\begin{aligned} \boldsymbol{\Delta}(\boldsymbol{\xi}) &= \mathbf{u}^+(\boldsymbol{\xi}) - \mathbf{u}^-(\boldsymbol{\xi}) \\ &= \sum_{A \in N^+} \Phi_A(\boldsymbol{\xi})\, \mathbf{u}_A - \sum_{A \in N^-} \Phi_A(\boldsymbol{\xi})\, \mathbf{u}_A, \end{aligned} \tag{2.4}$$

where $\mathbf{u}^+$ and $\mathbf{u}^-$ denote the displacement fields of the upper and lower surfaces, respectively, defined by sets of nodes $N^+$ and $N^-$, $\Phi_A$ is the shape function associated with local node $A$ on upper or lower surface, $\mathbf{u}_A$ is the nodal displacement, and $\boldsymbol{\xi}$ are coordinates parametrizing the surface. This expression for the opening displacement and the expressions for the nodal force and stiffness that follow are valid within a framework using standard finite element shape functions as well as a framework using meshfree shape functions. In terms of the variation in the nodal displacements $\mathbf{u}_A$, we can rewrite the work increment (2.2) as

$$\delta w_A^{\text{CSE}} = \mathbf{f}_A^{\text{CSE}} \cdot \delta \mathbf{u}_A, \tag{2.5}$$

where the components of the nodal force

$$f_{rA}^{\text{CSE}} = \int_{\Gamma_0} \frac{\partial \Delta_i}{\partial u_{rA}}\, Q_{ij}\, \tilde{T}_j \, d\Gamma \tag{2.6}$$

only receive contributions from cohesive surfaces that fall within the support of node $A$ and

$$\frac{\partial \Delta_i}{\partial u_{jA}} = \begin{cases} \frac{\partial \Phi_A}{\partial \xi}\, \delta_{ij} & \text{for } A \in N^+, \\ -\frac{\partial \Phi_A}{\partial \xi}\, \delta_{ij} & \text{for } A \in N^- \end{cases} \tag{2.7}$$

follows from the definition of the opening displacement (2.4).

The transformation to a representation of the displacement jump and tractions in a coordinate frame fixed to the current configuration of the surfaces is often neglected in an analog to small

strain bulk deformation. Though omitting this changing transformation reduces computational effort, the resulting nodal forces will be incorrect in situations for which the surfaces undergo appreciable reorientation due to local crack tip deformations or rigid rotations of the entire body. Tracking the current orientation of the surfaces adds relatively little complication of the element force vector, but produces a considerable increase in the complexity of the tangent stiffness. Not only does the transformation introduce additional contributions to the stiffness, but the resulting matrix is not symmetric.

The tangent stiffness matrix is derived from the linearization of (2.6) as

$$\delta \mathbf{f}_A^{\mathrm{CSE}} = \mathbf{K}_{AB}^{\mathrm{CSE}} \delta \mathbf{u}_B \tag{2.8}$$

where

$$\begin{aligned} \left[\mathbf{K}_{AB}^{\mathrm{CSE}}\right]_{rs} &= \frac{\partial f_{rA}^{\mathrm{CSE}}}{\partial u_{sB}} \\ &= \int_{\Gamma_0} \frac{\partial \Delta_i}{\partial u_{rA}} \left( \frac{\partial Q_{ij}}{\partial u_{sB}} \tilde{T}_j + Q_{ij} \frac{\partial \tilde{T}_j}{\partial \tilde{\Delta}_k} \frac{\partial \tilde{\Delta}_k}{\partial u_{sB}} \right) d\Gamma. \end{aligned} \tag{2.9}$$

From (2.1), we may write

$$\frac{\partial \tilde{\Delta}_i}{\partial u_{sA}} = \frac{\partial Q_{ji}}{\partial u_{sA}} \Delta_j + Q_{ji} \frac{\partial \Delta_j}{\partial u_{sA}}. \tag{2.10}$$

Substituting (2.10) into (2.9), the tangent may be expressed as

$$\begin{aligned} \left[\mathbf{K}_{AB}^{\mathrm{CSE}}\right]_{rs} = \int_{\Gamma_0} \Bigg( & \frac{\partial \Delta_p}{\partial u_{rA}} Q_{pi} \frac{\partial \tilde{T}_i}{\partial \tilde{\Delta}_j} Q_{qj} \frac{\partial \Delta_q}{\partial u_{sB}} \\ & + \frac{\partial \Delta_p}{\partial u_{rA}} Q_{pi} \frac{\partial \tilde{T}_i}{\partial \tilde{\Delta}_j} \frac{\partial Q_{qj}}{\partial u_{sB}} \Delta_q \\ & + \frac{\partial \Delta_i}{\partial u_{rA}} \frac{\partial Q_{ij}}{\partial u_{sB}} \tilde{T}_j \Bigg) \, d\Gamma. \end{aligned} \tag{2.11}$$

In order to complete the formulation of $\mathbf{K}_A^{\mathrm{CSE}}$, we need to derive an expression for the third-rank tensor $\frac{\partial \mathbf{Q}}{\partial \mathbf{u}_A}$. In two dimensions, the transformation tensor $\mathbf{Q}$ may be expanded as

$$Q_{ij}^{\mathrm{2D}} = \hat{t}_i \, \delta_{1j} + \hat{n}_i \, \delta_{2j}, \tag{2.12}$$

where the unit tangent direction in the deformed configuration

$$\hat{\mathbf{t}} = \frac{\mathbf{t}}{|\mathbf{t}|} \tag{2.13}$$

is defined from the jacobian of the surface parametrization

$$\mathbf{t}(\xi) = \frac{\partial \mathbf{x}(\xi)}{\partial \xi}. \tag{2.14}$$

The mid-plane surface is

$$\mathbf{x}(\xi) = \frac{1}{2}\left(\sum_{A\in N^+} \Phi_A(\xi)\ \mathbf{x}_A + \sum_{A\in N^-} \Phi_A(\xi)\ \mathbf{x}_A\right), \tag{2.15}$$

where the nodes on upper and lower facets of the element are denoted by $N^+$ and $N^-$ as in (2.4) and the current coordinates are defined with respect the undeformed coordinates $\mathbf{X}_A$ as

$$\mathbf{x}_A = \mathbf{X}_A + \mathbf{u}_A. \tag{2.16}$$

From (2.15), the tangent (2.14) may be expanded as

$$\mathbf{t}(\xi) = \frac{1}{2}\left(\sum_{A\in N^+} \frac{\partial \Phi_A}{\partial \xi}\,\mathbf{x}_A + \sum_{A\in N^-} \frac{\partial \Phi_A}{\partial \xi}\,\mathbf{x}_A\right). \tag{2.17}$$

The normal direction may be written as

$$\hat{\mathbf{n}} = \begin{bmatrix} 0 & -1 \\ 1 & 0 \end{bmatrix} \hat{\mathbf{t}} = \mathbf{Q}^{(\frac{\pi}{2})}\,\hat{\mathbf{t}}. \tag{2.18}$$

From (2.12) and (2.18), we can therefore express $\frac{\partial \mathbf{Q}}{\partial \mathbf{u}_A}$ needed in (2.11) for the two-dimensional case as

$$\frac{\partial Q^{\text{2D}}_{ij}}{\partial u_{kA}} = \frac{\partial \hat{t}_i}{\partial u_{kA}}\,\delta_{1j} + Q^{(\frac{\pi}{2})}_{ir}\,\frac{\partial \hat{t}_r}{\partial u_{kA}}\,\delta_{2j}, \tag{2.19}$$

where

$$\frac{\partial \hat{t}_i}{\partial u_{kA}} = \left[\frac{\partial}{\partial \mathbf{u}_A}\frac{\mathbf{t}}{|\mathbf{t}|}\right]_{ik} = \frac{1}{|\mathbf{t}|}\left(\frac{\partial t_i}{\partial u_{kA}} - \hat{t}_i\,\frac{\partial t_r}{\partial u_{kA}}\,\hat{t}_r\right). \tag{2.20}$$

The derivative of the tangent $\mathbf{t}$ follows from (2.17) as

$$\frac{\partial \mathbf{t}}{\partial \mathbf{u}_A} = \frac{1}{2}\,\frac{\partial \Phi_A}{\partial \xi}\,\mathbf{1}. \tag{2.21}$$

In three dimensions, the transformation tensor $\mathbf{Q}$ may be expanded as

$$Q^{\text{3D}}_{ij} = \hat{t}^{(1)}_i\,\delta_{1j} + \hat{t}^{(2)}_i\,\delta_{2j} + \hat{n}_i\,\delta_{3j}, \tag{2.22}$$

where the local normal direction $\hat{\mathbf{n}}$ and the two tangent directions $\hat{\mathbf{t}}^{(1)}$ and $\hat{\mathbf{t}}^{(2)}$ are defined using the parameterization of the surface with respect to $\boldsymbol{\xi} = [\xi\ \eta]^{\text{T}}$. At any point on the surface, two tangential, but not necessarily orthogonal, directions are defined by the columns of the surface jacobian

$$\mathbf{m}^{(1)}(\boldsymbol{\xi}) = \frac{\partial \mathbf{x}(\boldsymbol{\xi})}{\partial \xi} \qquad \text{and} \qquad \mathbf{m}^{(2)}(\boldsymbol{\xi}) = \frac{\partial \mathbf{x}(\boldsymbol{\xi})}{\partial \eta}. \tag{2.23}$$

Using the mid-plane construction, we can expand these tangent directions as

$$\mathbf{m}^{(1)}(\boldsymbol{\xi}) = \frac{1}{2}\left(\sum_{A\in N^+} \frac{\partial \Phi_A(\xi,\eta)}{\partial \xi}\,\mathbf{x}_A + \sum_{A\in N^-} \frac{\partial \Phi_A(\xi,\eta)}{\partial \xi}\,\mathbf{x}_A\right) \tag{2.24}$$

and

$$\mathbf{m}^{(2)}(\boldsymbol{\xi}) = \frac{1}{2}\left(\sum_{A\in N^+}\frac{\partial\Phi_A(\xi,\eta)}{\partial\eta}\,\mathbf{x}_A + \sum_{A\in N^-}\frac{\partial\Phi_A(\xi,\eta)}{\partial\eta}\,\mathbf{x}_A\right) \tag{2.25}$$

Using these results, we can construct the unit normal to the surface as

$$\hat{\mathbf{n}} = \frac{\mathbf{n}}{|\mathbf{n}|} = \frac{\mathbf{m}^{(1)}\times\mathbf{m}^{(2)}}{\left|\mathbf{m}^{(1)}\times\mathbf{m}^{(2)}\right|}, \tag{2.26}$$

and the remaining, mutually orthogonal, directions are chosen as

$$\hat{\mathbf{t}}^{(1)} = \frac{\mathbf{m}^{(1)}}{\left|\mathbf{m}^{(1)}\right|} \tag{2.27}$$

$$\hat{\mathbf{t}}^{(2)} = \hat{\mathbf{n}}\times\hat{\mathbf{t}}^{(1)}. \tag{2.28}$$

In order to derive an expression for $\frac{\partial\mathbf{Q}^{3\mathrm{D}}}{\partial\mathbf{u}_A}$ from (2.22), we need the derivatives of each of the directions (2.26)–(2.28) with respect to $\mathbf{u}_A$. The derivatives of the coordinate directions are given by

$$\frac{\partial\hat{t}_i^{(1)}}{\partial u_{kA}} = \frac{1}{\left|\mathbf{m}^{(1)}\right|}\left(\frac{\partial m_i^{(1)}}{\partial u_{kA}} - \hat{t}_i^{(1)}\,\frac{\partial m_r^{(1)}}{\partial u_{kA}}\,\hat{t}_r^{(1)}\right), \tag{2.29}$$

$$\frac{\partial\hat{t}_i^{(2)}}{\partial u_{kA}} = \epsilon_{irs}\left(\frac{\partial\hat{n}_r}{\partial u_{kA}}\hat{t}_s^{(1)} + \hat{n}_r\frac{\partial\hat{t}_s^{(1)}}{\partial u_{kA}}\right), \text{ and} \tag{2.30}$$

$$\frac{\partial\hat{n}_i}{\partial u_{kA}} = \frac{1}{|\mathbf{n}|}\left(\frac{\partial n_i}{\partial u_{kA}} - \hat{n}_i\,\frac{\partial n_r}{\partial u_{kA}}\,\hat{n}_r\right), \tag{2.31}$$

where $\epsilon_{ijk}$ is the permutation symbol defined by

$$\epsilon_{ijk} = \begin{cases} 1 & \text{for even permutations of } i,\ j, \text{ and } k,\\ -1 & \text{for odd permutations of } i,\ j, \text{ and } k,\\ 0 & \text{otherwise}\end{cases} \tag{2.32}$$

and the derivatives of the tangent vectors (2.23) are

$$\frac{\partial\mathbf{m}^{(1)}}{\partial\mathbf{u}_A} = \frac{1}{2}\,\frac{\partial\Phi_A}{\partial\xi}\,\mathbf{1} \qquad \text{and} \qquad \frac{\partial\mathbf{m}^{(2)}}{\partial\mathbf{u}_A} = \frac{1}{2}\,\frac{\partial\Phi_A}{\partial\eta}\,\mathbf{1}. \tag{2.33}$$

The expression for $\frac{\partial\mathbf{n}}{\partial\mathbf{u}_A}$ in (2.31) follows from the definition of $\mathbf{n}$ in (2.26) as

$$\frac{\partial n_i}{\partial u_{kA}} = \epsilon_{irs}\left(\frac{\partial m_r^{(1)}}{\partial u_{kA}}m_s^{(2)} + m_r^{(1)}\frac{\partial m_s^{(2)}}{\partial u_{kA}}\right). \tag{2.34}$$

With these results, the formulation of the element level nodal force vector and consistent tangent matrix is complete. These expressions are valid for cohesive surfaces within a standard finite

element framework as well as within the framework of meshfree methods. In using these expressions with meshfree methods, some modification of the nodes defining the displacement jump (2.4) is needed. Furthermore, the current configuration of the element mid-plane from (2.15) and (2.16) must be modified to account for the meshfree nature of the displacement field. Within a standard finite element setting, the nodes defining the geometry are the same nodes defining the opening displacement. In this sense, the elements may be considered "isoparametric". As is shown in Section 3.3 describing the formulation of cohesive elements in a meshfree domain, any points in the undeformed configuration can be used to define the reference element geometry while the opening displacement is calculated from the meshfree representation of the displacement field.

### 2.1.2 Cohesive surface relations

The element formulation presented in Section 2.1.1 makes use of a local coordinate frame defined with respect the deforming facets of the cohesive surface. This construction allows all surface constitutive relations to define the evolution of the local traction $\tilde{\mathbf{T}}$ with respect to the local opening displacement $\tilde{\boldsymbol{\Delta}}$, while the kinematics of large deformation and surface rotations are accounted for at the element level. For the case of an elastic, or reversible, cohesive relation, the traction is derived from a free energy potential $\varphi$ as

$$\tilde{\mathbf{T}} = \frac{\partial \varphi}{\partial \tilde{\boldsymbol{\Delta}}} \tag{2.35}$$

while the surface stiffness may be expressed as

$$\frac{\partial \tilde{\mathbf{T}}}{\partial \tilde{\boldsymbol{\Delta}}} = \frac{\partial^2 \varphi}{\partial \tilde{\boldsymbol{\Delta}} \partial \tilde{\boldsymbol{\Delta}}}. \tag{2.36}$$

The use of $\varphi$ in here differs from its definition in Section A.1. Throughout this section we will use $\varphi$ to denote a cohesive potential. Using (2.36), we see that the first term contributing to the element stiffness (2.11) is symmetric, while the remaining terms are generally nonsymmetric.

Motivated by the universal binding energy curves of Rose *et al.* [80] from atomistic modeling, Xu and Needleman[95] proposed the mixed-mode cohesive potential

$$\varphi\Big(\tilde{\boldsymbol{\Delta}}\Big) = \phi_n + \phi_n \exp\left(-\frac{\tilde{\Delta}_n}{\delta_n}\right)\left(\left[1 - r + \frac{\tilde{\Delta}_n}{\delta_n}\right]\frac{1-q}{r-1} - \exp\left(-\frac{\tilde{\Delta}_t^2}{\delta_t^2}\right)\left[q + \left(\frac{r-q}{r-1}\right)\frac{\tilde{\Delta}_n}{\delta_n}\right]\right). \tag{2.37}$$

From (2.35), the components of the traction are

$$\tilde{T}_n\Big(\tilde{\boldsymbol{\Delta}}\Big) = \frac{\phi_n}{\delta_n}\exp\left(-\frac{\tilde{\Delta}_n}{\delta_n}\right)\left(\frac{\tilde{\Delta}_n}{\delta_n}\exp\left(-\frac{\tilde{\Delta}_t^2}{\delta_t^2}\right) + \frac{1-q}{r-1}\left[1 - \exp\left(-\frac{\tilde{\Delta}_t^2}{\delta_t^2}\right)\right]\left[r - \frac{\tilde{\Delta}_n}{\delta_n}\right]\right) \tag{2.38}$$

and

$$\tilde{T}_t\Big(\tilde{\boldsymbol{\Delta}}\Big) = 2\,\phi_n \frac{\tilde{\Delta}_t}{\delta_t^2}\left(q + \left[\frac{r-q}{r-1}\right]\frac{\tilde{\Delta}_n}{\delta_n}\right)\exp\left(-\frac{\tilde{\Delta}_n}{\delta_n}\right)\exp\left(-\frac{\tilde{\Delta}_t^2}{\delta_t^2}\right). \tag{2.39}$$

In (2.37)–(2.39), the ratio $q = \frac{\phi_t}{\phi_n}$ relates the pure normal mode to shear mode fracture energy and $r = \frac{\tilde{\Delta}_n^*}{\delta_n}$ defines $\tilde{\Delta}_n^*$, the value of $\tilde{\Delta}_n$ after complete shear separation with $\tilde{T}_n = 0$. The effect

of $r$ vanishes when $q = 1$, which is the value used for all calculations in this study. The normal and tangential openings are defined as $\tilde{\Delta}_n = \tilde{\boldsymbol{\Delta}} \cdot \tilde{\mathbf{n}}$ and $\tilde{\Delta}_n = \tilde{\boldsymbol{\Delta}} \cdot \tilde{\mathbf{t}}$ with respect to the local normal and tangent. Xu and Needleman developed this cohesive relation in two dimensions. We extend this relation to three dimensions by assuming the response to be isotropic with respect to the tangential opening. That is, the response is expressed only in terms of the magnitude of the tangential opening, which can also be written as

$$\tilde{\Delta}_t = \left| \tilde{\boldsymbol{\Delta}} - \tilde{\Delta}_n \, \tilde{\mathbf{n}} \right|, \tag{2.40}$$

to emphasize that it is independent of $\tilde{\mathbf{t}}$. For the three-dimensional model, we did not attempt to incorporate any additional effects from the relative rotation of the surfaces about the normal.

The potential developed by Xu and Needleman is of the form $\varphi(\boldsymbol{\Delta})$, where the vector argument implies the potential itself explicitly dictates the dependence of the traction on the shear and opening components of displacement. By inspection of (2.37), it is clear that potentials of this type are difficult to derive for specific behavior. In contrast, others[15, 16, 70, 81] have proposed cohesive potentials which can be expressed in terms of a scalar, effective opening displacement $\hat{\varphi}(\Delta)$. The dependence on the shear and normal components of the opening displacement is incorporated into the definition of the effective opening displacement

$$\Delta^{\text{eff}} = \sqrt{\tilde{\boldsymbol{\Delta}} \cdot \boldsymbol{\beta} \tilde{\boldsymbol{\Delta}}}, \tag{2.41}$$

where $\boldsymbol{\beta}$ is introduced to produce mixed-mode effects. $\boldsymbol{\beta}$ is typically diagonal and controls the relative effect of the shear and normal openings. From (2.41) and (2.35), the cohesive traction is

$$\tilde{\mathbf{T}} = \frac{\partial \varphi}{\partial \tilde{\boldsymbol{\Delta}}} = \frac{1}{\Delta^{\text{eff}}} \frac{\partial \hat{\varphi}}{\partial \Delta} \boldsymbol{\beta} \tilde{\boldsymbol{\Delta}}, \tag{2.42}$$

for symmetric $\boldsymbol{\beta}$. From (2.42) and (2.41), we can define an effective traction

$$T^{\text{eff}} = \frac{\partial \hat{\varphi}}{\partial \Delta} = \sqrt{\tilde{\mathbf{T}} \cdot \boldsymbol{\beta}^{-1} \, \tilde{\mathbf{T}}}. \tag{2.43}$$

Note that the effective traction $T^{\text{eff}}$ is not equal to the magnitude of the traction $|\tilde{\mathbf{T}}|$ unless $\boldsymbol{\beta} = \mathbf{1}$.

One advantage of scalar traction potentials is that they allow greater flexibility in the form of the potential. Any one-dimensional relation may used used to define mixed-mode response by making use of the effective opening concept. Moreover, damage-like variables are readily incorporated to model irreversibility in the failure process. Since the direction of opening is lost in calculating $\Delta^{\text{eff}}$ from (2.41), the cohesive relations must be augmented with additional terms for compressive loading; otherwise, "tensile" failure will also occur in compression.

In Section 2.1.3, we describe the pathological mesh dependence that arises from an active cohesive surface network. Analysis of the softening the network produces shows the problem diminishes as the initial slope of cohesive relation increases. We would expect this because the mesh dependence results from the fictitious compliance introduced by the network. From a numerical standpoint, it is undesirable to address this issue by selecting a potential with an extremely stiff initial response because of the instabilities this produces in the solution procedure. An alternate approach to achieving cohesive elements that are initially rigid is to introduce them adaptively. Adaptive insertion of cohesive surfaces is not only an implementation decision, it also produces

certain constraints on the form of the cohesive law. Adaptive insertion of cohesive surfaces has been used by Ortiz *et al.* in simulations of dynamic fracture and fragmentation in two[15, 16] and three[71, 81] dimensions using a scalar traction potential and the effective opening concept. Adaptive insertion requires selecting a criterion to trigger the start of the failure process. Ortiz *et al.* use the effective traction in the failure initiation criterion

$$T^{\text{eff}} \geq \sigma_c. \tag{2.44}$$

We can gain some insight into this criterion and the role of the effective opening displacement by assuming a simple form for $\boldsymbol{\beta}$ to yield

$$\begin{aligned} T^{\text{eff}} &= \sqrt{\tilde{\mathbf{T}} \cdot [\beta^{-2}\,\mathbf{1} + (1-\beta^{-2})\,\tilde{\mathbf{n}} \otimes \tilde{\mathbf{n}}]\,\tilde{\mathbf{T}}} \\ &= \sqrt{\beta^{-2}\,\tilde{T}_t^2 + \tilde{T}_n^2}. \end{aligned} \tag{2.45}$$

From (2.45), it is evident the parameter $\beta$ controls the sensitivity of the failure criterion to shear and normal tractions. From micromechanical considerations, one can imagine that frictional materials exhibit especially high capacities for shear loading. Indeed, for simulations of concrete, Ortiz *et al.* [81] select $\beta = 10$. The coefficients in $\boldsymbol{\beta}$ are fitted to experiments of high strain rate axial compression[20, 21]. However, under mixed-mode conditions its difficult to determine the mechanisms leading to the variation in the fracture energy. The variation could be the result of crack face contact and friction or changes in the behavior of the local bulk dissipation. The coupling of these additional sources of dissipation to the cohesive behavior has not been studied in detail. Other failure initiation criteria have may be proposed, such as those based on the maximum circumferential crack tip stress[25], or similarly, crack extension perpendicular to the direction of the maximum principal stress. This latter criterion is based on observations that cracks appear to propagate in the "local mode I" direction[7, 85]. The difficulty with the initiation criteria lies not only in selecting a suitable value of the "strength" of material, but also in incorporating the effect of mixed-mode loading on the predicted failure condition and the corresponding crack extension direction.

An additional requirement in formulating a mixed-mode cohesive relations for application to adaptive insertion approaches is that they must allow the initial traction to be specified explicitly in order to ensure that the traction along the initiated failure surface is continuous in time and evolves in a physically meaningful way. In formulating this class of cohesive surface relations, we might assume the tractions are given by

$$\tilde{\mathbf{T}}\left(\tilde{\boldsymbol{\Delta}}\right) = \mathbf{D}\left(\tilde{\boldsymbol{\Delta}}\right)\,\tilde{\mathbf{T}}_0, \tag{2.46}$$

where $\tilde{\mathbf{T}}_0$ is the traction at failure initiation and $\mathbf{D}\left(\tilde{\boldsymbol{\Delta}}\right)$ represents a general mixed-mode evolution relation for the traction, restricted by the conditions that

$$\mathbf{D}(\mathbf{0}) = \mathbf{1} \qquad \text{and} \qquad \lim_{|\tilde{\boldsymbol{\Delta}}|\to\infty} \mathbf{D}\left(\tilde{\boldsymbol{\Delta}}\right) = \mathbf{0}. \tag{2.47}$$

When expressed in the form suggested by (2.46) and (2.47), the cohesive tractions do not evolve identically at all points on the failure surface. In general, the initial traction will differ depending

on the state of stress at initiation. This observation is different from the usual notion of first determining a cohesive surface relation based on experimental measurements or a model for the failure process and then applying this identical relation to every occurrence of the failure mode. As shown above, the evolution process is treated as an initial value problem where the initial conditions are determined by the state of stress, or traction, at the onset of failure. Viewed in this sense, $\mathbf{D}$ represents this process and is the same for each surface. More generally, we could express the mixed-mode evolution as $\mathbf{D}\left(\tilde{\boldsymbol{\Delta}}, \tilde{\mathbf{T}}_0, \mathbf{q}\right)$, where $\mathbf{q}$ represents any state variables. As a simple example, we might choose an evolution relation, taking a scalar argument, that incorporates the exponential "tail" of the universal binding energy curve[80]

$$\hat{\mathbf{D}}\left(\Delta^{\text{eff}}\right) = \exp\left(-\frac{\Delta^{\text{eff}}}{\delta_c}\right)\mathbf{1}, \tag{2.48}$$

where $\delta_c$ represent a characteristic opening to failure. One problem with an evolution relation of this form is that traction magnitude evolves, but the direction remains the same in the local frame. There have not been sufficient detailed experimental observations of the evolution failure process zones to determine the shortcomings of this assumption.

For the simulations presented in Section 4.4, we used the linear, damage-like, traction evolution relation

$$\hat{\mathbf{D}}\left(\Delta^{\text{eff}}\right) = \begin{cases} \left(1 - \frac{\Delta^{\text{eff}}}{\delta_c}\right)\mathbf{1} & \Delta^{\text{eff}} \geq \Delta^{\text{eff}}_{\text{max}}, \\ \Delta^{\text{eff}}\left(1 - \frac{\Delta^{\text{eff}}_{\text{max}}}{\delta_c}\right)\mathbf{1} & \Delta^{\text{eff}} < \Delta^{\text{eff}}_{\text{max}}, \\ \mathbf{0} & \Delta^{\text{eff}}_{\text{max}} > \delta_c, \end{cases} \tag{2.49}$$

where $\Delta^{\text{eff}}_{\text{max}}$ is a state variable tracking the maximum effective displacement achieved. The fracture energy defined by

$$G = \int \mathbf{T} \cdot d\boldsymbol{\Delta} \tag{2.50}$$

for general $\boldsymbol{\beta} \neq \mathbf{1}$ requires specification of the opening displacement history. For the simplified case of purely opening mode displacement with $\boldsymbol{\beta} = \mathbf{1}$, the linear traction evolution law from (2.49) displays a fracture energy of

$$G = \frac{1}{2}\left|\mathbf{T}_0\right| \delta_c. \tag{2.51}$$

### 2.1.3 Softening induced by a cohesive surface network

In an idealized description of the cohesive surface network approach, the complete material description is separated into fracture properties captured by the cohesive surface constitutive model while bulk properties may be selected with near complete independence. Furthermore, the discrete collection of fracture surfaces is assumed to yield realistic crack paths on average or as the mesh is refined. In the discussion that follows, we demonstrate that the method is not convergent as a function of mesh size. Furthermore, we develop a condition for the existence of a true continuum cohesive crack from the notion that the traction distribution in the failure process zone must be well-resolved over the spatial discretization near the tip.

An active cohesive surface network may be considered as a composite material consisting of discrete surface elements inserted between continuum regions exhibiting some bulk constitutive properties. Naturally, the effective elastic properties of the composite depend on properties of both

the surface and bulk constitutive relations although the surfaces are introduced only to produce fracture behavior. This distortion of elastic properties is present for all degrees of deformation and is exhibited by the composite even in the undeformed state. Moreover, the elastic properties of the composite are mesh-dependent both in terms of a general softening with decreasing mesh size and anisotropy induced by the mesh texture. In essence, the difficulties arise because the surface relations exhibit an inherent length scale that is absent in homogeneous deformations. Since this length scale is introduced at the level of the finite element discretization, it is not surprising that the resulting difficulties are also mesh-dependent.

A one-dimensional example can be used to demonstrate the general features of the distortion of elastic properties produced by an active cohesive surface network. For the one-dimensional case, the cohesive surfaces simply produce softening. In multiple dimensions, this distortion takes the form not only of a change in overall stiffness, but also the development of anisotropy which is dependent on the detailed layout of the mesh. A one-dimensional cohesive network is shown in left portion of Figure 2.2. The spacing between cohesive surfaces in the undeformed state is $h$. Subject

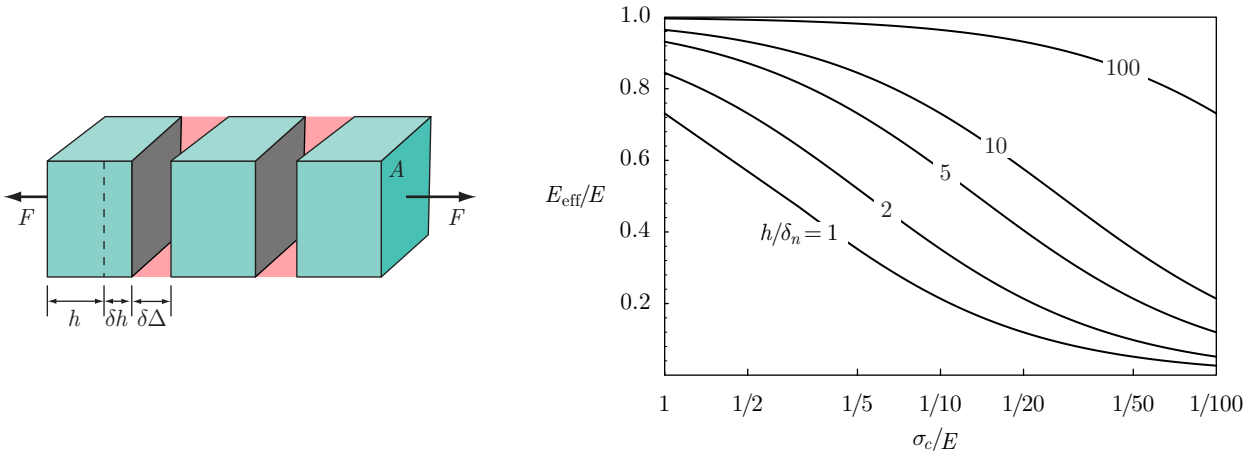


Figure 2.2: A one-dimensional cohesive surface network and its effective modulus $E_{\text{eff}}$ as a function of surface spacing $h$ and cohesive parameters $\delta_n$ and $\sigma_c$.

to some loading, each continuum block stretches by an amount $\delta h$, and each surface opens by a jump of $\delta\Delta$. Traction continuity requires

$$E\,\epsilon = k\,\delta\Delta, \tag{2.52}$$

where $E$ is Young's modulus of the bulk, $\epsilon$ is the infinitesimal strain $\frac{\delta h}{h}$, and $k$ is the constant of proportionality between the initial opening displacements and the resulting tractions. The effective modulus of the composite is $E_{\text{eff}} = \sigma/\epsilon_{\text{tot}}$, where the total strain is

$$\epsilon_{\text{tot}} = \frac{\delta h + \delta\Delta}{h}. \tag{2.53}$$

Combining these expressions, the effective modulus of the composite may be written as

$$E_{\text{eff}} = E\left[1 - \frac{1}{1 + \frac{k\,h}{E}}\right]. \tag{2.54}$$

From this result, we see that the properties of the continuum are recovered as the cohesive surfaces become rigid, that is, $E_{\text{eff}} \to E$ as $k \to \infty$ or $h \to \infty$. In practice, the bulk constitutive properties, represented by $E$, and the fracture properties, represented by $k$, are selected to represent a particular material. Therefore, $E_{\text{eff}}$ in (2.54) has only one free parameter $h$, the surface cohesive surface spacing which is also the continuum element size since cohesive surfaces are inserted between all element interfaces. As we make the continuum elements smaller, the effective stiffness of the composite medium decreases.

In order to demonstrate the significance of this softening, we make use of the cohesive relations developed by Xu and Needleman[95]. Since this analysis describes only the properties of the undeformed network, the detailed form of the relation does not contribute to the effective modulus expression (2.54), but a particular relation is needed to express the softening behavior in terms of cohesive parameters. In the absence of shear deformations, the normal component of traction is given by

$$T_n(\Delta_n) = \frac{\phi_n}{\delta_n^2}\,\Delta_n \exp\left(-\frac{\Delta_n}{\delta_n}\right), \tag{2.55}$$

where $\phi_n$ is the mode I work to fracture and $\delta_n$ is the normal opening at which the maximum traction of

$$\sigma_c = \frac{\phi_n}{e\,\delta_n} \tag{2.56}$$

is produced, where $e = \exp(1)$. For initial openings, the proportionality constant $k$ in (2.52) is

$$k = \frac{\phi_n}{\delta_n^2}. \tag{2.57}$$

In fitting the parameters of a cohesive model, we typically select the fracture energy $\phi_n$ and a value for either $\sigma_c$ or $\delta_n$, neither of which has been experimentally determined with a high degree of certainty. Orowan estimated $E/\sigma_c = 30$, though values of 10[95] to 600[15] have been used in the literature.

The right portion of Figure 2.2 shows the effective modulus of the one-dimensional cohesive surface network as a function of the cohesive strength for a range of the surface spacings. The modulus of the continuum is recovered as $\sigma_c$ and $h/\delta_n$ increase.

### 2.1.4 A cohesive zone condition

In modeling phenomenon exhibiting intrinsic length scales, one expects these scales to result in some upper bound restrictions on the mesh dimension. A criterion for this upper bound is now developed based on a cohesive zone condition. In order for simulations using cohesive surfaces to return reliable results, the tractions in the cohesive zone must be well-resolved by the spatial discretization. Otherwise, the fracture energy fails to be represented accurately. We define the "cohesive zone" as the region on a fracture plane from the location of peak tractions to the "tail" of the distribution where we consider the material to be completely failed. The size of this zone depends not only on the properties of the cohesive relation, but also on the bulk constitutive properties and the local geometry. In order to derive a condition for the existence of a continuum cohesive crack, we make use of the linear elastic, asymptotic tip fields. The stress varies as

$$\sigma = \frac{K}{\sqrt{2\pi r}}, \tag{2.58}$$

where $K$ is the stress intensity fracture and $r$ is the distance from the tip. The distance from the crack tip at which the cohesive stress is attained is

$$r_c = \frac{1}{2\pi}\frac{\phi\, E_{\text{eff}}}{\sigma_c^2}, \tag{2.59}$$

where we have introduced the fracture energy $\phi$ and the bulk constitutive properties using Irwin's relation $\phi = K^2/E_{\text{eff}}$. As with estimates of plastic zone sizes made with this approach, $r_c$ likely underestimates the true distance to the tip at which the cohesive strength is attained since removal of the stress singularity produces a redistribution of stresses near the tip. We now define a cohesive zone condition

$$r_c > h, \tag{2.60}$$

which states that in order for our simulations to capture the continuum notion of a cohesive crack, the mesh dimension $h$ must be smaller than the characteristic dimensions over which the cohesive tractions act. Making use of the effective modulus for the one-dimensional cohesive surface network (2.54) together with the parameters of the Xu-Needleman potential, we find the cohesive zone condition requires

$$\frac{h}{\delta_n} < \left(\frac{e}{2\pi} - \frac{1}{e}\right)\frac{E}{\sigma_c} \approx \frac{1}{15}\,\frac{E}{\sigma_c}. \tag{2.61}$$

In the calculations of Xu and Needleman[95], they choose the cohesive strength as $E/\sigma_c = 10$, meaning the cohesive zone condition can only be satisfied if the characteristic mesh dimension is smaller than the critical opening displacement. The ratio of mesh size to critical opening displacement in Xu and Needleman's study varies over the range $5 < h/\delta_n < 50$, meaning that the cohesive zone condition is not satisfied. For $h/\delta_n = 5$, the effective modulus (2.54) is only 60% of its desired value. Reducing $h$ further to satisfy the cohesive zone condition would result in even greater distortion of the elastic properties. This approximate analysis indicates that no ideal compromise exists between the mesh size restrictions required to preserve the elastic response and those required to resolve the near tip cohesive zone. The consequences of failing to satisfy the cohesive zone condition (2.60) are not well understood. In Section 4.3, we study these issues further with numerical examples.

## 2.2 Virtual Internal Bond model

In contrast the the surface model present in Section 2.1, we next present a bulk constitutive model that displays cohesive behavior. The general features of the VIB model, as well as more detailed study of its localization behavior under conditions of dynamic crack propagation, are described in greater detail elsewhere[34, 45, 46, 47]. A brief review of the model is repeated here to provide a description of cohesive behavior in the bulk behavior and to provide relations needed to fit the parameters of the model to specific material behavior. The model attempts to incorporate the behavior of a spatial distribution of cohesive bonds that are presumed to act at the microstructural level. The link between the microstructure and continuum-level measures of deformation is made using the Cauchy-Born rule, which assume macroscopic measures of deformation are imposed uniformly across the underlying microstructure analogous to Taylor's assumption for polycrystalline plasticity formulations. This approach is employed by Ortiz, Phillips, and Tadmor to develop constitutive models for single crystal materials[87]. From a practical point of view, it is desirable to

extend the procedure for embedding cohesive behavior beyond models for single crystal materials. We would like to develop a model to study fracture in noncrystalline materials, such as polymers or glasses, or in polycrystalline materials for which the elastic anisotropy is lost due to the homogenizing effect of many randomly oriented crystalline grains. The concept of homogenization is applied here to the interactions between material particles. The resulting constitutive model embeds the cohesive nature of the interaction potentials, but is free of any orientational dependencies.

The VIB model is developed within the framework of hyperelasticity. The current, or deformed, configuration of a body is described as $\mathbf{x} = \boldsymbol{\varphi}(\mathbf{X})$, by a mapping $\boldsymbol{\varphi}$ of the undeformed configuration $\mathbf{X}$. The arrangement of cohesive interactions among material particles is described by a spatial bond density function. The strain energy density is computed by integrating the bond density in space in a continuous analog to the sum over discrete lattice neighbors for the case of crystalline materials. The VIB form of the strain energy density function is

$$\Phi = \frac{1}{\Omega_0} \int_{\Omega_0^*} U(l)\, D_\Omega \, d\Omega, \tag{2.62}$$

where $\Omega_0$ is the undeformed representative volume, $l$ is the deformed virtual bond length, $U(l)$ is the bonding potential, $D_\Omega$ is the volumetric bond density function, and $\Omega_0^*$ is the integration volume defined by the range of influence of $U$. Depending on the range of influence of the bond potential function, the integration volume $\Omega_0^*$ may not correspond with the representative volume $\Omega_0$. This difference may be illustrated for crystalline materials whenever the bond potentials extend beyond the lattice unit cell. This method was first alluded to by Gao[31] as a method for constructing an amorphous network of cohesive bonds by a spatial average. The deformed bond length $l$ is computed from the Cauchy-Born rule, assuming the integration volume $\Omega_0^*$ deforms homogeneously as described by a given deformation gradient $\mathbf{F} = \frac{\partial \boldsymbol{\varphi}}{\partial \mathbf{X}}$. In order to avoid questions as to whether the Cauchy-Born rule holds for the proposed microstructure, we consider only bond density functions $D_\Omega$ that are centrosymmetric. Under this restriction, the deformation at the microstructural level must be homogeneous in order to maintain the symmetry present in the undeformed configuration. In extending this description from a lattice of discrete bonding interactions to a continuous bond distribution, the invariance in the deformation with respect to translation of our observation point is not limited to positioning the coordinate origin at crystal lattice sites. All points in the material act as centers of symmetry. From physical considerations, we assume the bonding function $U$ will be relatively short range so that, although the bond density function $D_\Omega$ describes the relative particle distribution of the entire body about the observation point, the integration volume $\Omega_0^*$ will be on the order of the representative volume $\Omega_0$. The undeformed virtual bond vector is represented as

$$\mathbf{L} = L\, \boldsymbol{\Xi}, \tag{2.63}$$

where $L$ is the reference bond length, and $\boldsymbol{\Xi}$ is a unit vector in the direction of the undeformed bond. Undeformed bonds are mapped to their deformed configuration $\boldsymbol{l}$ by

$$\boldsymbol{l} = \mathbf{F}\, \mathbf{L}. \tag{2.64}$$

Making use of the right Cauchy-Green stretch tensor, the deformed bond length is

$$l(\mathbf{C}) = L \sqrt{\boldsymbol{\Xi} \cdot \mathbf{C}\, \boldsymbol{\Xi}}. \tag{2.65}$$

Expressed as a function of $\mathbf{C}$, the deformed bond length transforms objectively by construction. The stress response and tangent moduli are computed from the strain energy density (2.62) using the relations from Green elastic theory[63]. Employing

$$\frac{\partial l}{\partial \mathbf{C}} = \frac{L^2}{2\,l}\,\boldsymbol{\Xi}\otimes\boldsymbol{\Xi}, \tag{2.66}$$

the (symmetric) 2nd Piola-Kirchhoff stress is

$$\mathbf{S} = 2\,\frac{\partial \Phi}{\partial \mathbf{C}} = \frac{1}{\Omega_0}\int\limits_{\Omega_0^*} \frac{U'(l)}{l}\,\boldsymbol{\Xi}\otimes\boldsymbol{\Xi}\,L^2\,D_\Omega\,d\Omega, \tag{2.67}$$

and the material tangent modulus is

$$\mathbf{C} = 2\,\frac{\partial \mathbf{S}}{\partial \mathbf{C}} = \frac{1}{\Omega_0}\int\limits_{\Omega_0^*} \left(\frac{U''(l)}{l^2} - \frac{U'(l)}{l^3}\right)\boldsymbol{\Xi}\otimes\boldsymbol{\Xi}\otimes\boldsymbol{\Xi}\otimes\boldsymbol{\Xi}\,L^4\,D_\Omega\,d\Omega. \tag{2.68}$$

The modulus (2.68) displays Cauchy symmetry as well as the usual major and minor symmetries of elasticity. This result that an amorphous solid with a random network of cohesive bonds satisfies the Cauchy relation seems to be a generalization of Stakgold's theorem[86] to an amorphous solid. A material particle in an amorphous solid satisfies centrosymmetry in a statistical sense, and the cohesive force law corresponds to a two-body potential.

Since we limit our study to centrosymmetric bond density functions, it is natural to express the strain energy density (2.62) in spherical coordinates as

$$\Phi(\mathbf{C}) = \langle U(l)\rangle = \left\langle U(L\sqrt{\boldsymbol{\Xi}\cdot\mathbf{C}\,\boldsymbol{\Xi}})\right\rangle, \tag{2.69}$$

where each bond is characterized by coordinates $\{L,\theta,\phi\}$. For conciseness, we have introduced the notation of a spherical average as

$$\langle\bullet\rangle = \frac{1}{\Omega_0}\int\limits_{-\pi}^{\pi}\int\limits_{0}^{\pi}\int\limits_{0}^{L^*} (\bullet)\,D(L,\theta,\phi)\,L^2\sin\theta\,dL\,d\theta\,d\phi, \tag{2.70}$$

where $L^*$ represents the maximum distance over which particles interact. In spherical coordinates, the bond direction vector $\boldsymbol{\Xi}$ can be written as

$$\boldsymbol{\Xi}(\theta,\phi) = \begin{Bmatrix}\sin\theta\,\cos\phi\\ \sin\theta\,\sin\phi\\ \cos\theta\end{Bmatrix}. \tag{2.71}$$

The precise definition of $D(L,\theta,\phi)$ is that $D(L,\theta,\phi)\,L^2\sin\theta\,dL\,d\theta\,d\phi$ represents the number of bonds in the undeformed solid with length between $L$ and $L+dL$ and orientation between $\{\theta,\phi\}$ and $\{\theta+d\theta,\phi+d\phi\}$. Using this notation, the components of the 2nd Piola-Kirchhoff stress and the material tangent modulus from (2.67) and (2.68) can be represented as

$$\mathbf{S} = \left\langle \frac{L^2U'(l)}{l}\,\boldsymbol{\Xi}\otimes\boldsymbol{\Xi}\right\rangle \tag{2.72}$$

and

$$\mathbf{C} = \left\langle L^4 \left( \frac{U''(l)}{l^2} - \frac{U'(l)}{l^3} \right) \boldsymbol{\Xi} \otimes \boldsymbol{\Xi} \otimes \boldsymbol{\Xi} \otimes \boldsymbol{\Xi} \right\rangle . \tag{2.73}$$

The properties of the VIB model are determined by the choice of the bond density distribution function $D(L, \theta, \phi)$. In this study, we consider only the isotropic form of the model. The distribution function

$$D(L, \theta, \phi) = D_L(L) \tag{2.74}$$

yields an isotropic solid with fully randomized internal bonds. The instantaneous response becomes generally anisotropic under finite deformations. The associated average for the isotropic case is

$$\langle \bullet \rangle_L = \frac{1}{\Omega_0} \int_0^{L^*} (\bullet) D_L(L)\, L^2\, dL. \tag{2.75}$$

Selecting the radial bond distribution function as

$$D_L(L) = D_0\, \delta_D(L - L_0)\,, \tag{2.76}$$

where $D_0$ is a constant, implies that all of the bonds in the solid are of the same type, or initial length. The result is a model for amorphous material with nearest neighbor bonding only. With this bond distribution, the strain energy density from (2.69) and (2.70) becomes

$$\Phi = \frac{D_0\, L_0^2}{\Omega_0} \int_{-\pi}^{\pi} \int_0^{\pi} U(l) \sin\theta\, d\theta\, d\phi. \tag{2.77}$$

The distribution function

$$D(L, \theta, \phi) = D_L(L)\, \delta_D(\theta - \pi/2) \tag{2.78}$$

yields a plane stress, isotropic solid. Unlike the standard plane stress approximation, this model is truly two-dimensional, displaying no out-of-plane deformation or stress. The material can be thought of as being composed of a single sheet of cohesive bonds, or layers of noninteracting sheets, since all of the bonds lie in a single plane. As was the case in three dimensions, selecting $D_L(L)$ as (2.76) yields a model for amorphous material with nearest neighbor bonding only. For this case, the strain energy density has the especially simple form

$$\Phi = \frac{D_0\, L_0^2}{\Omega_0} \int_{-\pi}^{\pi} U(l)\, d\phi. \tag{2.79}$$

Though this model may be physically unrealistic, its simplicity makes it useful for both theoretical and numerical investigations of the fracture properties resulting from the VIB approach.

In the sections that follow, we will investigate the stress response and fracture properties exhibited by the VIB model. The goal of these sections is to present relations between the bond potential parameters and resulting model response. These relations allow the model to be fitted to particular materials.

### 2.2.1 Isotropically elastic properties at infinitesimal strain

We are particularly interested in the properties of an amorphous network of cohesive bonds that is homogeneous and isotropic at small strain. The properties of the model at small strains can be used to fit the model parameters to particular materials. For this case, the bond density function is selected as $D(L,\theta,\phi) = D_L(L)$, and $\mathbf{E}$, the Green Lagrangian strain, and $\mathbf{S}$ reduce to the strain and stress tensors of linear elasticity: $\mathbf{E} \to \boldsymbol{\epsilon}$ and $\mathbf{S} \to \boldsymbol{\sigma}$. $\Phi$ can be expanded up to the quadratic term as

$$\Phi(\boldsymbol{\epsilon}) = \left\langle U(L) + \frac{L^2}{2} U''(L)\,(\boldsymbol{\Xi}\cdot\boldsymbol{\epsilon}\,\boldsymbol{\Xi})\,(\boldsymbol{\Xi}\cdot\boldsymbol{\epsilon}\,\boldsymbol{\Xi}) \right\rangle, \tag{2.80}$$

where the first order term does not appear since the interaction potential is assumed to satisfy $\langle U'(L)\rangle = 0$ to give a stress-free, undeformed state. This produces the generalized Hooke's law

$$\sigma_{ij} = \mathsf{c}_{ijkl}\,\epsilon_{kl}, \tag{2.81}$$

where the modulus under infinitesimal deformations is related to the cohesive bond distribution by

$$\begin{aligned} \mathbf{c} &= \left\langle L^2\, U''(L)\, \boldsymbol{\Xi}\otimes\boldsymbol{\Xi}\otimes\boldsymbol{\Xi}\otimes\boldsymbol{\Xi} \right\rangle \\ &= \left\langle L^2 U''(L) \right\rangle_L \int_{\pi}^{-\pi}\int_{0}^{\pi} \boldsymbol{\Xi}\otimes\boldsymbol{\Xi}\otimes\boldsymbol{\Xi}\otimes\boldsymbol{\Xi}\,\sin\theta\,d\theta\,d\phi. \end{aligned} \tag{2.82}$$

It can be directly verified that

$$\int_{\pi}^{-\pi}\int_{0}^{\pi} \Xi_i\,\Xi_j\,\Xi_k\,\Xi_l \sin\theta\,d\theta\,d\phi = \frac{4\pi}{15}\left(\delta_{ij}\delta_{kl} + \delta_{ik}\delta_{jl} + \delta_{il}\delta_{kj}\right) \tag{2.83}$$

is a fourth-rank isotropic tensor. The resulting elastic stiffness tensor is

$$\mathsf{c}_{ijkl} = \mu\left(\delta_{ij}\delta_{kl} + \delta_{ik}\delta_{jl} + \delta_{il}\delta_{kj}\right), \tag{2.84}$$

with shear modulus equal to

$$\mu = \frac{4\pi}{15}\left\langle L^2\, U''(L)\right\rangle_L. \tag{2.85}$$

The other elastic constants are

$$\lambda = \mu \qquad \nu = 1/4 \qquad E = \frac{2\pi}{3}\left\langle L^2\, U''(L)\right\rangle_L, \tag{2.86}$$

where $\lambda$ and $\mu$ are the Lamé constants, $\nu$ is Poisson's ratio, and $E$ is Young's modulus. Since a variety of engineering materials display values of Poisson's ratio within a range around 1/4, the Cauchy symmetry exhibited by the VIB model does not represent a significant restriction of the formulation for application to practical analyses.

The results for the plane stress, isotropic bond density function

$$D(L,\theta,\phi) = D_L\,\delta_D(\theta - \pi/2) \tag{2.78}$$

are quite similar, but the relations for the elastic moduli (2.85,2.86) must be modified to account for the difference in spatial dimensions. The modulus in the generalized Hooke's law (2.81) is given by

$$\begin{aligned}\mathbf{c} &= \left\langle L^2\, U''(L)\, \boldsymbol{\Xi} \otimes \boldsymbol{\Xi} \otimes \boldsymbol{\Xi} \otimes \boldsymbol{\Xi} \right\rangle \\ &= \left\langle L^2 U''(L) \right\rangle_L \int_{\pi}^{-\pi} \boldsymbol{\Xi} \otimes \boldsymbol{\Xi} \otimes \boldsymbol{\Xi} \otimes \boldsymbol{\Xi}\, d\phi.\end{aligned} \tag{2.87}$$

The elastic stiffness tensor has the same form given in (2.84). However, the shear modulus becomes

$$\mu = \frac{\pi}{4} \left\langle L^2\, U''(L) \right\rangle_L . \tag{2.88}$$

From Cauchy symmetry, the Lamé constants are equal ($\lambda = \mu$), but the relations between the other elastic constants are different from the standard relations of three dimensional elasticity. From the Hooke's law relations in strictly two dimensions, Poisson's ratio, Young's modulus, and the bulk modulus are related to the Lamé constants by

$$\nu = \frac{\lambda}{\lambda + 2\mu}, \quad E = \frac{4\mu\,(\lambda + \mu)}{\lambda + 2\mu}, \quad \text{and} \quad \kappa = \lambda + \mu. \tag{2.89}$$

Using (2.89), the elastic constants for the plane stress isotropic VIB model are

$$\nu = 1/3, \qquad \text{and} \qquad E = \frac{2\pi}{3} \left\langle L^2\, U''(L) \right\rangle_L . \tag{2.90}$$

### 2.2.2 A model potential

The preceding discussions have not made reference to any particular cohesive potential. For the purpose of demonstration, we introduce the phenomenological cohesive force law

$$U'(l) = A\,(l - L) \exp\left( -\frac{l - L}{B} \right). \tag{2.91}$$

The defining characteristics of this potential are illustrated in Figure 2.3. The potential has a "well" of depth $U_0 = U(L) = -AB^2$. This quantity can be related to the fracture energy through a $J$-integral analysis[45]. The response of the potential for bond lengths around the location of this minimum is determined by the parameter $A$. The "stiffness" at the minimum is $U''(L) = A$. In the left portion of Figure 2.3, the potential $U$ is shown with a quadratic potential exhibiting the same energy, force, and stiffness at $l = L$. The quadratic potential defines the response of a "linear spring", for which the force always varies proportionally with the stretch in the bond. Compared with the quadratic potential, the cohesive potential displays greater stiffness for compressive deformations and the characteristic loss of convexity in tension.

The second parameter $B$ determines the cohesive properties of the potential. The maximum force $U'_{\max} = \frac{AB}{e}$, where $e = \exp(1)$, is generated for a stretched length of $l = L\left(1 + \frac{B}{L}\right)$. In terms of the 2nd Piola-Kirchhoff stress (2.67), we see that the cohesive strength displayed by the VIB model is not determined by the force $U'(l)$, but rather by the ratio $U'(l)\,/l$. The maximum value for this ratio occurs for

$$l_c = \frac{1}{2}\left( L + \sqrt{4\,B\,L + L^2} \right) = L + B + O\big(B^2/L\big)\,, \tag{2.92}$$

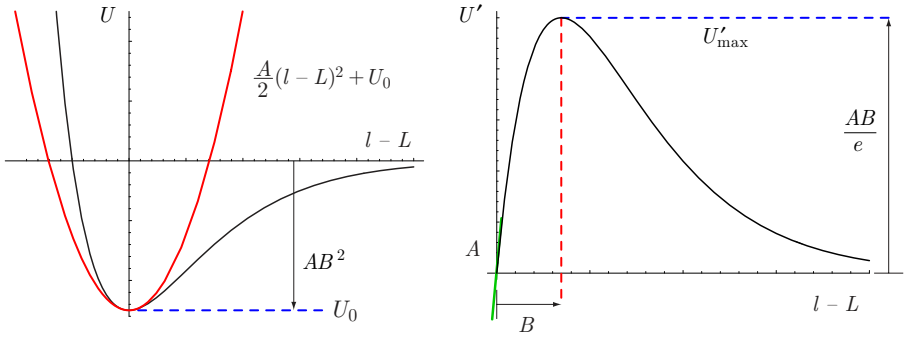


Figure 2.3: Characteristics of the phenomenological cohesive force potential from (2.91) illustrating effect of the parameters $A$ and $B$.

from which we find

$$\max_l \left[\frac{U'(l)}{l}\right] = \frac{U'(l_c)}{l_c} \approx \frac{AB}{e\,(L+B)}. \tag{2.93}$$

As we will show in the next section, the peak Cauchy stress under equitriaxial stretching depends on the maximum value of $U'(l)\,/l^2$. The maximum value for this ratio also occurs for

$$l_c^{3\mathrm{D}} = L + B + O\big(B^2/L\big)\,, \tag{2.94}$$

yielding

$$\max_l \left[\frac{U'(l)}{l^2}\right] = \frac{U'\big(l_c^{3\mathrm{D}}\big)}{\big(l_c^{3\mathrm{D}}\big)^2} \approx \frac{AB}{e\,L\,(L+2\,B)}. \tag{2.95}$$

### 2.2.3 Fitting of the cohesive strength

The cohesive strength exhibited by the model depends not only the choice of bond potential parameters, but also varies as a function of the deformation state. Experimentally, the cohesive strength of materials has never been determined. Estimates of the cohesive strength lie in the range of less that $E/600$, as used by Camacho and Ortiz[15], to $E/10$ used by Xu and Needleman[95], where $E$ is Young's modulus. Orowan[69] estimated the cohesive strength as $E/30$. The plane stress, isotropic VIB model provides a simplified means for studying the variation of the cohesive strength with deformation. With only two independent stretches determining the state of deformation, the results become considerably easier to understand than the fully three-dimensional case. For the two-dimensional case under equibiaxial stretching, the components of the 2$^{\text{nd}}$ Piola-Kirchhoff stress are

$$S_{IJ} = \left\langle \frac{L^2\,U'(l)}{l} \right\rangle_L \int_{-\pi}^{\pi} \Xi_I\,\Xi_J\,d\phi = \left\langle \frac{L^2\,U'(l)}{l} \right\rangle_L \pi\,\delta_{IJ}. \tag{2.96}$$

Selecting the radial bond density function as $D_L(L) = D_0\,\delta_D(L-L_0)$ from (2.76) where $D_0$ is a constant, the Cauchy stress can then be expressed as

$$\boldsymbol{\sigma} = \frac{\pi\,D_0\,L_0^4}{\Omega_0}\,\frac{U'(l)}{l}\,\mathbf{1}. \tag{2.97}$$

The cohesive strength is achieved at the maximum value of $U'(l)/l$, which is given by (2.93) for the model potential. Using this result, the cohesive strength under equibiaxial stretching for the plane stress, isotropic VIB model is given by

$$\sigma_c^* = \frac{D_0\, L_0^4}{\Omega_0}\, \frac{A\, B\, \pi}{e\,(L_0 + B)}. \tag{2.98}$$

This relation becomes a helpful normalizing factor which can be used to demonstrate how values of cohesive law parameters affect the cohesive strength displayed by the plane stress VIB model under different states of deformation.

The normalized cohesive strength $\sigma_c$ is shown over a range of deformation states for different values of $B/L$ in Figure 2.4. Primary extension of the material is in the $X_2$ direction. The stretch

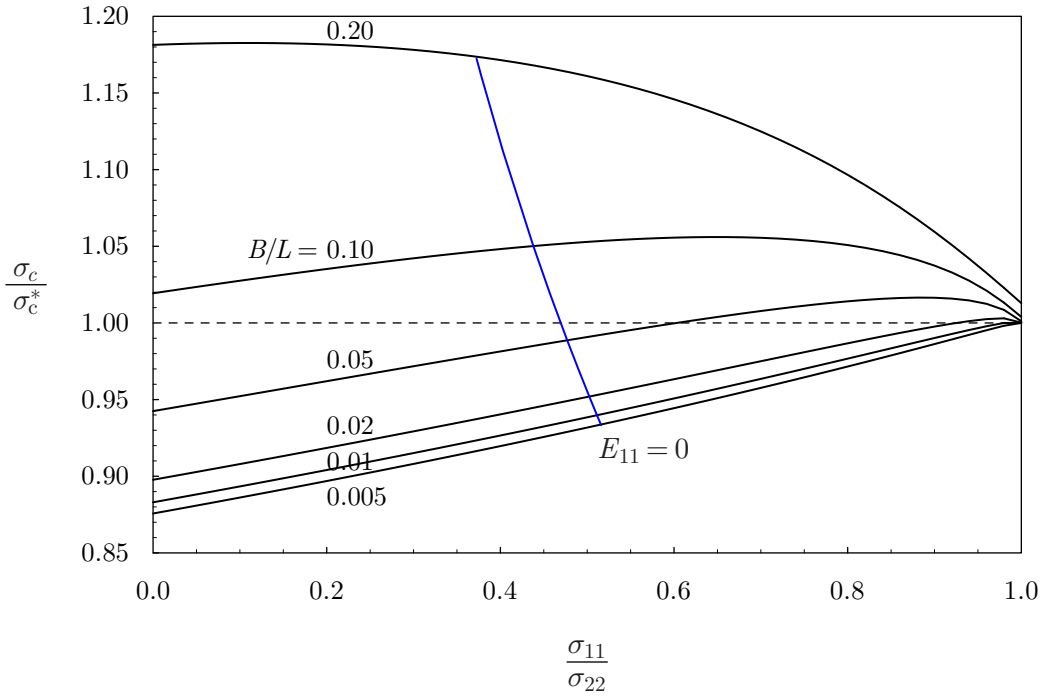


Figure 2.4: Variation in the cohesive stress $\sigma_c$ with the state of deformation for different values of the cohesive law parameter $B/L$ using the model interaction potential from Section 2.2.2.

in the $X_1$ direction is varied to control the stress ratio $\sigma_{11}/\sigma_{22}$ over a range from uniaxial stress ($\sigma_{11}/\sigma_{22} = 0$) to equibiaxial deformation ($\sigma_{11}/\sigma_{22} = 1$). States of uniaxial stretching are indicated by the line marked $E_{11} = 0$. Several aspects are apparent from the results shown in the figure. The relation (2.93) used to derive the cohesive strength under equibiaxial deformation is approximate, but holds to within 2% up to values of $B/L = 0.2$. For smaller values of $B/L$, the cohesive strength increases as the state of deformation is varied from uniaxial to equibiaxial stress. As the value of $B/L$ increases, the state of deformation which produces the highest cohesive strength shifts away from the equibiaxial state. A cohesive strength of $\sigma_c^* = E/30$ requires $B/L \approx 0.06$, which indicates that the maximum value of the cohesive stress occurs for a stress ratio $\sigma_{11}/\sigma_{22} \approx 0.7$ when the

model parameters are selected to produce realistic values of the cohesive strength. Finally, the cohesive strength for this case varies less than 5% from $\sigma_c^*$ over the full range of deformation states, indicating that (2.98) acts as a useful relation for fitting the VIB model to experimentally determined material properties.

For the isotropic model in three dimensions subject to equitriaxial stretching, the components of the 2nd Piola-Kirchhoff stress are

$$S_{IJ} = \left\langle \frac{L^2\, U'(l)}{l} \right\rangle_L \int_{-\pi}^{\pi} \int_{0}^{\pi} \Xi_I\, \Xi_J\, \sin\theta\, d\theta\, d\phi = \left\langle \frac{L^2\, U'(l)}{l} \right\rangle_L \frac{4\,\pi}{3}\, \delta_{IJ}. \tag{2.99}$$

Using the bond density function from (2.76), the Cauchy stress is

$$\boldsymbol{\sigma} = \frac{4\,\pi\, D_0\, L_0^4}{3\,\Omega_0\,\lambda}\, \frac{U'(l)}{l}\, \mathbf{1}, \tag{2.100}$$

where the additional factor of the stretch $\lambda = l/L_0$ in the denominator implies the peak Cauchy stress occurs at the maximum value of $U'(l)\,/l^2$, not the maximum value of $U'(l)\,/l$ as was found for the plane stress model. Using the results from (2.95), the equitriaxial cohesive strength is given by

$$\sigma_c^* = \frac{4\, D_0\, L_0^4}{3\,\Omega_0}\, \frac{A\, B\, \pi}{e\,(L_0 + 2\, B)}. \tag{2.101}$$

The stress state ahead of a mode I crack front in three dimensions is better approximated as equibiaxial, plane strain rather than equitriaxial; however, an analytical estimate for the cohesive stress is not available for this case.

### 2.2.4 *J*-integral estimate of fracture energy

As demonstrated in the previous section, the onset of fracture predicted by the VIB model is not determined solely by the choice of bond potential, but also depends on the state of deformation in the localization zone. Similarly, the work to fracture cannot be determined by considering the bond potential alone. We can study the relationship between the parameters of the bond potential, the crack tip loading, and the fracture energy by making use of the $J$-integral[79, 26]. The results derived in this section also provide an approximate relationship to fit the VIB model parameters to experimentally determined fracture properties.

The finite elasticity form of the $J$-integral[26] expressed in the Lagrangian representation is

$$\boldsymbol{J} = \int_{\Gamma} \left(\Phi\, \mathbf{1} - \mathbf{F}^{\mathrm{T}}\mathbf{P}\right) \mathbf{N}\, d\Gamma, \tag{2.102}$$

where $\Gamma$ is a contour in the undeformed configuration surrounding the crack tip as shown in Figure 2.5(a), $\mathbf{N}$ is the outward normal to the contour, $\Phi$ is the strain energy density, $\mathbf{P}$ is the 1st Piola-Kirchhoff stress (A.21), and $\mathbf{F}$ is the deformation gradient (A.4). The energy release rate for crack extension is given by $J_1$. We assume that the crack grows by material failure along a strip of height $h$. In reality, the dimensions of the strip depend on the nature of the material being considered. In general, the height $h$ will be on the order of $L$, the characteristic length scale of

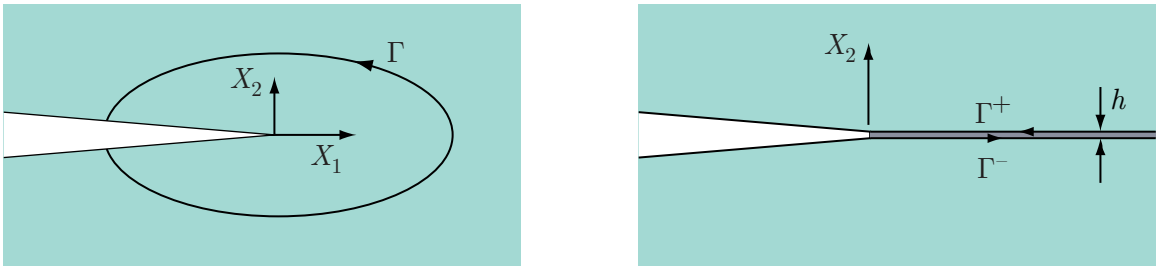


(a) (b)

Figure 2.5: $J$-integral contours (a) for an arbitrary path and (b) for a path surrounding a zone of localization with height $h$.

the microstructure. For crystalline materials, this dimension would be on the atomic scale while it could be on millimeter length scales for polymeric materials.

Because of the path independence of $J$, we can select a contour that lies along the upper and lower edges of the localization zone, denoted by $\Gamma^+$ and $\Gamma^-$ in Figure 2.5(b). The contours extend from the crack tip at $X_1 = 0$ to material remote from the tip as $X_1 \to \infty$. Along these contours, the normal vectors are $N_J^+ = \delta_{2J}$ and $N_J^- = -\delta_{2J}$, reducing the $J$-integral expression (2.102) to

$$J_1 = -\int_0^\infty \left[ (P_{i2}F_{i1})^+ - (P_{i2}F_{i1})^- \right] dX_1. \tag{2.103}$$

Within a finite deformation setting, it is difficult to make general assumptions about the character of the stress and deformation fields unless the loading is chosen to be highly symmetric. If we restrict our analysis to mode I loading, the stress field will be symmetric about the crack plane to give $\mathbf{P}^+ = \mathbf{P}^-$. Using this assumption and expressing $\mathbf{F}$ in terms of the displacement field, we can rewrite $J_1$ as

$$J_1 = -\int_0^\infty \left[ P_{22} \frac{\partial \left( u_2^+ - u_2^- \right)}{\partial X_1} + P_{12} \frac{\partial \left( u_1^+ - u_1^- \right)}{\partial X_1} \right] dX_1. \tag{2.104}$$

The displacement field will also be symmetric about the crack plane, which yields the relation $u_1^+ = u_1^-$. Adopting the notation $\Delta u_2(X_1) = u_2^+ - u_2^-$ to represent the separation across the localization strip, $J_1$ becomes

$$J_1 = \int_0^\infty P_{22}\, d(\Delta u_2), \tag{2.105}$$

where the limits of integration have been determined by prescribing $\Delta u_2(0) \to \infty$ as the material reaches complete failure and $\Delta u_2(X_1 \to \infty) = 0$ in the material far ahead of the tip.

The height of the localization strip enters the analysis when we express the separation in terms of stretch, yielding

$$\Delta u_2 = (\lambda_2 - 1)\, h \qquad \text{and} \qquad d\left(\Delta u_2\right) = h\, d\lambda_2. \tag{2.106}$$

With this change of variables, the expression for $J_1$ at a mode I crack tip is

$$J_1 = h \int_1^\infty P_{22}\, d\lambda_2. \tag{2.107}$$

This result reaffirms the well known result that the appearance of localization, in the form of crack extension for this case, introduces a length scale dependence into the observed behavior. From the perspective of dimensional analysis, a length scale must enter the description of fracture since the VIB model describes only the strain energy density, stress, or modulus at a point, with units of energy per volume, while the fracture energy has units of energy per area. The fact that the VIB model does not provide a characteristic length scale for the localization zone creates difficulties in numerical modeling. For example, the spatial discretization in finite element modeling introduces a length scale that is not related to the material's intrinsic length scale, unless the element dimensions approach the length scale of the microstructure. Even for this case, the mesh still produces anisotropy in the fracture energy since the effective width of an element is not the same for all orientations. Localization naturally occurs in a region of the mesh one element wide. In the absence of an intrinsic length scale, the displacement jump produced by the opening of fracture surfaces represents a singularity in the strain field. This description of localized modes of deformation has been applied to the study shear bands resulting from plasticity models exhibiting softening[3]. Unless enhancements are introduced into the finite element shape functions to capture these sharp features in the displacement field, they will appear in the solution as sharply as can be represented: localized deformation in the elements with the smallest characteristic dimension. From a physical point of view, fracture along a trajectory with the smallest effective localized width represents the path of least resistance for a crack since this requires the least amount of energy. With the present VIB model, the characteristic element size in the fracture region must be selected in conjunction with the VIB parameters in order to produce the desired fracture energy. A more difficult problem to remedy is the anisotropy of the fracture energy resulting from mesh orientation. The source of this fracture energy anisotropy is illustrated in Figure 2.6. Depending

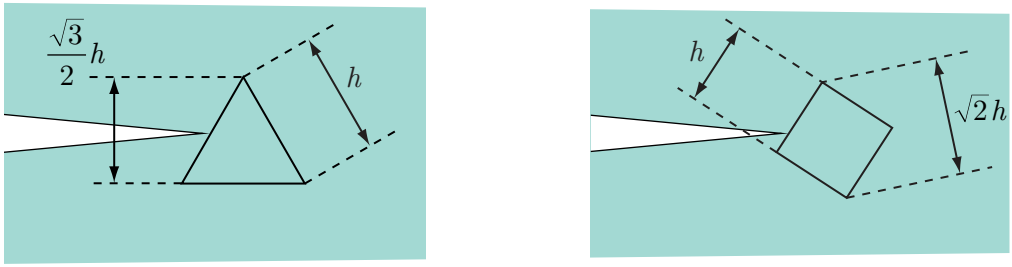


Figure 2.6: Fracture energy anisotropy due element geometry and orientation showing the effective height of the elements in terms of the characteristic dimension $h$.

on the element geometry and orientation, the effective height of the localization zone changes with the direction in which the crack propagates. Since the fracture energy is proportionate to this height, we would expect the crack propagation direction to be influenced by the near tip mesh arrangement. Ultimately, a length scale must be introduced into the VIB model. Otherwise, the localized deformations must be governed with constitutive properties other than the stress-strain

relations from the model. We have just begun investigating this latter approach of coupling cohesive bulk models with cohesive surface models in a single complementary approach to modeling fracture.

Although the work to fracture (2.107) is an integral over the stretch normal to the crack plane, the $P_{22}$ component of the 1st Piola-Kirchhoff stress depends on the entire deformation. In order to arrive at some relations between the constitutive model parameters and the fracture energy, we consider the case of equibiaxial stretching ($\lambda_1 = \lambda_2 = \lambda$) with the plane stress VIB model using the potential described in Section 2.2.2. This state of deformation generates the equibiaxial Cauchy stress given by (2.97). Noting that the stretched length is $l = \lambda L$ and using the stress relations given by (A.25), we can express $J_1$ as

$$J_1 = \frac{\pi h D_0 L_0^3}{\Omega_0} \int_1^\infty U'(l)\, d\lambda. \tag{2.108}$$

A change of variables produces

$$J_1 = \frac{\pi h D_0 L_0^2}{\Omega_0} U(l) \Big|_{L_0}^\infty = -\frac{\pi h D_0 L_0^2 U_0}{\Omega_0} = G^*, \tag{2.109}$$

where we have assumed the potential has the general features $U(L_0) = U_0$ and $U(l \to \infty) = 0$, as shown in Figure 2.3. Although the assumption of equibiaxial stretching made in deriving (2.109) will not hold for a general case of crack extension, $G^*$ does provide some guidance in fitting bond potential parameters with experimental measurements.

Restricting our consideration to the two-dimensional model provides the opportunity to investigate how the fracture energy changes as a function of the assumed deformation state in the localizing zone. With deformation in the crack opening direction controlled by $\lambda_2$, we can vary $\lambda_1$ to see the effect of stretching the material along the crack propagation direction. The form of $J_1$ in (2.107) shows that the fracture energy is determined by the work done against the resistance in the material to deformation in the $X_2$ direction. However, the $P_{22}$ stress generated in the material is a function of the total deformation. The work done by deformation in the $X_1$ direction does not contribute to the fracture energy explicitly, but has the effect of "weakening" the ability of bonds in certain orientations to resist the deformation leading to fracture. During an actual fracture process, $\lambda_1$ would vary according to boundary conditions and specimen geometry. In order to demonstrate the effect of the deformation state on the fracture energy, we prescribe the stress ratio $\sigma_{11}/\sigma_{22}$ or the ratio of the Green strains $E_{11}/E_{22}$ to remain constant during the fracture process. The history of $\lambda_1$ during the fracture process for different values of these ratios is shown in Figure 2.7 for $B/L = 0.05$. The stress ratio is varied from $\sigma_{11}/\sigma_{22} = 0$, corresponding to uniaxial stress, to $\sigma_{11}/\sigma_{22} = 1$, corresponding to an equibiaxial stress state. The ratio in the strains varies over the same range, corresponding to deformations from uniaxial stretching to equibiaxial stretching. The figure shows that only the curves for $\sigma_{11}/\sigma_{22} = E_{11}/E_{22} = 1$ coincide, and then only up to the point at which the cohesive stress is reached. We would expect this result since the material is isotropic, so that equibiaxial stretching leads to equibiaxial stress. As the cohesive limit is exceeded, the material in the stress-controlled calculations is allowed to relax in the $X_1$ direction rather than continuing along a path of equibiaxial deformation. These paths, which prescribe unloading in the material along the propagation direction, more closely resemble the material behavior during fracture than do the strain-prescribed paths of deformation.

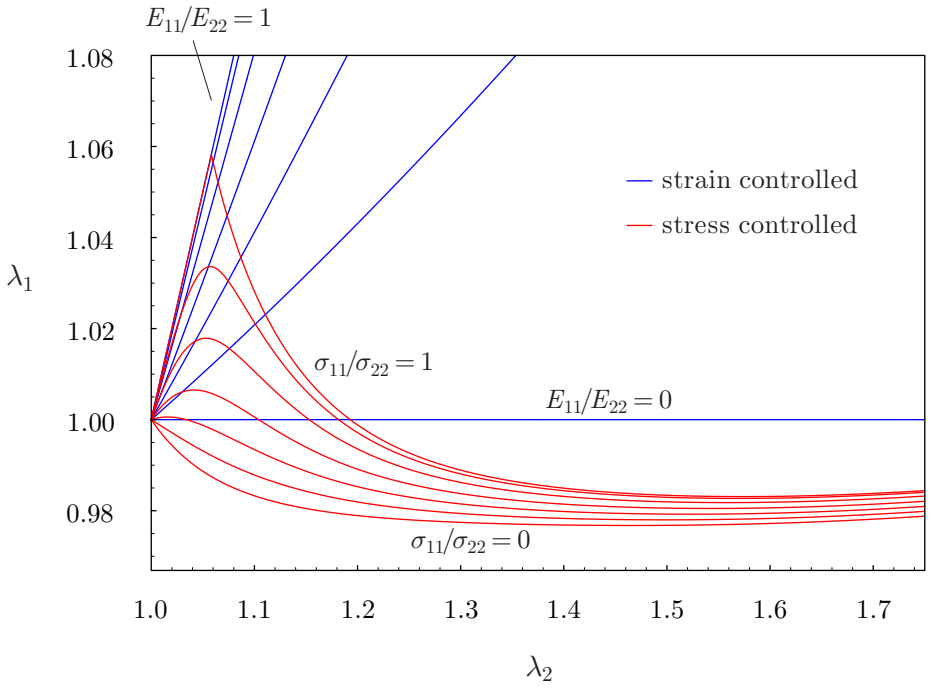


Figure 2.7: The history of $\lambda_1$ through the fracture process as a function of increasing $\lambda_2$, for prescribed stress ratios $\sigma_{11}/\sigma_{22}$ and strain ratios $E_{11}/E_{22}$ of $\{0.0, 0.2, 0.4, 0.8, 0.94, 1.0\}$ for $B/L = 0.05$.

The fracture energy computed from (2.107) over the range of stress and strain ratios shown in Figure 2.7 is depicted in Figure 2.8 for a range of values for $B/L$. For each assumed state of deformation, the fracture energy is evaluated with an adaptive scheme which employs Richardson extrapolation to provide an estimate of the quadrature error. The tolerance on the error was adjusted to yield convergence in the numerical integration to within machine precision. Figure 2.8 shows that $G^*$ from (2.109) represents a lower bound on the energy required to produce fracture in the plane stress, isotropic VIB model. The fracture energy increases as the assumed deformation changes from equibiaxial strain to uniaxial strain. As described earlier, we would expect this increase in the fracture energy since the effect of "weakening" in the bonds due to the $X_1$ deformation is decreasing. Surprisingly, the fracture energy for prescribed uniaxial strain is identical to the fracture energy for prescribed uniaxial stress although the histories of the total deformation for these cases is very different. The fracture energy continues to increase as the ratio in the stresses varies from uniaxial stress to equibiaxial stress. As an approximation to an actual fracture process, the stress controlled states of deformation are more realistic than the strain controlled states since they allow the material to relax perpendicular to the crack opening direction once the cohesive stress has been attained, as shown in Figure 2.7. Therefore, we expect the plane stress, isotropic VIB model to exhibit a fracture energy of 1.8 to 1.9 $G^*$ in numerical simulations of fracture. The results in the figure also show that the normalized fracture energy $G/G^*$ does not vary as a function of $B/L$ for deformation with a prescribed ratio of Green strains. For deformation with a prescribed ratio of Cauchy stress, the results display a decrease in $G/G^*$ as $B/L$ increases from 0.02 to 0.20.

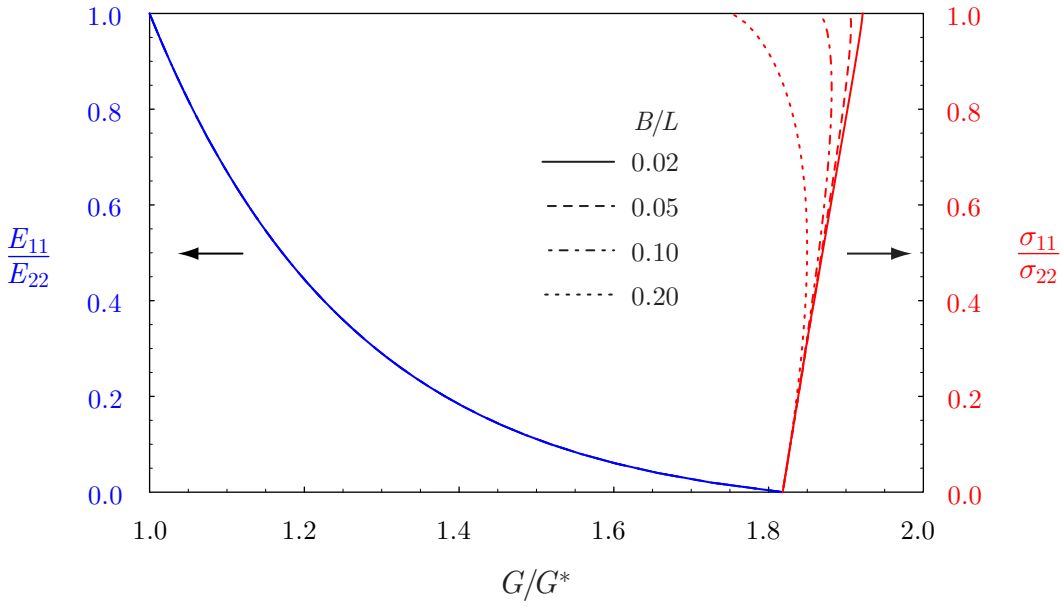


Figure 2.8: Variation in fracture energy $G$ with assumed deformation state $(E_{11}/E_{22}, \sigma_{11}/\sigma_{22})$ during fracture.

### 2.2.5 Failure indicators

The promise of cohesive modeling is the ability to produce fracture in numerical simulations without requiring an imposed failure criterion. Failure occurs as a natural consequence of the cohesive formulation, which embeds a finite strength and fracture energy in the material model. Although we are not required to impose a failure *criterion*, we do need to identify a failure *indicator*. With classical fracture theory, conditions for crack propagation are posed as a threshold criterion that clearly defines the point at which failure occurs. With a cohesive view of material, failure proceeds in a much more gradual manner. The material does not simply fail, but exhibits a complete history of response from the undeformed state through the cohesive limit to complete failure.

In selecting a failure indicator, we choose to associate it with a threshold condition that corresponds to reaching the cohesive limit rather than a cut-off condition when the stresses being sustained by the material are deemed insignificant. Hill[40] has described the loss of strong ellipticity of the strain energy density function as an indication of the loss of stability of a solid. The analysis is related to the eigenvalues of the acoustical tensor $\mathbf{q}(\mathbf{N})$ (A.31). The loss of strong ellipticity coincides with a loss of uniqueness in the solutions of the governing equation of elastodynamics (A.28). The discontinuous modes of deformation that become admissible with the loss of strong ellipticity appear across a characteristic surface, which we describe with the normal $\mathbf{N}^*$ in the undeformed configuration. With the loss of strong ellipticity produced by models of plasticity exhibiting softening, these characteristic surfaces are associated with slip, or shear, bands. In the present context, we associate these characteristic surfaces with highly localized bands of deformation that become new crack faces as the material reaches complete failure.

We also study the behavior of a second failure indicator that is related more directly with the

cohesive strength than is the analysis of the acoustical tensor. Since the bond density functions of the VIB model are defined with respect to the undeformed configuration, the 1st Piola-Kirchhoff stress $\mathbf{P}$ is related to the force generated by the network of virtual bonds. The maximum values of $\mathbf{P}$ corresponds to the largest forces that can be sustained by the bonds of the virtual microstructure.

The onset of failure indicated by these two criteria as a function of the state of deformation is shown in Figure 2.9 for the plane stress, isotropic VIB model. The configuration of the imposed

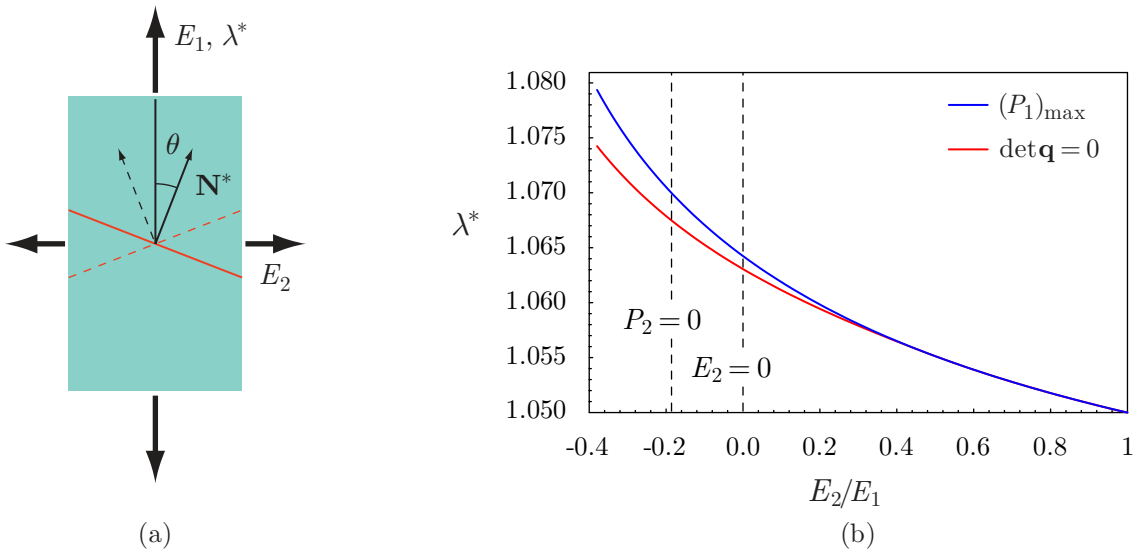


Figure 2.9: (a) Geometry of the loading configuration and (b) a comparison of failure indicators for the plane stress, isotropic VIB model as a function of the state of deformation.

deformation is shown in Figure 2.9(a). The deformation is characterized by $E_1/E_2$, the ratio of the principal values of the Green strain, where $E_1$ and $E_2$ are the strains along and perpendicular to the primary loading direction, respectively. The normal to the characteristic surface associated with the loss of strong ellipticity is shown as $\mathbf{N}^*$. Figure 2.9(b) illustrates how the two criteria differ in indicating the onset of failure as a function of the state of deformation for $B/L = 0.05$ using the model interaction potential from Section 2.2.2. The stretch in the primary loading direction at the point of failure is designated as $\lambda^*$. The deformation states for uniaxial stress ($P_2 = 0$) and uniaxial strain ($E_2 = 0$) are indicated in the figure. For $E_2/E_1 < 0.3$, the loss of strong ellipticity clearly occurs at a smaller stretch than the stretch required to reach the maximum value of $P_1$. In this regime, the maximum value of $P_1$ attained at $\lambda^*$ in the figure is unreachable since homogeneous states of deformation become unstable once the acoustical tensor is non-positive definite. As the imposed deformation becomes more nearly equibiaxial, the critical stretches for the two criteria converge. For $E_2/E_1 > 0.3$, the two curves in the figure are nearly indistinguishable. For the equibiaxial case, both criteria indicate the onset of failure at $\lambda^* = B/L$, the stretch for which the bond force is maximal.

Figure 2.10 shows the orientation of the characteristic surface with normal $\mathbf{N}^*$ as a function of the state of deformation. The angle $\theta^*$ is measured from the axis of primary loading, as indicated in Figure 2.9(a). States of deformation corresponding to uniaxial stress and strain are indicated in the figure. The key result of these calculations is that the characteristic surface associated

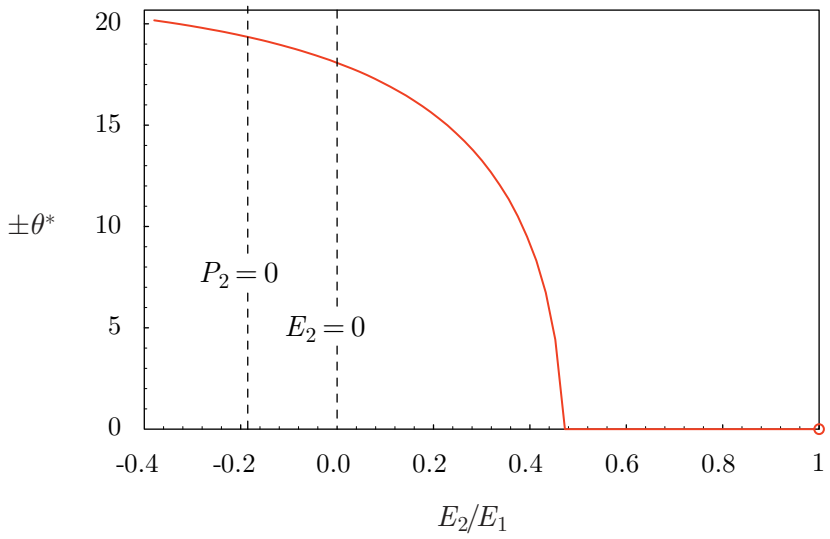


Figure 2.10: Orientation of the localized band as a function of the state of deformation.

with the loss of strong ellipticity is oriented perpendicular to the primary loading direction for imposed deformations approaching the equibiaxial state, $E_2/E_1 > 0.5$ in the figure. From the asymptotic crack tip solutions of linear elasticity, we know that the state of equibiaxial stretching resembles the deformation a material particle experiences in front of a mode I crack tip. Therefore, it is encouraging that the direction of crack growth indicated by $\mathbf{N}^*$ matches our expectations for the direction of propagation of a mode I crack. Under mixed-mode conditions, classical fracture theory requires that we postulate a crack propagation direction. Typically, one prescribes crack propagation in the locally mode I direction, the orientation for which $K_{II} = 0$. Alternatively, one could select the direction corresponding to the largest hoop stress $\sigma_{\theta\theta}$ surrounding the crack tip. Since the mechanisms of material failure are not well understood, the most appropriate choice for the direction of crack propagation is also unclear.

With the VIB model, the fracture characteristics under mixed-mode conditions are embedded in the constitutive behavior. Once the parameters in model have been selected, no additional criteria need to be imposed in order to reproduce a wide variety of fracture phenomena. As shown in Figures 2.9 and 2.10, the loss of strong ellipticity appears to be an appropriate indicator of the onset of failure. For loading with mode I character, it agrees with our expectation for failure to initiate as the stress in the material approaches the cohesive limit and for crack propagation to occur in the direction perpendicular to the direction of the largest stress.

# 3 Application of meshfree methods to modeling fracture

Recently, there has been intense interest in the development of meshfree numerical simulation methods. The advantages we see for using meshfree methods to model fracture and fragmentation are outlined in Section 1.3. The methods used in this study have their origins in Smoothed Particle Hydrodynamics (SPH) proposed by Gingold and Monaghan[36]. A number of methods have developed that employ variants of the Moving Least Squares fitting procedure of Lancaster and Salkauskas[52]. These include, but are not limited to, the Diffuse Element Method of Nayroles *et al.* [65], the Element Free Galerkin method of Belytschko *et al.* [10], the Reproducing Kernel Particle Method of Liu and Chen[56], and the Meshless Local Petrov-Galerkin method of Atluri and Zhu[4]. A number of overviews and reviews have appeared regarding these methods[9, 59, 58, 60, 61], though the interested reader will find no shortage of new developments.

## 3.1 Reproducing Kernel Particle Method (RKPM)

RKPM belongs to class of methods for which the approximation, or "image", of a signal is given by a kernel expression. Without loss of generality, we can consider the expression for the approximation in one dimension

$$u^{R_a}(x) = \int_{-\infty}^{+\infty} \phi_a(x-y)\ u(y)\ dy, \tag{3.1}$$

where $\phi_a$ is alternately called a weight, kernel, or smoothing function. From the analogy to signal processing, $\phi_a$ may be viewed as a customizable low pass filter between the original signal, or data, $u(y)$ and its reproduced image. This function is positive, even, and has compact support characterized by the dilation parameter $a$. Liu and Chen[56] improved the accuracy of the method by modifying the window function with a correction to yield a reproducing condition as

$$u^{R_a}(x) = \int_{-\infty}^{+\infty} \overline{\phi}_a(x-y)\ u(y)\ dy, \tag{3.2}$$

where the modified window function

$$\overline{\phi}_a(x-y) = C(x;x-y)\ \phi_a(x-y) \tag{3.3}$$

incorporates the polynomial

$$C(x;x-y) = b_0(x) + b_1(x)\ (x-y) + b_2(x)\ (x-y)^2 + \ldots + b_m(x)\ (x-y)^m \tag{3.4}$$

which ensures that the approximation can exactly represent polynomials of order $m$. In general, we may express the correction function as

$$C(\mathbf{x};\mathbf{x}-\mathbf{y}) = \mathbf{b}(\mathbf{x}) \cdot \mathbf{P}(\mathbf{x}-\mathbf{y}) \tag{3.5}$$

where $\mathbf{P}$ is a basis of polynomials that possess the desired degree of completeness and $\mathbf{b}(\mathbf{x})$ is an vector of unknown coefficients determined from the reproducing condition (3.2). The requirement that each member of the basis be reproduced follows from (3.2) as

$$\mathbf{P}(\mathbf{0}) = \int_{-\infty}^{+\infty} \mathbf{b}(\mathbf{x}) \cdot \mathbf{P}(\mathbf{x}-\mathbf{y})\ \phi_a(\mathbf{x}-\mathbf{y})\ \mathbf{P}(\mathbf{x}-\mathbf{y})\ d\mathbf{y}. \tag{3.6}$$

The vector of coefficients follows as

$$\mathbf{b}(\mathbf{x}) = \mathbf{M}_a^{-1}(\mathbf{x})\,\mathbf{P}(\mathbf{0})\,, \tag{3.7}$$

where

$$\mathbf{M}_a(\mathbf{x}) = \int_{-\infty}^{+\infty} \mathbf{P}(\mathbf{x}-\mathbf{y}) \otimes \mathbf{P}(\mathbf{x}-\mathbf{y})\ \phi_a(\mathbf{x}-\mathbf{y})\, d\mathbf{y} \tag{3.8}$$

is known as the moment matrix. Using the result from (3.7), the reproducing condition (3.2) can be written as

$$\mathbf{u}^{R_a}(\mathbf{x}) = \int_{-\infty}^{+\infty} \mathbf{b}(\mathbf{x}) \cdot \mathbf{P}(\mathbf{x}-\mathbf{y})\, \phi_a(\mathbf{x}-\mathbf{y})\ \mathbf{u}(\mathbf{y})\ d\mathbf{y}. \tag{3.9}$$

First and higher order gradients of the field representation follow from (3.7)–(3.9) through simple differentiation. For clarity, we present the expressions for derivatives. We note that these derivatives may be evaluated exactly though some early work in the meshfree field advocated approximate expressions for these derivatives[65]. The gradient of the field may be expressed as

$$\begin{aligned}\frac{\partial \mathbf{u}^{R_a}(\mathbf{x})}{\partial \mathbf{x}} = \int_{-\infty}^{+\infty} \mathbf{u}(\mathbf{y}) \otimes \Bigg[ & \frac{\partial \mathbf{b}(\mathbf{x})}{\partial \mathbf{x}}\ \mathbf{P}(\mathbf{x}-\mathbf{y})\ \phi_a(\mathbf{x}-\mathbf{y}) + \\ & \mathbf{b}(\mathbf{x})\ \frac{\partial \mathbf{P}(\mathbf{x}-\mathbf{y})}{\partial \mathbf{x}}\, \phi_a(\mathbf{x}-\mathbf{y}) + \\ & \mathbf{b}(\mathbf{x}) \cdot \mathbf{P}(\mathbf{x}-\mathbf{y})\ \frac{\partial \phi_a(\mathbf{x}-\mathbf{y})}{\partial \mathbf{x}} \Bigg]\, d\mathbf{y},\end{aligned} \tag{3.10}$$

where the gradient of the coefficient vector

$$\frac{\partial \mathbf{b}(\mathbf{x})}{\partial \mathbf{x}} = -\mathbf{M}_a^{-1}(\mathbf{x})\, \frac{\partial \mathbf{M}_a(\mathbf{x})}{\partial \mathbf{x}}\, \mathbf{b}(\mathbf{x}) \tag{3.11}$$

follows from (3.7) making use of the relation

$$\frac{\partial \left[\mathbf{M}_a^{-1}\right]_{ij}}{\partial x_k} = -\left[\mathbf{M}_a^{-1}\right]_{ir} \frac{\partial \left[\mathbf{M}_a\right]_{rs}}{\partial x_k}\ \left[\mathbf{M}_a^{-1}\right]_{sj}. \tag{3.12}$$

Higher-order gradients may be calculated by further differentiation of (3.10)–(3.12). Notably, the expressions for the representation of the unknown field variables are general for an arbitrary number of field and spatial dimensions, including the expressions for the first and higher order gradients of the field.

In evaluating the representations for the field numerically, we discretize the integrals in the previous expressions. The discrete reproducing condition follows from (3.9) as

$$\mathbf{u}^{R_a^h}(\mathbf{x}) = \sum_{I=1}^{N_p} \mathbf{b}(\mathbf{x}) \cdot \mathbf{P}(\mathbf{x}-\mathbf{x}_I)\, \phi_a(\mathbf{x}-\mathbf{x}_I)\ \mathbf{u}_I\, \Delta V_I, \tag{3.13}$$

where $N_p$ is the number of sampling points, or particles, under consideration, and $\mathbf{x}_I$, $\mathbf{u}_I = \mathbf{u}(\mathbf{x}_I)$, and $\Delta V_I$ are the coordinates, field value, and integration weight (volume) associated with particle $I$, respectively. From (3.13), we can identify the RKPM nodal shape functions as

$$\mathbf{u}^{R_a^h}(\mathbf{x}) = \sum_{I=1}^{N_p} \Phi_{aI}(\mathbf{x})\ \mathbf{u}_I, \tag{3.14}$$

where

$$\Phi_{aI}(\mathbf{x}) = \mathbf{b}(\mathbf{x}) \cdot \mathbf{P}(\mathbf{x} - \mathbf{x}_I)\, \phi_a(\mathbf{x} - \mathbf{x}_I)\ \Delta V_I. \tag{3.15}$$

Unlike the shape functions derived for standard finite element methods, the RKPM shape functions (3.15) do not in general possess the so-called Kronecker delta property, that is

$$\Phi_{aI}(\mathbf{x}_J) \neq \delta_{IJ}. \tag{3.16}$$

The lack of this property complicates the enforcement of essential boundary conditions. Furthermore, this characteristic affects the enforcement of contact constraint and the imposition of cohesive tractions. The applications of cohesive surface formulations to meshfree methods in discussed in Section 3.3.

## 3.2 Representation of cracks in a meshfree domain

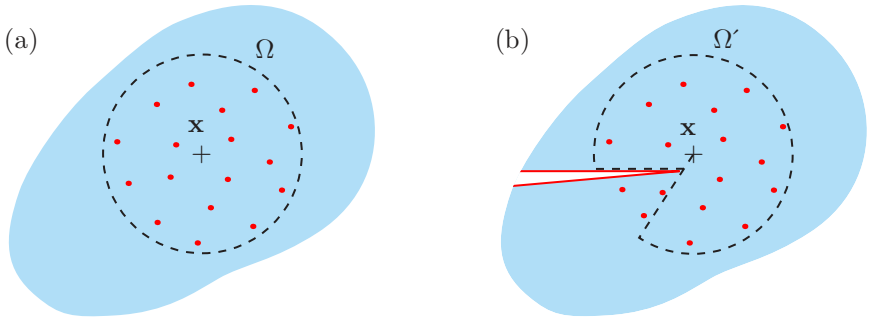


Figure 3.1: Adaptivity inherent in meshfree methods applied to resolving changes in the contributions to the field at point $\mathbf{x}$ due to an advancing crack tip using the "visibility" criterion.

With standard finite element formulations, the displacement field at any point $\mathbf{u}(\mathbf{x})$ is represented with Lagrange polynomials that interpolate the values from nodes arranged in pre-defined sets ("elements") with selected topologies (quadrilaterals, tetrahedra, etc.). In contrast to this fixed construction, meshfree methods represent the displacement field at any point $\mathbf{x}$ as a linear combination of contributions from an arbitrarily arranged set of nodes in the neighborhood of $\mathbf{x}$, as expressed in (3.14). This set of nodes is depicted within the region $\Omega$ in Figure 3.1(a). Propagation of a crack, or any other source of a displacement field discontinuity, may be represented by excluding from the neighborhood any regions separated from $\mathbf{x}$ by the line of discontinuity. The modified neighborhood this produces is denoted as $\Omega'$ in Figure 3.1(b). As the observation point $\mathbf{x}$ translates around the tip, the neighborhood varies constantly due to the crack, producing a

representation of the displacement field that is discontinuous across the crack path. This so-called "visibility" criterion for determining the domain of influence for a particular node was developed by Belytschko *et al.* [10] in conjunction with the Element-Free Galerkin (EFG) method. This method of generating a discontinuity has been to simulate crack growth with classical approaches to fracture mechanics under both dynamic and static conditions two dimensions[11, 62, 13], as well as under dynamic conditions in three dimensions[51]. Belytschko *et al.* [9] describe that this construction leads to discontinuities in the shape functions of nodes whose support is only partially "cut". When a line of discontinuity passes entirely through the support of a node, its shape function is continuous, though the field represented by a shape function expansion over all nodes will possess a discontinuity. Galerkin methods are normally constructed to require no discontinuities of the first kind; however, Krysl and Belytschko[50] have shown that these shape functions may lead to convergent solutions. Organ *et al.* [68] develop methods by which these discontinuities in the nodal shape functions can be avoided by diffracting the "line of sight" around the crack front rather than terminating a node's influence abruptly.

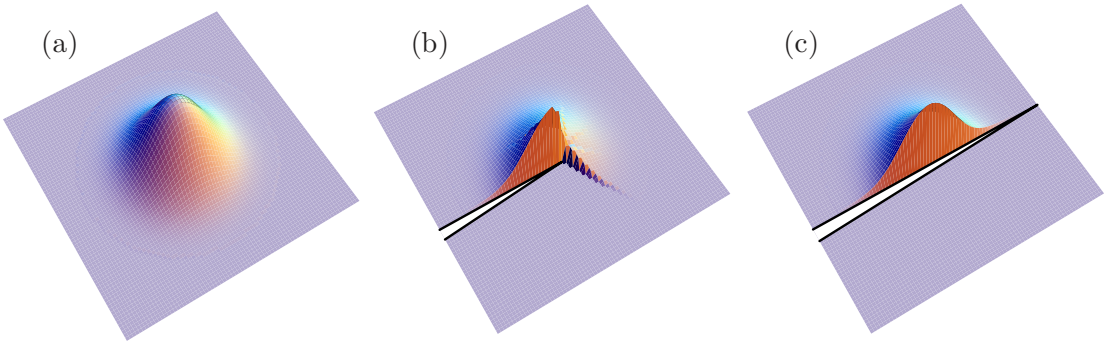


Figure 3.2: The evolution of an RKPM shape function with the propagation of a line of discontinuity.

Figure 3.2 shows how a shape function is altered by the presence of an imposed line of discontinuity. The changes are due to application of the simple "visibility" condition. The partially cut shape function in Figure 3.2(b) displays some of the nonsmoothness that Organ *et al.* remove with their diffraction approach. The completely cut shape function in Figure 3.2(c) demonstrates how discontinuities in the displacement field are represented by modification of the shape functions. The supports of cut shape functions do not extend over the line of discontinuity. Therefore, the displacement field on either side of the cut is independent of the particles on the other. Using this construction, we represent cracks with sets of line segments in two dimensions and surfaces subdivided into triangular and quadrilateral facets. This representation can treat multiple, intersecting cracks as long as the arrangement of fracture surfaces does not isolate any field points from coverage by the minimum number nodal support needed to calculate the shape functions.

## 3.3 Cohesive surfaces in a meshfree domain

Section 2.1.1 presents a general formulation of the nodal force vector and tangent stiffness matrix for cohesive surface elements. In order to apply the formulation with a meshfree representation of the displacement field, we need to modify our definitions of the reference and current configurations as

well as our definition of the opening displacement. In doing so, we have investigated two approaches to projecting the tractions across the facets of the cohesive elements onto the particles of the meshfree domain. We prefer the approach described in Section 3.3.1. This approach is consistent with the meshfree definition of the opening displacement and does not require introducing any additional degrees of freedom as cohesive elements are inserted. The approach we describe in Section 3.3.2 involves inserting pairs of particles along the fracture surface and constructing a finite element-like representation of the deformed configuration.

### 3.3.1 Consistent projection of cohesive tractions

One of the principal advantages of meshfree methods is that we can readily construct a representation of the displacement field and its derivatives at any point within the meshfree domain. Using this representation, we can transform the cohesive tractions into consistent nodal forces without introducing additional particles, as is required by the approach outlines in Section 3.3.2. The geometry of a cohesive surface in a meshfree domain is illustrated in Figure 3.3. In order to integrate

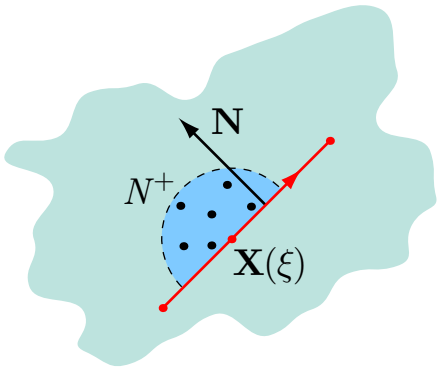


Figure 3.3: Undeformed configuration of a cohesive surface with parameterization $\mathbf{X}(\boldsymbol{\xi})$ and normal $\mathbf{N}$ in a meshfree domain showing the neighborhood $N^+$ a field point on the "upper" face.

the cohesive tractions, we must define a parameterization which uniquely defines the geometry of the cohesive surface in the undeformed configuration. Section 3.2 describes how cracks in a meshfree domain are represented by collections of cutting facets, line segments in two dimensions, and triangular or quadrilateral surface segments in three dimensions. These cutting facets can be introduced anywhere within the meshfree domain. The geometry of the cutting facets is defined in the undeformed configuration.

Given the coordinates of arbitrary points within the domain, we can define a parameterization of the cutting facet using standard finite element shape functions

$$\mathbf{X}(\boldsymbol{\xi}) = \sum_{A=1}^{N^s} \Phi_A^{\mathrm{FE}}(\boldsymbol{\xi})\ \mathbf{X}_A, \tag{3.17}$$

where $N^s$ is the number of facet points. The points defining the surface do not coincide with particles. That is, there are no degrees of freedom associated with the points defining the geometry of the cutting surfaces. The shape functions $\Phi_A^{\mathrm{FE}}$ in (3.17) serve only to provide a unique mapping

from $\boldsymbol{\xi}$ to points lying on the surface. In Section 2.1.1, we defined the opening displacement as

$$\begin{aligned}\boldsymbol{\Delta}(\boldsymbol{\xi}) &= \mathbf{u}^+(\boldsymbol{\xi}) - \mathbf{u}^-(\boldsymbol{\xi}) \\ &= \sum_{A\in N^+} \Phi_A(\boldsymbol{\xi})\,\mathbf{u}_A - \sum_{A\in N^-} \Phi_A(\boldsymbol{\xi})\,\mathbf{u}_A,\end{aligned} \tag{2.4}$$

where the surface normal $\mathbf{N}(\boldsymbol{\xi})$ sets its sense. Within a standard finite element framework, the opening displacement depends only on the nodes on the surface. Therefore, the projection of tractions resulting from $\frac{\partial \boldsymbol{\Delta}}{\partial \mathbf{u}_A}$ in (2.7) only produces forces on surface nodes. As shown in Figure 3.3, the meshfree representation of the displacement field along the "upper" facet involves the truncated neighborhood of all nodes whose support covers $\mathbf{X}^+(\boldsymbol{\xi})$. The meshfree shape functions $\Phi_A(\mathbf{X}^+(\boldsymbol{\xi}))$ in (2.4) are given by (3.15) though the subscript $a$, denoting the dilation parameter, has been omitted. To use the expressions for the force vector and tangent stiffness from Section 2.1.1 with meshfree methods, we need to modify the expression for the element mid-plane that defines the transformation $\mathbf{Q}$ in (2.1) and (2.3) into and out of the local coordinates of the surface elements. The expression for the mid-plane from (2.15) becomes

$$\mathbf{x}(\boldsymbol{\xi}) = \sum_{A=1}^{N^s} \Phi_A^{\mathrm{FE}}(\boldsymbol{\xi})\ \mathbf{X}_A + \frac{1}{2}\left(\sum_{A\in N^+} \Phi_A(\mathbf{X}(\boldsymbol{\xi}))\ \mathbf{u}_A + \sum_{A\in N^-} \Phi_A(\mathbf{X}(\boldsymbol{\xi}))\ \mathbf{u}_A\right), \tag{3.18}$$

which combines the finite element shape functions for the parameterization of the undeformed configuration from (3.17) with the meshfree shape functions $\Phi_A$ of the displacement field along the upper and lower facets of the element. The jacobian of the surface parameterization may be written as

$$\frac{\partial \mathbf{x}(\xi)}{\partial \boldsymbol{\xi}} = \frac{\partial \mathbf{X}(\boldsymbol{\xi})}{\partial \boldsymbol{\xi}} + \frac{1}{2}\left(\sum_{A\in N^+} \mathbf{u}_A \otimes \frac{\partial \Phi_A(\mathbf{X})}{\partial \mathbf{X}} + \sum_{A\in N^-} \mathbf{u}_A \otimes \frac{\partial \Phi_A(\mathbf{X})}{\partial \mathbf{X}}\right) \frac{\partial \mathbf{X}(\boldsymbol{\xi})}{\partial \boldsymbol{\xi}}, \tag{3.19}$$

where the chain rule applied to the term involving the displacement field is needed since the meshfree shape functions are defined in terms of the particle coordinates in the undeformed configuration. The jacobian of the reference configuration follows from (3.17) as

$$\frac{\partial \mathbf{X}(\boldsymbol{\xi})}{\partial \boldsymbol{\xi}} = \sum_{A=1}^{N^s} \mathbf{X}_A \otimes \frac{\partial \Phi_A^{\mathrm{FE}}(\boldsymbol{\xi})}{\partial \boldsymbol{\xi}}. \tag{3.20}$$

To complete the formulation of the tangent stiffness of the consistent projection, we need to consider the derivative of the jacobian of the surface transformation $\frac{\partial \mathbf{x}}{\partial \boldsymbol{\xi}}$, needed in (2.20) for the two-dimensional case and (2.29)–(2.31) and (2.34) for the three-dimensional case. The derivative

$$\frac{\partial^2 x_i}{\partial u_{kA} \partial \xi_j} = \frac{\partial \Phi_A}{\partial X_r}\,\frac{\partial X_r}{\partial \xi_j}\,\delta_{ik} \tag{3.21}$$

follows from (3.19) for $A$ in $N^+$ and $N^-$ for particles the upper and lower facets, respectively. Because meshfree shape functions are used in the expression of the opening displacement (2.4) and the mid-plane surface (3.18), the projection of cohesive tractions onto the nodes produces

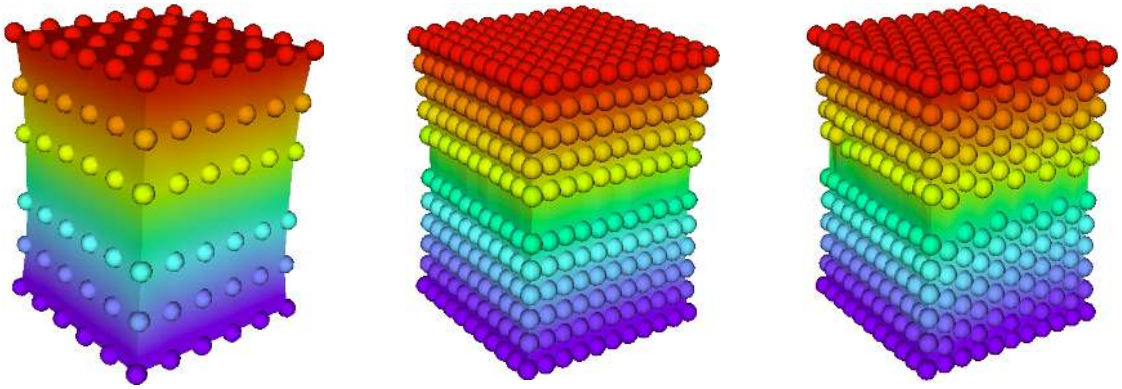

(a) (b) (c)

Figure 3.4: Three-dimensional calculations of the uniaxial extension of a prismatic bar for three different particle distributions, shaded by contours of displacement.

forces that extend some depth into the bulk. This differs from the results for cohesive surfaces in a standard finite element setting and from the surface project for meshfree methods described in Section 3.3.2, but is consistent with the meshfree representation of the displacement field.

To verify the formulation of cohesive surfaces in a meshfree domain, we performed a series of fully three-dimensional calculations of uniaxial extension of a prismatic bar. The three different particle arrangements are shown in a deformed state in Figure 3.4. For the case illustrated in Figure 3.4 (a), the cubic domain contains $6 \times 6$ particles on a regular hexahedral grid of integration cells. Figure 3.4 (b) shows the domain containing $11 \times 11$ particles on a regular hexahedral grid, while Figure 3.4 (c) shows 1549 particles on a grid of unstructured tetrahedral integration cells. For each case, a planar layer of quadrilateral cohesive surface elements in a regular $2 \times 2$ arrangement is inserted at the mid-height. A $3 \times 3$ Gauss rule is used to integrate element force and stiffness. The cohesive relation proposed by Xu and Needleman[95] (see Section 2.1.2) governs the evolution of tractions over the surfaces. The critical opening displacement $\delta_n$ in the cohesive relation is selected as $\frac{L}{100}$, where $L$ is the cube dimension. The bulk behavior is modeled with an isotropic, finite deformation constitutive model that displays a Young's modulus $E$ and Poisson's ratio $\nu = \frac{1}{4}$ under infinitesimal deformations. Uniform displacements are imposed on the particles of the upper and lower surfaces. These particles are also held fixed in the transverse directions. All other faces of the cube are traction free.

The reaction force calculated for each case as a function of the normalized displacement $\frac{d}{\delta_n}$ under quasistatic deformation is shown for all three cases in Figure 3.5. The force is normalized by the maximum force the layer of cohesive elements can sustain $A_0\,\sigma_c$, where $A_0$ is the area of the surfaces in the undeformed configuration and $\sigma_c$ is the cohesive strength. The straight, dashed line has slope $\frac{E\,\delta_n}{\sigma_c\,L}$ and describes the response of the cube under infinitesimal deformations. The figure shows that all three cases display nearly the same response with a peak reaction force determined from the parameters of the cohesive relations although the arrangement of particle with respect to the geometry of the cohesive elements is changing. The deviation of the curves from the extrapolation of the infinitesimal strain response is due to constrain effects from the displacement boundary conditions at finite deformations. The results of these calculations demonstrate that

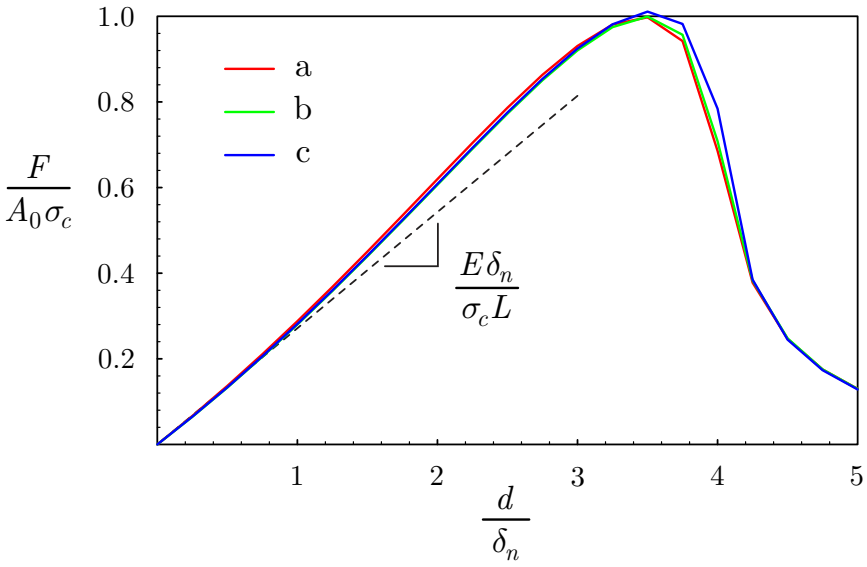


Figure 3.5: Curves of reaction force $F$ versus end displacement $d$ under uniaxial extension for different particle distributions normalized by the cohesive parameters $\sigma_c$ and $\delta_n$ and the modulus $E$ and the model dimensions $L$ and $A_0$.

cohesive surfaces can be inserted at arbitrary locations within a meshfree domain without also introducing additional degrees of freedom.

### 3.3.2 Surface projection of cohesive tractions

With standard finite element shape functions, the field representation along a boundary, or surface, depends only on the nodes lying directly on that boundary. As a result, natural boundary conditions or cohesive tractions produce only surface forces. Here we present an approach for projecting cohesive tractions that also produces forces only at particles lying along the surface. One of the key advantages of meshfree methods is that particles may readily be added to the domain without requiring remeshing. We utilize this feature to line both faces of the fracture surface with particles that we donate as $N_{\mathbf{X}}$ as shown in Figure 3.6. Collecting these particles into sets of facets, we define a parameterization of the surface

$$\mathbf{X}(\boldsymbol{\xi}) = \sum_{A \in N_{\mathbf{X}}} \Phi_A^{\mathrm{FE}}(\boldsymbol{\xi})\ \mathbf{X}_A \tag{3.22}$$

using standard finite element shape functions $\Phi_A^{\mathrm{FE}}$. In (3.22), we do not distinguish between which particles lie on the upper and lower surface because they are coincident in the undeformed configuration. Essentially, we insert particles at the arbitrary points used to define the facet geometry in Section 3.3.1. The opening displacement (2.4) is constructed as described for the consistent projection, though the sets of particles $N^+$ and $N^-$ on opposite surfaces of the crack surface may now include nodes in $N_{\mathbf{X}}$.

With meshfree methods, the projection of cohesive tractions penetrates to particles in the bulk because of the dependence on the meshfree shape functions in $\frac{\partial \boldsymbol{\Delta}}{\partial \mathbf{u}_A}$ given by (2.7) and in $\frac{\partial^2 \mathbf{x}}{\partial \mathbf{u}_A \partial \boldsymbol{\xi}}$ given

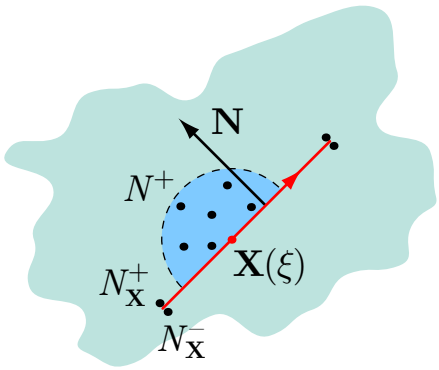


Figure 3.6: Undeformed configuration of a cohesive surface in a meshfree domain with additional points inserted on the upper $N^+_{\mathbf{X}}$ and lower $N^-_{\mathbf{X}}$ surfaces to define the geometry of the surface.

by (3.21) for terms resulting from tracking the local surface transformation $\mathbf{Q}$. Without rigorous justification, we can restrict the projection to the surface nodes through the modifications of

$$\frac{\partial \Delta_i}{\partial u_{jA}} = \begin{cases} \frac{\partial \Phi^{\mathrm{FE}}_A}{\partial \xi} \delta_{ij} & \text{for } A \in N^+_{\mathbf{X}}, \\ -\frac{\partial \Phi^{\mathrm{FE}}_A}{\partial \xi} \delta_{ij} & \text{for } A \in N^-_{\mathbf{X}} \end{cases} \tag{2.7′}$$

and by approximating the mid-plane surface as

$$\mathbf{x}(\boldsymbol{\xi}) = \frac{1}{2} \left( \sum_{A \in N^+_{\mathbf{X}}} \Phi^{\mathrm{FE}}_A(\boldsymbol{\xi}) \, (\mathbf{X}_A + \mathbf{u}_A) + \sum_{A \in N^-_{\mathbf{X}}} \Phi^{\mathrm{FE}}_A(\boldsymbol{\xi}) \, (\mathbf{X}_A + \mathbf{u}_A) \right). \tag{3.23}$$

This expression is approximate because $\mathbf{u}_A$ is only the *contribution* from particle $A$ to the displacement field $\mathbf{u}(\mathbf{X}_A)$ not the displacement of particle $A$ itself. For the cohesive surface formulation, this mid-plane construction is only used to define jacobian of the surface parameterization $\frac{\partial \mathbf{x}}{\partial \boldsymbol{\xi}}$ needed to compute $\mathbf{Q}$. Using (3.23), we can define the consistent approximation to (3.21) as

$$\frac{\partial^2 x_i}{\partial u_{kA} \partial \xi_j} = \frac{\partial \Phi^{\mathrm{FE}}_A}{\partial \xi_j} \delta_{ik}. \tag{3.24}$$

The expressions (2.7′) and (3.24) preserve linear momentum balance across the cohesive surfaces, result in consistent nodal forces and stiffness, and produce forces only at surface particles. Although this approach introduces an additional construction at the surface, it does have the advantage that the crack surfaces become clearly defined with particles.

## 3.4 Adaptive insertion of cohesive surfaces

The procedure for adaptively inserting cohesive surfaces in a meshfree domain is constructed around the moving tip template shown in Figure 3.7. Although the analysis of softening due to a network of cohesive surfaces in Section 2.1.3 or theoretical conditions for the appearance of discontinuous bifurcations[40, 88] may suggest an adaptive approach is needed for modeling cohesive fracture,

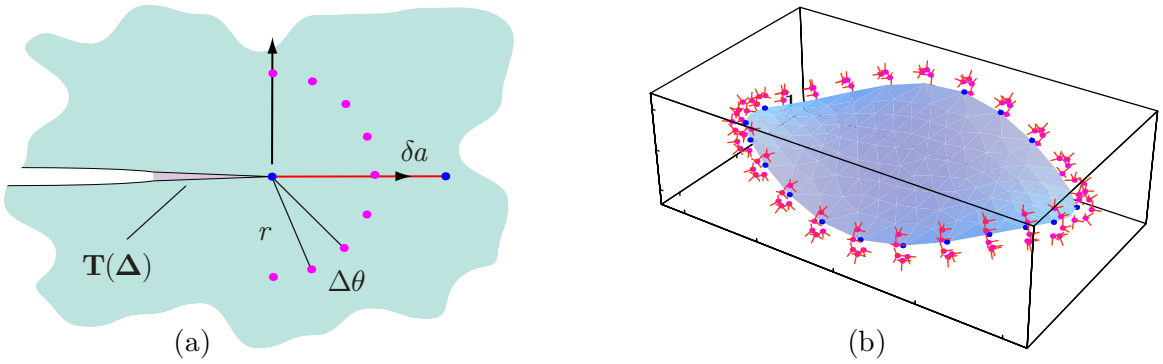


Figure 3.7: (a) Moving tip template used for adaptive insertion of cohesive surfaces illustrating the crack extension increment $\delta a$, the sampling radius $r$, and the angular sampling increment $\Delta\theta$ and (b) application of the template along three-dimensional crack fronts.

the implementation of a simulation procedure introduces a number of parameters not prescribed by theory. The parameters we introduce in our moving tip model are shown in Figure 3.7 (a). An insertion criterion is sampled at points a distance $r$ from the tip at an angular interval of $\Delta\theta$. With meshfree methods, all points in the domain may equivalently be selected for evaluation of the displacement field and its derivatives. For the hyperelastic bulk materials considered in this study, we can readily sample the traction on prospective fracture planes or the hoop stress $\sigma_{\theta\theta}$. With the bulk behavior predicted by the VIB model, we can probe the material for the appearance of discontinuous bifurcation using the acoustical tensor (A.31).

Once the insertion criterion is satisfied, we insert an additional segment of fracture surface of length $\delta a$. The traction across the fracture plane is used to initialize the cohesive relation $\mathbf{T}(\boldsymbol{\Delta})$ (2.46) in order to keep the traction in time. Additionally, the shape functions of any nodes affected by the additional fracture surface are recalculated. The sampling template is then reconstructed at the new position of the crack front. As shown in Figure 3.7 (b), the template can be applied in three dimensions by transforming the tip parameters into the local coordinates along the crack front. In three dimensions, the moving crack front "paves" the fracture surface with triangular or quadrilateral facets. Krysl and Belytschko[51] discuss a number if issues associated with implementation of fracture surface generation in three dimensions.

Though detailed numerical examples appear in Section 4, we present two qualitative demonstrations of the adaptive insertion procedure. In Figure 3.8 (a), a beam composed of isotropic, hyperelastic material is subject to quasistatic, displacement-controlled, three-point bending. The figure shows the predicted fracture path for three separate cases in which the location of the initial pre-crack is changed. A critical, maximum hoop stress criterion determines the insertion of additional fracture surfaces. The results demonstrate how cracks can grow in arbitrary orientations with respect to the arrangement of nodes which are positioned at the vertices of the grid shown. Figure 3.8 (b) presents a three-dimensional example of adaptive crack surface insertion. A cylindrical body (only one quarter shown) is composed of an inner core and a surrounding encapsulant. The core undergoes a quasistatic volumetric expansion with respect to the encapsulant. The core and part of the encapsulant are modeled using finite elements. A region modeled using RKPM is coupled to the elements with the method proposed by Belytschko *et al.* [12] As the core expands,

the initial pre-crack in the meshfree domain grows into the arbitrary shape shown in the figure.

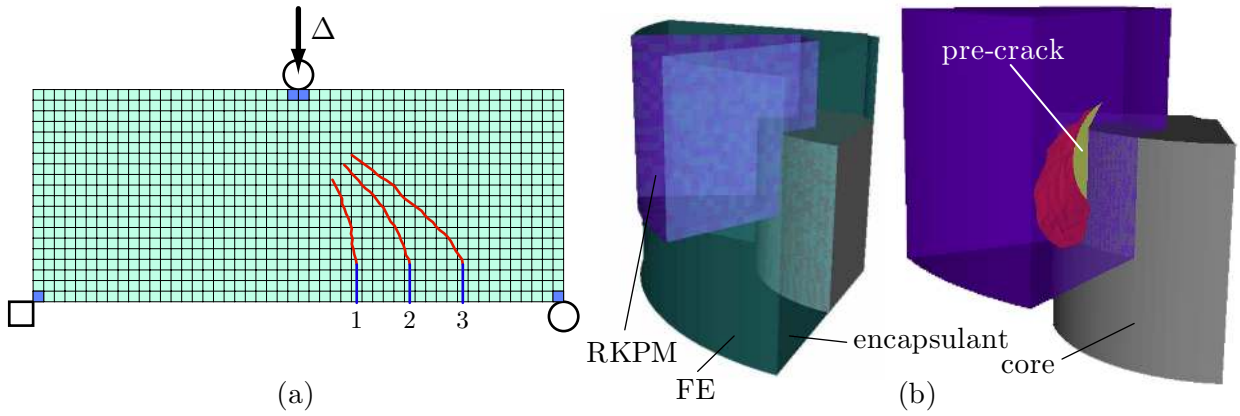


Figure 3.8: Qualitative examples of adaptive insertion showing (a) fracture in an asymmetric, three-point bending specimen and (b) growth of a crack in a quarter symmetry model subject to a dilatational mismatch strain.

In principle, the cohesive tractions should remove the stress singularity at the crack tip. This regularization should eliminate problems of convergence associated with point-wise sampling of the crack tip fields. Because the role of insertion procedure is to provide a smooth and continuous transition between the bulk response and the cohesive surface relations, the fracture behavior should be independent of sampling parameters introduced in the implementation. The effect of these sampling parameters is investigated in the simulations presented in Section 4.4.

# 4 Numerical examples

We present a number of simulations to demonstrate capabilities and shortcomings of the cohesive modeling approaches. The first two examples focus on interfacial failure for which the fracture path is known *a priori* or restricted to pre-defined surfaces. Under these circumstances, we focus on verifying that the modeling approach and numerical procedures display the expected resistance to crack extension. In the third example, we compare how reliably the different methods can predict fracture paths under dynamic loading conditions. The final example focuses in reproducing the behavior of cracks propagating under unstable loading conditions. Under these conditions, the intrinsic, rate-limiting physics of crack growth emerge.

## 4.1 Validation of cohesive zone modeling using a double-cantilever beam

Before comparing with experimental results, one should conduct numerical studies on simple geometries to understand potential sources of error. The double-cantilever beam geometry (DCB) is a likely candidate because the geometry is accepted by the fracture community and an analytical solution exists. A schematic of the DCB geometry is illustrated in Figure 4.1. For the DCB geom-

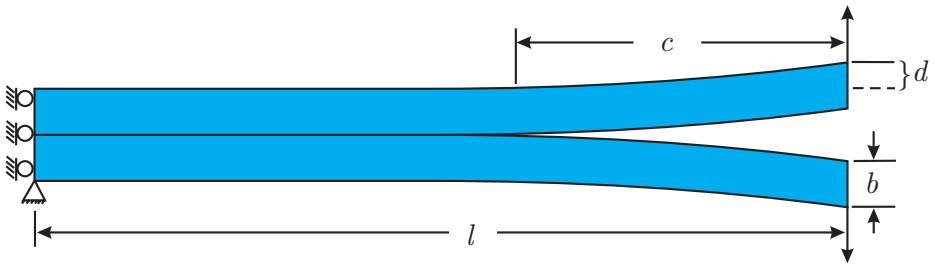


Figure 4.1: Schematic of the DCB geometry showing the overall beam length $l$, the free length $c$, the beam height $b$, and the end displacement of the midline $d$.

etry, we are seeking to minimize error in modeling: (i) bulk response, (ii) cohesive zone response, and (iii) interaction between (i) and (ii). In hope of decoupling the bulk and cohesive response, the bulk behavior is assumed to be linear elastic. Consequently, all dissipation is lumped into surface energy. This assumption can be illustrated by expressing the increment in the total energy under displacement-controlled loading as

$$\delta U = \delta U_E + \delta U_S \tag{4.1}$$

where $\delta U_E$ is the increment in strain energy and $\delta U_S$ is the increment in surface energy. The strain energy increment for both beams is

$$\delta U_E = \frac{3Ed^2b^3}{4c^3}\,\delta d, \tag{4.2}$$

where $E$ is Young's modulus. The interfacial surface energy changes as

$$\delta U_S = 2\gamma\,\delta c. \tag{4.3}$$

Invoking the Griffith energy balance at constant end displacement,

$$\left.\frac{\partial U}{\partial c}\right|_d = 0 \tag{4.4}$$

we can write an expression for the energy release rate

$$G = \frac{3Ed^2b^3}{4c^4} = 2\gamma \tag{4.5}$$

and solve for the crack length

$$c = \sqrt[4]{\frac{3Ed^2b^3}{4G}}. \tag{4.6}$$

One should note that the analytical solution does not take into account a cohesive zone. In fact, the crack length $c$ is simply the free span of the beam. The beam modulus for all simulations is 69.0 GPa (aluminum).

Crack growth is governed by the model proposed by Xu and Needleman[95]. Section 2.1.2 outlines the model in detail. In the context of the Xu-Needleman model, $\phi_n$ represents the normal work of separation, $\sigma_{\max}$ corresponds to the cohesive strength, and $\delta_n$ signifies the characteristic length scale associated with normal separation. Referencing (4.5), one can equate $\phi_n$ to $G_I$. For this study, $\phi_n$ is assumed to be 52.5 J/m$^2$ and $\delta_n$ is taken to be 25.4 $\mu$m. These values correspond to a weakly bonded interface. The resulting cohesive strength is only 0.761 MPa.

### 4.1.1 Understanding sources of numerical error

In hopes of capturing both the bulk response and cohesive zone response, four DCB meshes are used in the analysis. Figure 4.2 illustrates meshes A through D in the undeformed state. The number

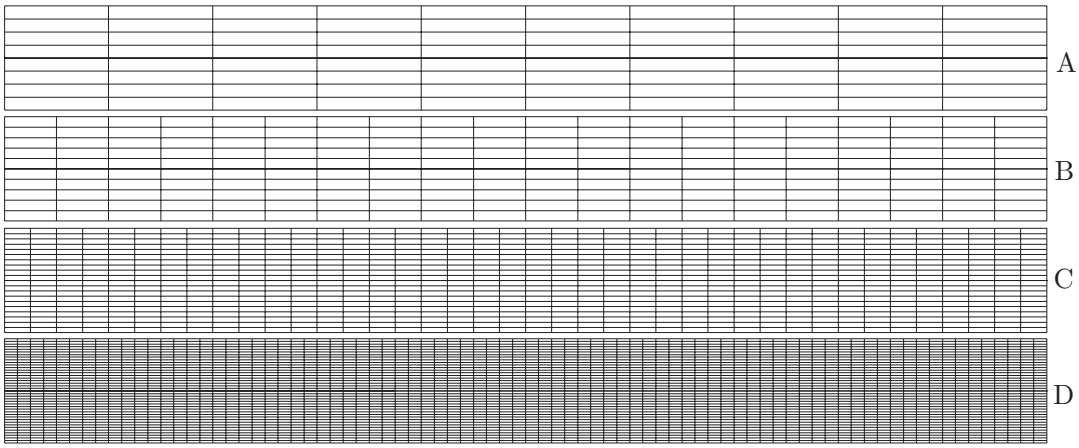


Figure 4.2: Four meshes used for the DCB peel simulations from the coarsest A to the most refined D.

of elements varies both through the thickness, $d$, and along the length, $l$. One should note that four-noded quadrilateral elements are employed for all simulations. Mesh A is composed of only 4 elements through the thickness and 10 elements along the length while mesh D is composed of 20

elements through the thickness and 80 elements along the length. The total number of elements for meshes A, B, C, and D are 90, 220, 840, and 3492, respectively. A layer of cohesive zone elements joins the two beams and provides a path for mode I crack propagation.

All quasistatic simulations are performed in plane stress. As indicated in Figure 4.1, symmetry is applied on the left face and a monotonically increasing end displacement $d$ is enforced on the upper and lower surfaces of the beams. Because the meshes are not pre-cracked, a cohesive zone forms at the edge and propagates inward. Figure 4.3 attempts to illustrate both the bending stresses and cohesive tractions. Red corresponds to regions of tension and adhesion while blue corresponds to regions of compression and de-adhesion. Notice that the cohesive zone spans multiple elements.

Given a cohesive zone, one must choose a criterion for tracking the crack tip. We define the crack

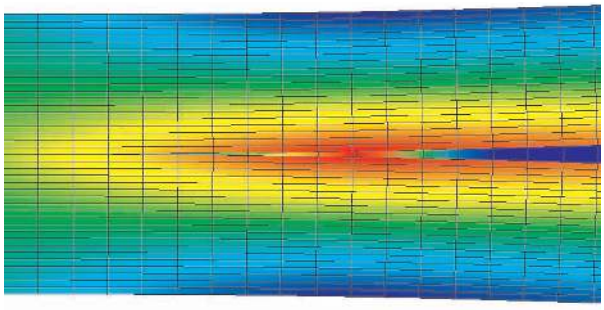

Figure 4.3: Contour plot of bending stresses and cohesive tractions.

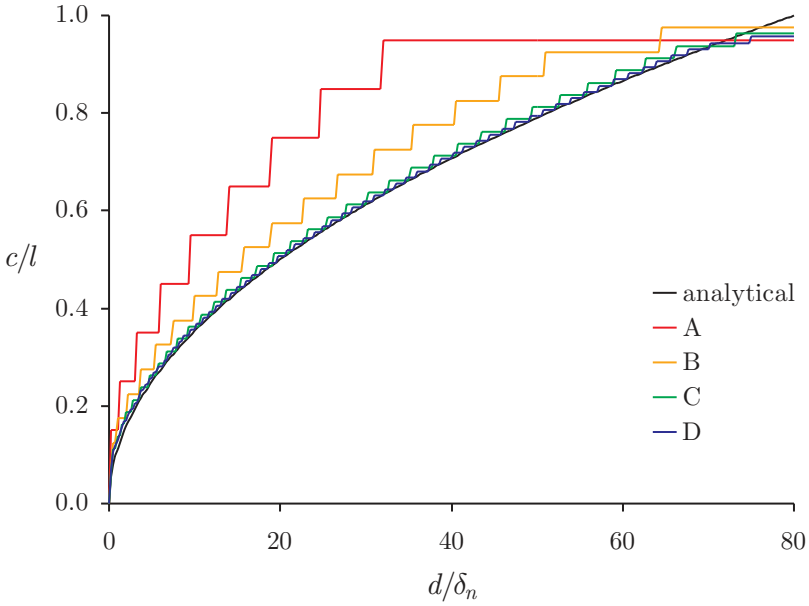


Figure 4.4: Crack length $c$ in a DCB specimen for four levels of mesh refinement A through D compared with the analytical solution.

tip in terms of crack tip opening displacement (CTOD). The crack tip is defined to coincide with

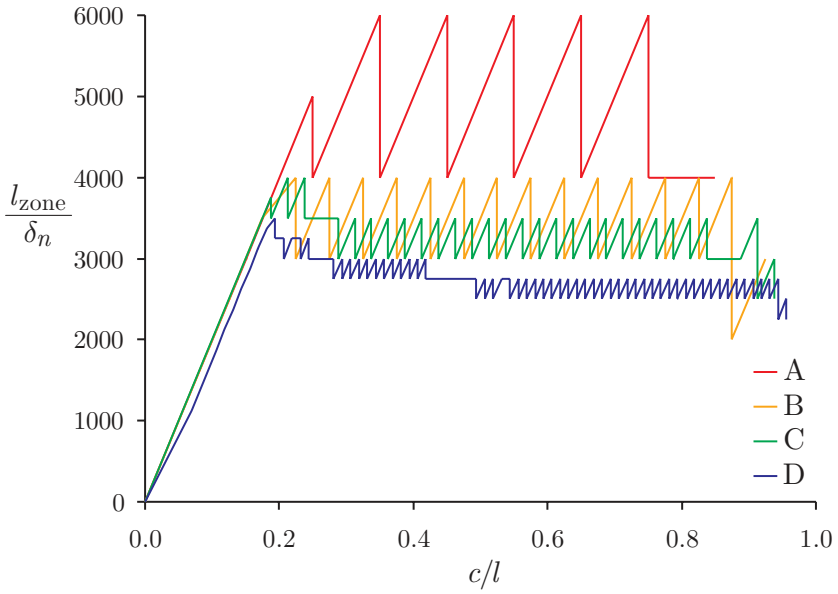


Figure 4.5: Variation in cohesive zone size $l_{\text{zone}}$ as a function of the crack length $c$ for four levels of mesh refinement A through D.

$0.1\delta_n$. Therefore, the cohesive zone lies in the wake of the selected crack tip. Given this criterion, we can plot simulated crack growth. Non-dimensionalized crack growth curves are presented for all meshes in Figure 4.4. Meshes C and D match the analytical solution. Surprisingly, this agreement remains strong even for small crack lengths. More importantly, meshes A and B do not agree with the analytical solution. Coarser meshes yield accelerated crack growth. We can examine the size of the cohesive zone in each simulation to gain insight. Again, we must establish a criterion for the tail of the cohesive zone. We define the cohesive zone to span from $0.1\delta_n$ to $4.0\delta_n$. If we integrate the traction-separation law detailed in Section 2.1.2, we find that 90% of the energy is dissipated between $0.1\delta_n$ and $4.0\delta_n$. Figure 4.5 illustrates the cohesive zone size for each mesh. Although the sampling size is limited to defined CTOD at nodal coordinates, one can clearly see the zone size is much smaller for the finer, converged meshes. We know that the cohesive zone size is dependent on the boundary-value-problem. If we increase the elastic modulus of the beams, we would expect the cohesive zone to lengthen. Conversely, if we decrease the elastic modulus of the beams, the cohesive zone would shrink. From this simple physical observation, we are inclined to conclude that the numerical stiffness associated with coarser meshes not only accelerates crack growth, but also lengthens the cohesive zone. This numerical stiffness can be further explored by monitoring the reaction force and calculating the energy release rate.

### 4.1.2 Exploring $G$, the energy release rate

By monitoring the reaction force $P$ at the applied displacement, we can determine the resistance at a particular crack length common to all simulations. In addition, we can also use that reaction load to calculate a more useful quantity, the mechanical energy release rate. From beam theory,

we can relate $d$ to $P$ using

$$d = \frac{4Pc^3}{Eb^3} \tag{4.7}$$

and substitute (4.7) into (4.5) to obtain

$$G = \frac{12P^2c^2}{E}. \tag{4.8}$$

Note that the energy release rate varies with the reaction load. Figure 4.6 makes a powerful statement about the variation in the driving force for all simulations. The energy release rate for the converged meshes mirrors the input work of separation, $G = \phi_n$. However, the energy release rate for the coarser meshes is much greater. While the upper and lower bounds are influenced by nodal sampling, we can safely conclude that errors in the energy release rate for Mesh A and B are 300% and 50%, respectively.

### 4.1.3 Calculating the $J$-integral

While the prior section focused on mesh-related stiffness, we also need to validate the numerical integration of the cohesive zone. Because the beams are elastic, $J = G$. If we examine the finest mesh, D, we would expect to calculate the $J$-integral with little error. Given a cohesive zone, the $J$-integral, given by (2.102), simplifies to

$$J = \int_\Gamma T_y \frac{\partial u_y}{\partial x} ds \tag{4.9}$$

where $T_y$ represents the global traction distribution and $u_y$ defines the global displacement distribution along the cohesive zone. Figure 4.7 concisely illustrates the components of the integrand of $J$. All quantities are expressed over the length of the cohesive zone. Using this information, we can integrate (4.9) and obtain 52.5 J/m$^2$, $\phi_n$.

In addition to validating the $J$-integral for mesh D, we would like to quantify the number of elements needed for integration purposes. Numerical evaluation of the $J$-integral is performed with the same 1- and 2-point Gauss rules used to evaluate the weak form contributions of the cohesive elements in the finite element code. These evaluations are performed with uniform grid sizes $h$. The value of $J$ depends on the relative alignment of the traction distribution and the integration grid. Varying this alignment produces a bound on the error in evaluating $J$. This bound is shown in Figure 4.8 as a function of $h$ normalized by the cohesive zone size $l_{\text{zone}}$. For example, if 5 elements are in the zone, $h/l_{\text{zone}} = 0.20$. Based on Figure 4.8, one would expect to evaluate the $J$-integral accurately. In fact, with a 2-point Gauss rule and 2 elements in the zone, we only expect 10% error. We should note that in practice the error would be larger because the crack opening displacement, $u_y$ is restricted by displacement interpolation functions. The current displacement profile is taken from mesh D with over 11 elements in the zone.

### 4.1.4 Ramifications of zone size

The prior section validates mesh D, with $h/l_{\text{zone}} < 0.10$. $J$-integral analysis concludes that fewer elements would be required to resolve the global traction distribution. To confirm prior findings, we propose to: (i) fix the mesh size, (ii) fix $\phi_n$, and (iii) decrement the characteristic length scale,

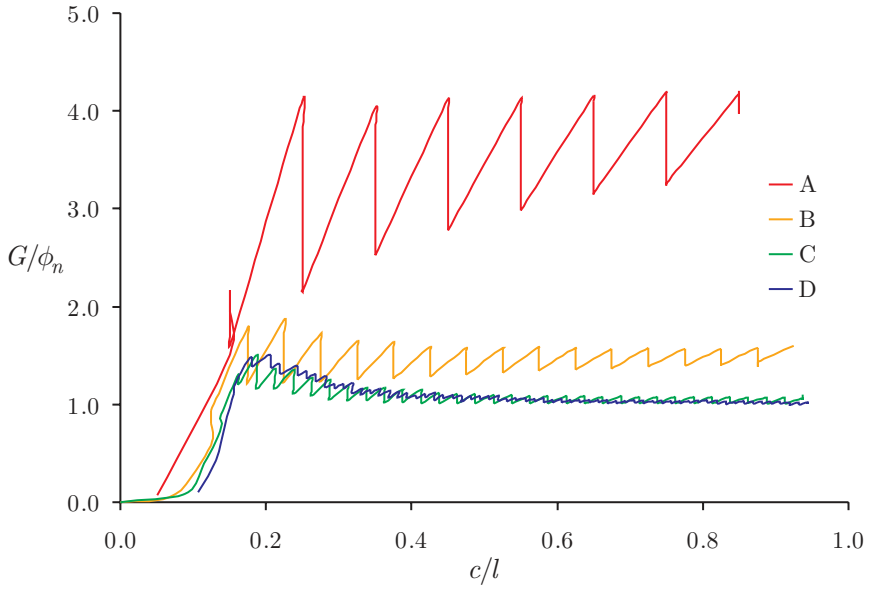


Figure 4.6: Variation in the crack driving force $G$ as a function of crack length $c$ for four levels of mesh refinement $A$ through $D$.

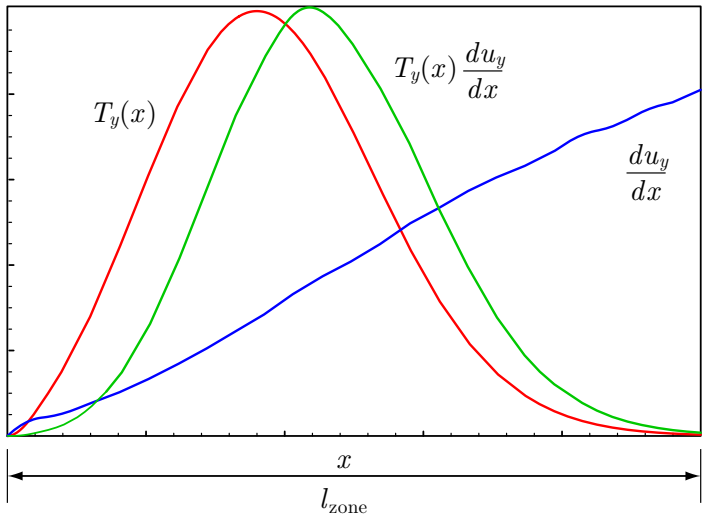


Figure 4.7: Characteristic scale over which the tractions in the cohesive zone contribute to the $J$-integral.

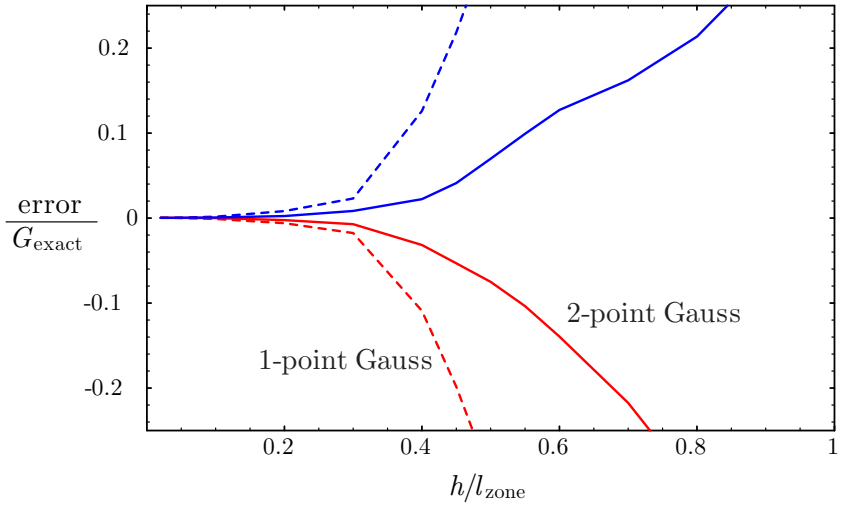


Figure 4.8: Bounds on the error in numerical integration of the $J$-integral as a function of mesh size $h$ using 1- or 2-point Gauss integration.

$\delta_n$. The characteristic length scale is reduced by a factor of 2, 5, and 10. The resulting traction-displacement curves are illustrated in Figure 4.9. Because $\sigma_{\max} = \phi_n/e\delta_n$, the cohesive strength increases by a factor of 2, 5, and 10. Crack growth curves for the confirmation simulations are shown in Figure 4.10.

As one would expect, the cohesive zone size scales with $\delta_n$. The number of elements in the zone for simulations $1.0\delta_n$, $0.5\delta_n$, $0.2\delta_n$, and $0.1\delta_n$ is 11, 8, 4, and 3, respectively. From these findings, we can conclude that we will match the analytical solution if we: (i) employ a converged mesh, and (ii) keep 3 or more elements in the cohesive zone. An equally powerful conclusion is that if (i) and (ii) are satisfied for an elastic body, $\phi_n$ dominates crack growth.

Because we do not sample the cohesive zone size during the simulation, the burden is on the analyst to provide ample discretization a priori. The authors wonder what numerical "symptoms" small and even sub-element cohesive zones would exhibit. With this in mind, $\delta_n$ is further decremented by a factor of 20, 50, and 100. Because quasistatic implicit methods do not converge, we employ explicit dynamics time integration to complete the simulations. The applied displacement rates approximate the quasistatic solution (400,000 time steps). Figure 4.11 illustrates that both error and global instabilites that can result from insufficient discretization. Although the size of the cohesive zone is difficult to track, one can safely say that for $0.1\delta_n$ the zone is 2 to 3 elements, for $0.05\delta_n$ it is 1 to 2 elements, for $0.02\delta_n$ it is on the order of an element, and with $0.01\delta_n$ it is sub-element. While the crack tip oscillates in the initial stages of growth for $0.02\delta_n$, the case of $0.01\delta_n$ exhibits oscillations throughout the simulation. We must stress that poor resolution will yield numerical instabilites that should not be interpreted as physical instabilities.

The simulations presented for the DCB geometry attempt to delineate errors associated with numerical stiffness and zone resolution. Stiff, coarser meshes accelerate crack growth due to artificially higher energy release rates. If the cohesive zone is not properly resolved, error and global instabilites will result. However, if one is able to deliver (i) a converged mesh, (ii) 3 or more elements in the zone, and (iii) an accurate work of separation, one can expect to predict crack growth reliably.

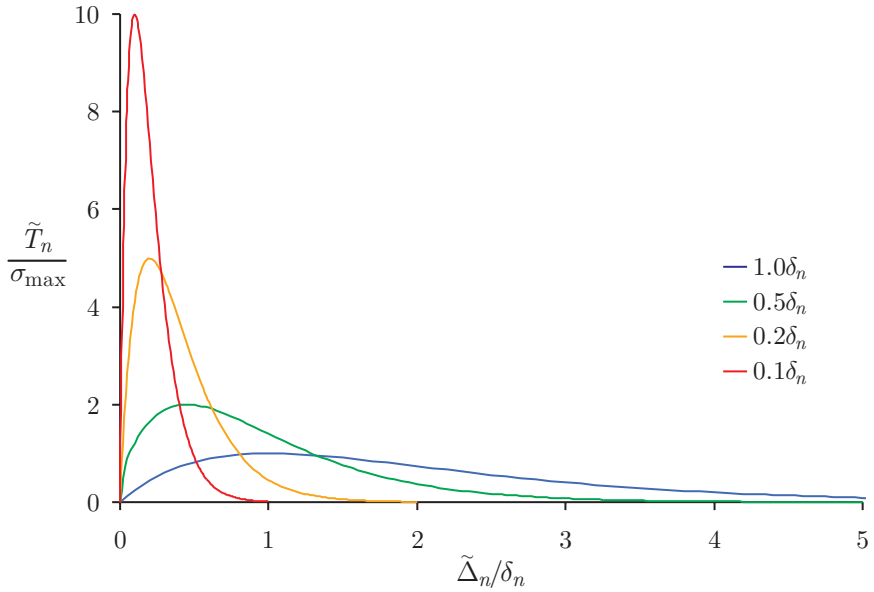


Figure 4.9: Reduction in the characteristic length scale, $\delta_n$

## 4.2 Three-dimensional validation of crack curvature in muscovite mica

Although Section 4.1 explored possible pitfalls in employing cohesive zone models, comparison with experimental observations is clearly needed. To simplify matters, the authors have chosen to investigate muscovite mica, a mineral that cleaves along known, crystallographic planes. The goal of the effort is not only to predict crack growth, but also to predict the three-dimensional curvature of the crack front.

### 4.2.1 Experimental Findings

Muscovite mica, an alumina silicate, is widely used in brittle fracture and interface studies (Obreimoff[66], Bryant[14], Bailey[5], Wan[91, 92]). Mica is composed of silica tetrahedra that are strongly bonded in layers to aluminum cations. A layer of potassium ions weakly bonds silica-aluminum-silica layers together. Because of its layered crystal structure, mica cleaves along the weak plane of potassium bonds illustrated in Figure 4.12. Its cleavage properties and optical transparency make mica an ideal brittle material for fracture studies.

In 1930, Obreimoff[66] validated the Griffith fracture criterion for brittle materials in a constant displacement double-cantilever beam (DCB) experiment. Recently, Hill[39] investigated the muscovite mica system. Some of her initial studies focused on crack growth and documenting crack front curvature near the free surface. Displacement boundary conditions were applied via a narrow wedge. Unlike a constant load or constant moment DCB test, the wedge enforces a constant displacement and yields a constant, stable crack length. The mechanical energy release rate $G$ is only a function of the wedge height, beam geometry, modulus, and crack length.

In Hill's work, a crack is initiated in the specimen using a 267 $\mu$m thick blade. The specimens are significantly thinner than the blade; thus, cleaving the mica into two, symmetric beams is difficult.

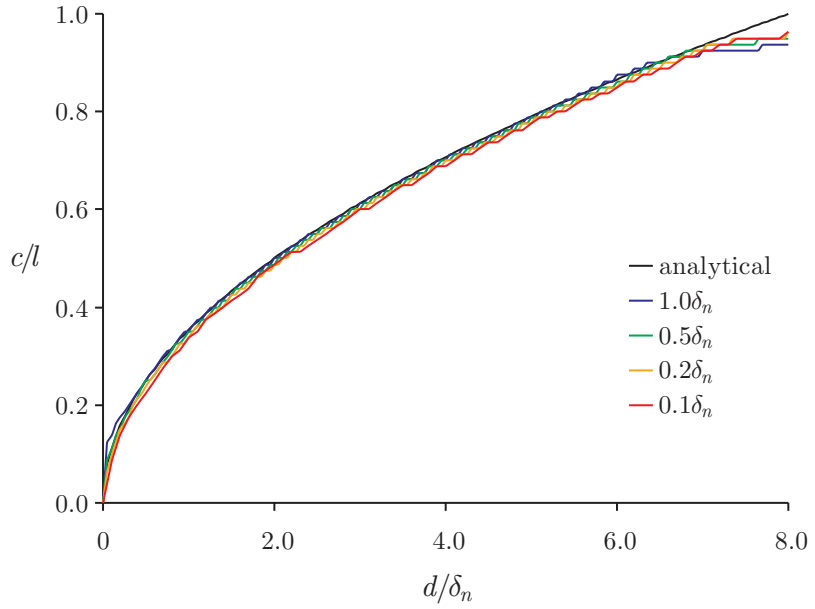


Figure 4.10: Simulated crack growth for different critical opening displacements $\delta_n$ within the limits of mesh resolution.

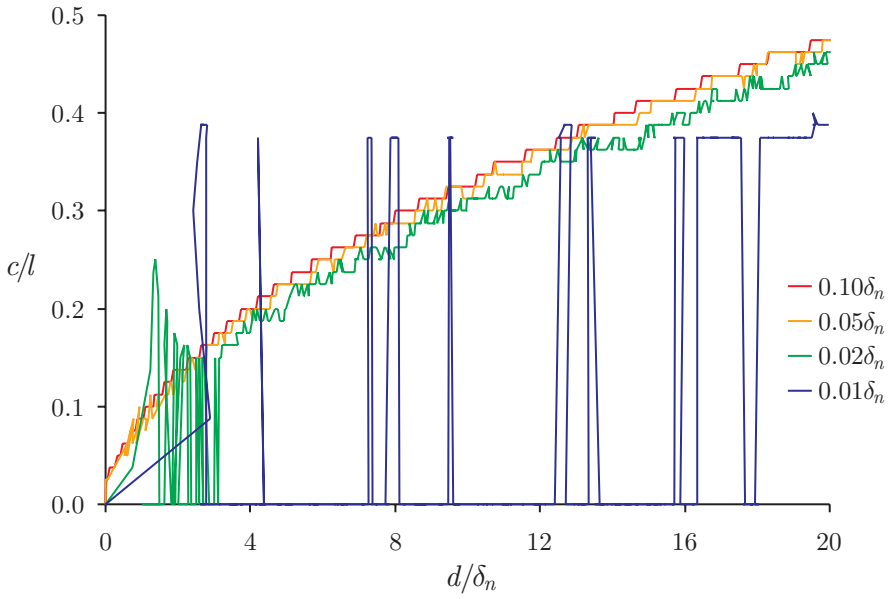


Figure 4.11: Instabilities in the simulated crack growth for different critical opening displacements $\delta_n$ below the limits of mesh resolution.

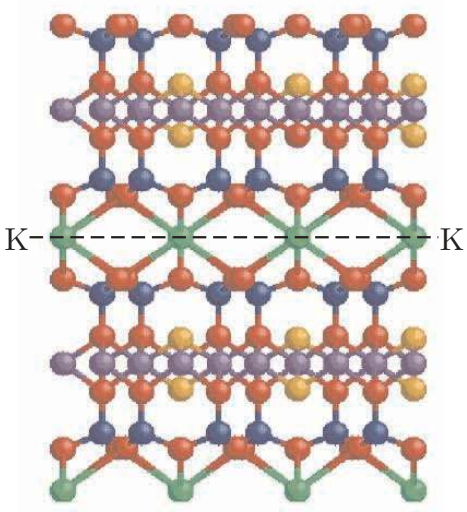


Figure 4.12: Layered crystal structure of muscovite mica, showing the layer of weakly bonded potassium (K) ions.

The cleaved mica is placed into a specimen holder and a stepper motor pushes the mica specimen onto the blade in 1 $\mu$m increments. Crack propagation is viewed with an optical microscope using green light. Figure 4.13 clearly illustrates that the free surface causes crack tip curvature. The region of curvature is roughly 760 $\mu$m from the edge of the specimen. In this particular experiment, the height of the upper and lower beams is 81 $\mu$m and 133 $\mu$m, respectively. For a more complete description of the test procedure, please reference Hill[39].

### 4.2.2 Problem statement

Because experimental evidence indicates a preferential cleavage plane, one can easily separate the bulk and interface models. The bulk is modeled as isotropic, linear elastic. The elastic modulus of muscovite mica, 169 GPa, is taken from McNeil[64]. The Poisson's ratio is assumed to be 1/4. The interface model employed in this work was proposed by Xu and Needleman[95] and is described in Section 2.1.2. Given that the bulk is elastic, the critical energy release rate in mode I, $G_{Ic}$, can be equated to the work of normal separation, $\phi_n$. While $\phi_n$ is an input parameter taken from experiment, 0.82 J/m$^2$, the characteristic length scales of separation, $\delta_n$ and $\delta_t$, are assumed to be 100 nm for both normal and tangential separation.

Because the beams have different heights, the neutral axis does not coincide with the fracture plane. Thus, the crack propagates under mixed-mode conditions. Since detailed measurements of the cohesive behavior have not been performed, we assume that $q = 1$ and $r = 0$. Future studies should consider if $G_{Ic}$ is truly equal to $G_{IIc}$.

As noted in the Section 4.2.1, the mica is pushed onto the wedge in 1 $\mu$m increments. Because mica is perfectly brittle, the crack length ahead of the wedge remains constant. This condition produces a "steady-state" crack length of roughly 7 mm. In order to reflect the experiment, the beam length is 10 mm. A beam width of 2.1 mm is selected to span the experimental micrograph, Figure 4.13. Figure 4.14 illustrates the aspect ratio of the specimen. While the boundary conditions reflect the experiment, no attempt is made to enforce the wedge geometry. Rather, an end

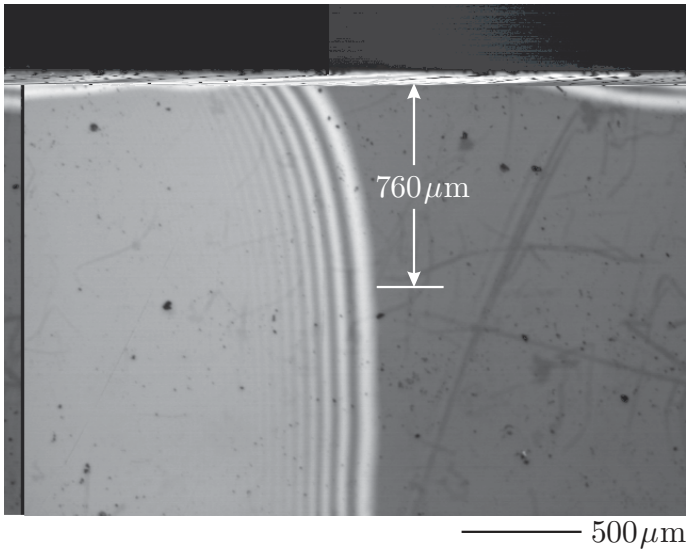


Figure 4.13: Crack front curvature in muscovite mica, showing the curvature in the front at the edge of the sample

displacement is applied to the central surface of each beam. The far end of the beam is pinned at the lower corner. Symmetry is applied along the beam width. Although the detailed shape of the blade edge is important during initiation, our effort focuses on crack curvature during "steady state" propagation.

Element spacing along the length is driven by the size of the cohesive zone. Defining the zone to span from $0.1\delta_n$ to $4.0\delta_n$, the simulations yield a cohesive zone of $200\,\mu$m. An element size of $25\,\mu$m guarantees 8 elements in the zone for integration purposes. Because eight-noded hexahedral elements are employed in bending, 10 elements span the thickness. Finally, spacing along the beam width is driven by the curvature shown in Figure 4.13. In order to place at least 10 elements within the region of curvature, the elements are $75\,\mu$m wide. The deformed mesh is illustrated in Figure 4.15. These constraints result in a mesh with 255,838 nodes and 235,200 elements.

### 4.2.3 Results and discussion

The high level of discretization requires that all simulations be performed in parallel using explicit dynamics time integration with loading rates selected to minimize inertial effects. Two-dimensional simulations verify that the imposed velocities approximate the quasistatic solution. Two-dimensional simulations also verify that the crack length is only governed by the work of separation. The size of the zone, however, is determined by both the work of separation and the characteristic length scales associated with separation, $\delta_n$ and $\delta_t$. Keeping $\phi_n$ and $\phi_t$ constant and varying $\delta_n$ and $\delta_t$, one can obtain numerous zone sizes with nearly identical crack lengths. Please reference Section 4.1 for more discussion.

We ran the model detailed in Section 5.2.2 in parallel for 200,000 time steps. The computed displacement field can be manipulated to generate a fringe pattern. The intensity of reflected light

Figure 4.14: Mesh decomposed for 64 processors.

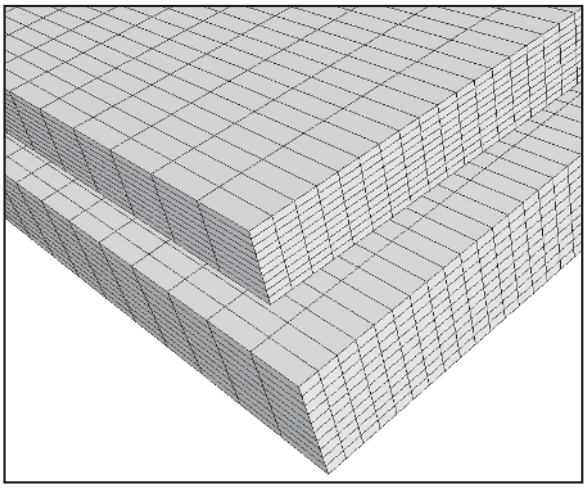

Figure 4.15: Detailed view of the DCB mesh.

varies as a function of the crack opening displacement $\Delta$ as

$$I \propto \sin^2\left(\frac{2\pi\Delta}{\lambda}\right) \tag{4.10}$$

where $\lambda$ is the wavelength of green light, 550 nm. Figure 4.16 illustrates the fringes associated with the crack front. Scale markers are placed for comparison to the experimental micrograph, Figure 4.13. Notice that in both cases, the crack curves over approximately 760 $\mu$m. This curvature can be attributed to a corresponding variation in the local energy release rate.

The first few fringes in both the simulation and experiment are indicative of the crack tip opening displacement profile. Although the experimentally observed crack front is "smeared" by a simulated cohesive zone size of 200 $\mu$m, the agreement in the fringe spacing indicates the variation in the opening profile is being reproduced fairly well. In the experimentally observed fringe patterns, the contrast fades after approximately five fringes. This may be due to the close spacing of fringes or an insufficient coherence length in the light source. As the distance between fringes approaches the mesh size, spurious fringes appear in the simulated patterns due to aliasing. A smaller zone size

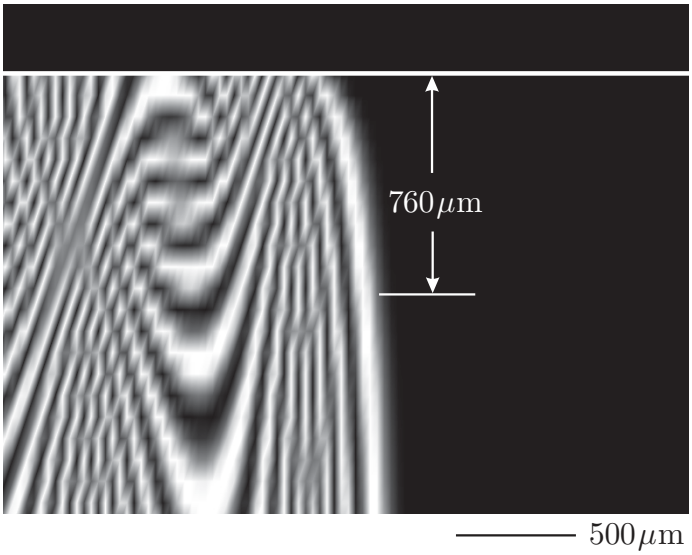


Figure 4.16: Simulated fringe pattern in muscovite mica resulting from the variation in the crack opening displacement.

would clarify the crack front curvature. Smaller zone sizes can be obtained through a reduction in $\delta_n$ and $\delta_t$. However, as noted in Section 4.2.2, the mesh size will change accordingly. In addition, more elements through the width will also be required to clarify crack front curvature. The needed discretization will require models on the order of several million degrees of freedom.

A cohesive approach to fracture is validated through comparison to crack front curvature in the muscovite mica mineral system. Experimental results clearly illustrate the region and nature of crack front curvature. Because mica cleaves along pre-determined planes, mixed-mode fracture is successfully modeled through a layer of cohesive zone elements. Three-dimensional finite element simulations yield a curved crack front that compares favorably with experimental findings. More work is needed. Future simulations should explore a reduction in the cohesive zone size and its effect on the crack tip opening displacement profile and crack front curvature.

## 4.3 Simulations of mixed-mode, dynamic crack propagation

The physics governing the propagation of cracks subject to mixed-mode loading are not well understood. Within the context of linear elastic fracture mechanics, it is often assumed that cracks extend in the direction of the local mode I loading. Similarly, tensile failure leading to crack propagation is assumed to occur along the direction perpendicular to the maximum hoop stress around the crack tip or in the direction perpendicular to the maximum principal stretch. Other criteria proposed for determining the fracture path include the maximum strain energy and the minimum strain energy. All of these criteria are strictly phenomenological. The goal of cohesive modeling approaches is to embed the essential physics of the fracture process in the constitutive behavior thereby allowing fracture to occur as the physics dictates.

The simulations in this section compare the ability of two cohesive modeling approaches to predict the direction of crack propagation reliably under mixed-mode loading conditions. First, we study the convergence and mesh sensitivity displayed by the cohesive surface network approach. The key advantage for this method is that fracture occurs without requiring that we track any failure initiation conditions or that we change the mesh to allow cracks to propagate. All element interfaces are bound together by cohesive tractions, and fracture occurs when the local loading overcomes the cohesive tractions. Seeding all element boundaries with cohesive surfaces is intended to provide a rich selection of fracture paths for growing cracks. Unfortunately, this seeding leads to fictitious compliance of the finite element mesh. As described in Section 2.1.3, the softening becomes less pronounced as the cohesive strength increases. Increasing the cohesive strength has the additional effect of reducing the size of the fracture process zone. Mesh resolution of the cohesive tractions limits how small the process zone can be. With these simulations, we attempt to find a compromise between these conflicting requirements.

The Virtual Internal Bond (VIB) model, described in Section 2.2, also allows fracture to develop without requiring that we track a failure initiation condition or change the model geometry. Unfortunately, the lack of an intrinsic length scale in the model dictates a particular mesh size for a given fracture energy. This shortcoming of the model implies that mesh size convergence studies cannot be performed with the model in its present form. As described in Section 2.2.4, the lack of an intrinsic length scale not only dictates the mesh size, but also leads to an anisotropy in the fracture energy as a function of propagation direction. This anisotropy in the fracture energy is not as severe as that produced by the cohesive surface network approach, where the limited number of propagation directions provided by the mesh imply infinite fracture energies for growth in all other orientations. We use the VIB model with meshfree methods in order to reduce the tendency for cracks to propagate along mesh lines. With meshfree methods, the nodal support size replaces the mesh dimension as the fictitious length scale selected by the localized mode.

Unfortunately, the current implementation of adaptively inserted cohesive surfaces in a meshfree domain is not sufficiently developed to handle the dynamic propagation conditions produced in these simulations. The adaptive approach would have allowed us to study which of the failure initiation conditions mentioned above produce the most physically realistic fracture paths. Additionally, the adaptive approach could be used with the VIB model which provides a failure initiation condition derived from the acoustical tensor, as described in Section 2.2.5.

### 4.3.1 The Kalthoff-Winkler experiments

In the experiments of Kalthoff and Winkler[43], specimens of maraging steel type 18Ni900 are subject to impact loading and, under a range of impact velocities, fail in brittle mode through the propagation of a crack branching at approximately 70° to the pre-cracks. The focus of the experimental study is to characterize the transition from failure due to brittle fracture to failure by the propagation of an adiabatic shear band. In this study, we only attempt to reproduce the results of the brittle failure mode. The specimen geometry used in the experiments is shown in Figure 4.17.

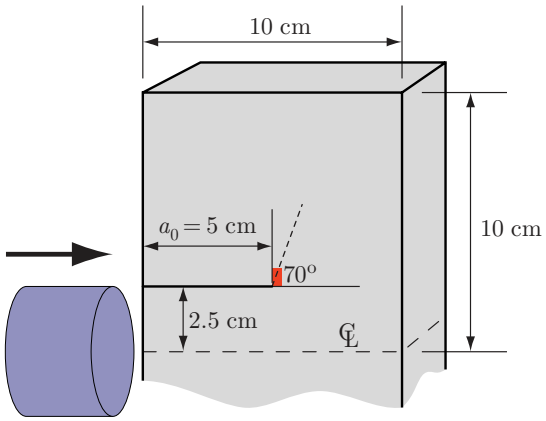


Figure 4.17: Geometry of the Kalthoff-Winkler[43] experiments (only upper-half shown).

Belytschko and Tabbara[13] model these experiments using concepts from linear elastic fracture mechanics with adaptive propagation of crack surfaces in a meshfree setting. In their simulations, extension is assumed to occur perpendicular to the direction of the maximum hoop stress around the crack tip. The hoop stress is calculated using asymptotic solutions for a crack propagating at a constant velocity. The crack velocity is assumed to be $0.15\,c_s$, where $c_s$ is the shear wave speed. Crack branching is not considered. These assumptions have a significant effect on the outcome of these simulations because the crack behavior is strongly influenced by the arrival of elastic wave reflections from the specimen boundaries. The promise of cohesive modeling is that aspects of the crack tip behavior such as the propagation speed and direction become outputs from rather than inputs to the simulations. The loading configuration at the tip of the pre-cracks in this test is particularly challenging to model because it produces severe shearing. Unlike a mode I configuration, no clear fracture path is provided by the symmetry of the loading. Furthermore, response of the cohesive surface network under compression and shear have a strong effect on the results due to the mixed-mode nature of the loading.

### 4.3.2 Problem statement

We investigate the capabilities of cohesive approaches to model these experiments with three sets of calculations. In the first set, we study the effect of the mesh design on the fracture path predicted using the cohesive surface network approach. The assumption of the network approach is that given

a sufficient number of fracture paths to sample, a crack will on average find the same path through different meshes. In the second set of calculations, we investigate the effects of varying the process zone dimension with respect to the element size. In other words, the first set of simulations study convergence of the fracture path as a function of the mesh design while the second set effectively study convergence as a function of mesh size. The final calculations assess sensitivity of the VIB model used in conjunction with meshfree methods to the texture of the particle distribution.

For the bulk, we use a finite deformation, isotropic constitutive model proposed by Simo *et al.* [84] for which the response to volumetric and deviatoric deformations is uncoupled. The hyperelastic stress response is derived from the stored energy function

$$\Phi = U(J) + \bar{\Phi}\big(\bar{\mathbf{b}}\big) \tag{4.11}$$

$$U(J) = \frac{1}{2}\,\kappa\left[\frac{1}{2}\left(J^2-1\right) - \ln J\right] \tag{4.12}$$

$$\bar{\Phi}\big(\bar{\mathbf{b}}\big) = \frac{1}{2}\,\mu\left(\operatorname{tr}\bar{\mathbf{b}} - 3\right), \tag{4.13}$$

where $\kappa$ is the bulk modulus, $\mu$ is the shear modulus, $\bar{\mathbf{b}} = J^{-2/3}\mathbf{b}$ is the deviatoric part of the left Cauchy-Green stretch tensor $\mathbf{b}$ (A.12), and $J = \det\mathbf{F}$ (A.26). This model is used because it is stable under severe compression. The simulations are performed in two dimensions so plane strain conditions are imposed on the three-dimensional constitutive model. The cohesive potential (2.37) proposed by Xu and Needleman[95] is used across all element boundaries in the cohesive network. In Figure 4.17, a shaded rectangle near the tip of the pre-crack indicates the region seeded with cohesive surfaces while the remainder of the domain is discretized with standard finite elements. As indicated in Figure 4.18, the region seeded with cohesive surfaces covers a region with height $\times$ width $=$ $7.2\,\text{mm} \times 3.6\,\text{mm}$. The "mesh unit cell" is composed of a rectangular cell, subdivided by diagonals to produce four, similar, triangular elements. Introducing the cohesive surface network into the finite element model increased the number of nodes from approximately 136,000 to 710,000 and additionally introduced 345,000 surface elements. We considered three rectangular unit cells with aspect ratios of $\frac{\text{height}}{\text{width}} = \left\{\frac{4}{3}, 1, \frac{2}{3}\right\}$. The dimension of the elements for each case is also shown in the lower portion of Figure 4.18. The characteristic element dimension in the region the crack propagates is approximately $50\,\mu$m, or on the order of 2000 times smaller than the overall model dimensions. For the study of convergence as a function of mesh resolution, a single mesh is used with a cross-cut square unit cell with dimension $50\,\mu$m. For these simulations, the uniformly meshed region through which the crack propagates is slightly larger than in the first case with dimensions height $\times$ width $= 9\,\text{mm} \times 16\,\text{mm}$. We use two background integration grids for the simulations using the VIB model with meshfree methods. Both grids make use of $50\,\mu$m rectangular cells although the cells in one grid are subdivided into four triangles to produce a different texture with approximately the same characteristic particle spacing. We locate a particle at every vertex of the grid. The cells also serve to define the location of Gauss integration points. The RKPM formulation described in Section 3.1 is used to compute the nodal shape functions. In all cases, the overall model dimensions are the same as the dimensions of the specimens used in the experiments.

To represent the properties of 18Ni900 steel, we select a Young's modulus of $E = 190\,\text{GPa}$, Poisson's ratio of $\nu = 0.3$, and a fracture toughness of $K_{Ic} = 68\,\text{MPa}\sqrt{\text{m}}$ from which we find a fracture energy of $\phi = 22.2\,\text{kJ/m}^2$. These parameters yield a characteristic opening $\delta_n$ for the cohesive surface relation from (2.56) of approximately $1.3\,\mu$m, assuming $E/\sigma_c = 10$. The impact with the projectile is approximated by prescribing a uniform velocity of $15\,\text{m/s}$ along the edge of

the sample hit by the projectile. A symmetry boundary condition is prescribed along the centerline of the specimen, and all other faces are traction free. The equations of motion (A.28) are integrated in time using an explicit, central difference scheme from the classical Newmark family of methods.

### 4.3.3 Results and discussion

The fracture path for three aspect ratios of the "mesh unit cell" are shown in Figure 4.18. The window of observation of these results is indicated in Figure 4.17 with a shaded rectangle near the tip of the initial pre-cracks. The simulations differ only in the layout of the mesh in the near tip region. Some common features in the fracture path are qualitatively reproduced. The appearance of

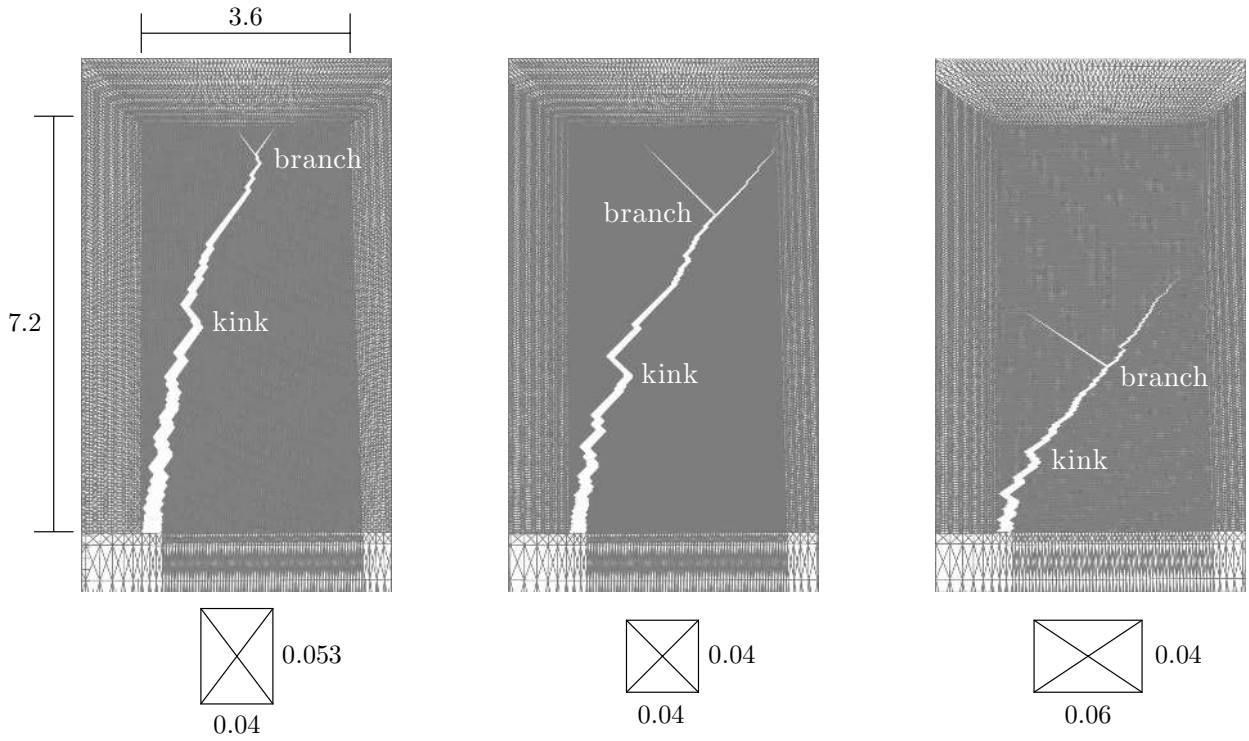


Figure 4.18: Simulations of the Kalthoff-Winkler experiment with different mesh designs (all units in mm).

pronounced kinks and a branch coincides with the arrival at the moving tip of strong waves reflected from the boundaries of the specimen. Most significantly, the results indicate that the fracture path is highly sensitivity to mesh texture, or alignment. In particular, the cracks propagated almost exclusively on the inclined facets of the mesh, avoiding the 0° and 90° facets.

For the cohesive network geometries shown, we propose two explanations for this behavior. First, we note that the cohesive zone condition (2.60) is not satisfied with the selected parameters, meaning that the surfaces act not like a network of continuum cohesive cracks but more like a network of individual, nonlinear springs analogous to the semi-empirical potentials used in molecular dynamics simulations. However, the springs are not all identical. The force acting between element edges scales with the area of each edge. With this view, we would expect fracture to proceed along weak paths through the medium. Indeed, the inclined facets for the geometries considered have

smaller areas than either the 0° and 90° facets. A second explanation does not require violation of the cohesive zone condition. In their study of fracture in orthotropic solids, Gao and Chiu[33] concluded that cracks will tend to propagate perpendicular to the "soft" direction in a material in order to maximize the energy release rate. This explanation suggests cracks will favor propagation perpendicular to the direction in the mesh with the smallest surface spacing. For the cross-cut mesh geometries considered in this study, the spacing of surfaces along inclined planes is always the smallest.

The results in Figure 4.19 show the effect of relative scaling between the fracture process zone and the mesh size. For these simulations, we use a single mesh, but scale the size of the fracture process zone by varying the cohesive strength $\sigma_c$ while keeping the fracture energy $\phi$ fixed. Since the bulk material is strictly hyperelastic and the size of the cohesive zone remains small compared with the relevant features of the model geometry, we would not expect the fracture path to depend strongly on the peak stresses near the crack tip or the size of the fracture process zone. Figures 4.19 (a)–(c) correspond to selecting $E/\sigma_c = \{30, 15, 10\}$, respectively. The continuum elements are colored with contours of the $\sigma_{11}$ component of the Cauchy stress. The times shown in the figure are in $\mu$s elapsed since the start of impact. Generally, we notice several features in the fracture paths. First, the fracture paths vary markedly as a function relative size of the fracture process zone. Second, the onset of propagation is delayed as the fracture process zone shrinks, or as $\sigma_c$ increases. Finally, we can again associate pronounced changes in the fracture path with the arrival of waves reflected from the boundaries of the specimen although this observation is not obvious from the limited number of snapshots presented for each case.

The analysis from Section 2.1.3 indicates that even with $E/\sigma_c = 30$, the parameters for these simulations do not satisfy the cohesive zone condition; however, Figure 4.19 (a) shows clear indications that a considerable modulus mismatch exists between the region initialized with the cohesive surface network and the regularly meshed region surrounding it. Further increasing $E/\sigma_c$ would produce even greater distortion of the elastic properties. The distortion in the modulus is so severe that the loading at the moving tip for this case may not be comparable with the others. For $E/\sigma_c = 15$, the mismatch is less pronounced though still visible. Comparing these two cases, we see that the crack finds a smoother path when the mesh size is reduced relative to the fracture process zone. For $E/\sigma_c = 10$, the onset of crack growth is delayed compared to the other cases. When the crack does extend, it grows a short distance but then becomes trapped from approximately 27 $\mu$s to 41 $\mu$s before extending again.

Figures 4.20 and 4.21 show the results of the simulations using the VIB model with RKPM. From the snapshots, we can see that the onset of growth and the crack velocity are in qualitative agreement with the results produced with the cohesive surface network. The experiment results did not include resolution of the crack growth over time. Unlike the results with the cohesive surface network, the fracture path predicted with the VIB model shows almost no effect from the interaction of the moving crack tip with waves reflected from the model boundaries. Comparing Figures 4.20 and 4.21, we see that changing the texture of the particle distribution does affect the fracture path. The crack grows at an average angle of approximately 63° and 79° for the two cases, respectively. The grid schematic shown in (c) for each figure shows that the angles chosen by the growing cracks do coincide with texture lines through the particle arrangements. However, the path does require the cracks to meander between particles to achieve the resulting propagation paths. We have not quantified the fracture energy anisotropy for propagation at different orientations through the grids used. The fracture path predicted by the VIB model will only be truly insensitive to texture with

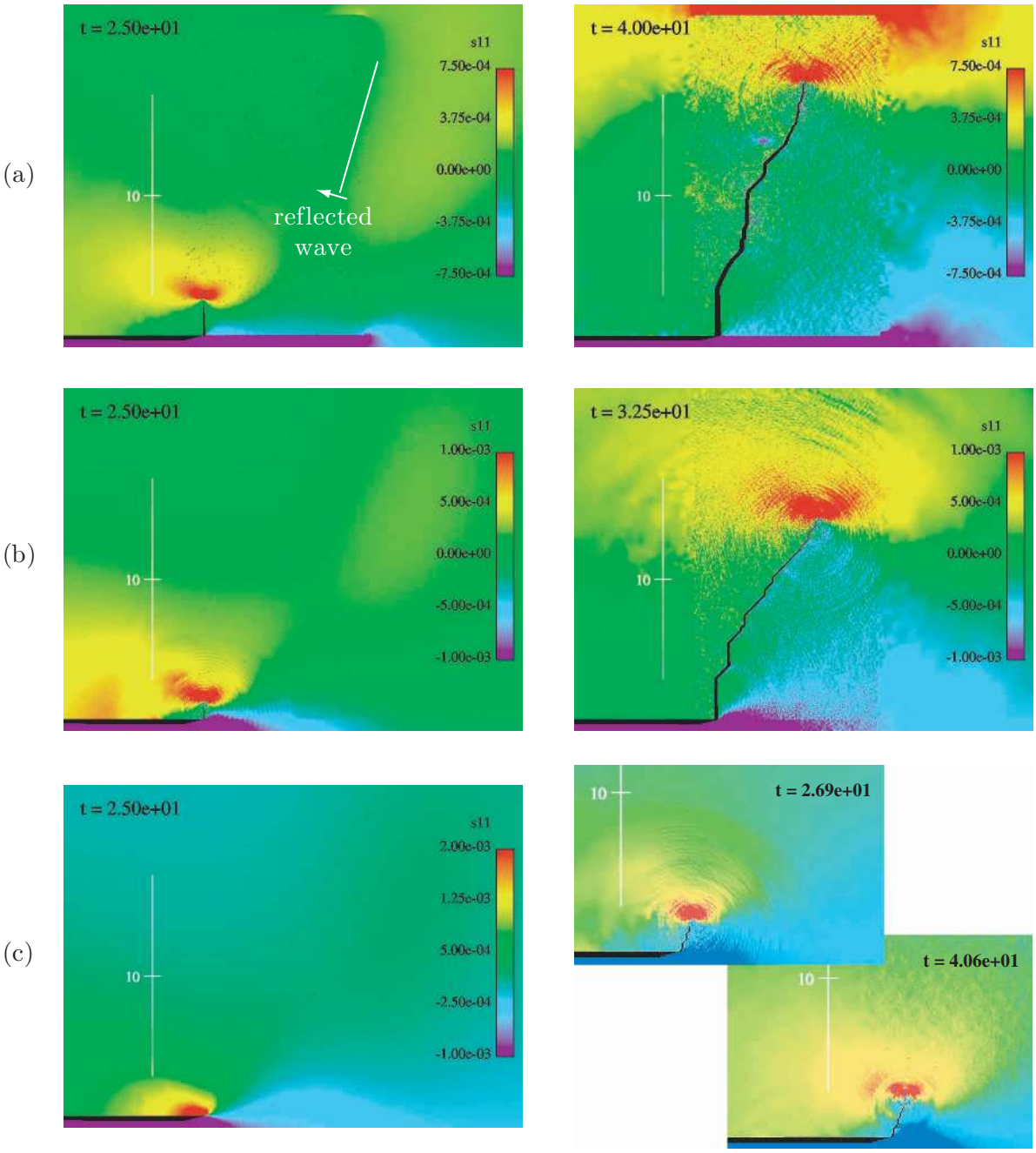


Figure 4.19: Fracture paths predicted using the cohesive surface network approach with $E/\sigma_c = 30$ (a), 15 (b), and 10 (c), shown with contours of $\sigma_{11}$.

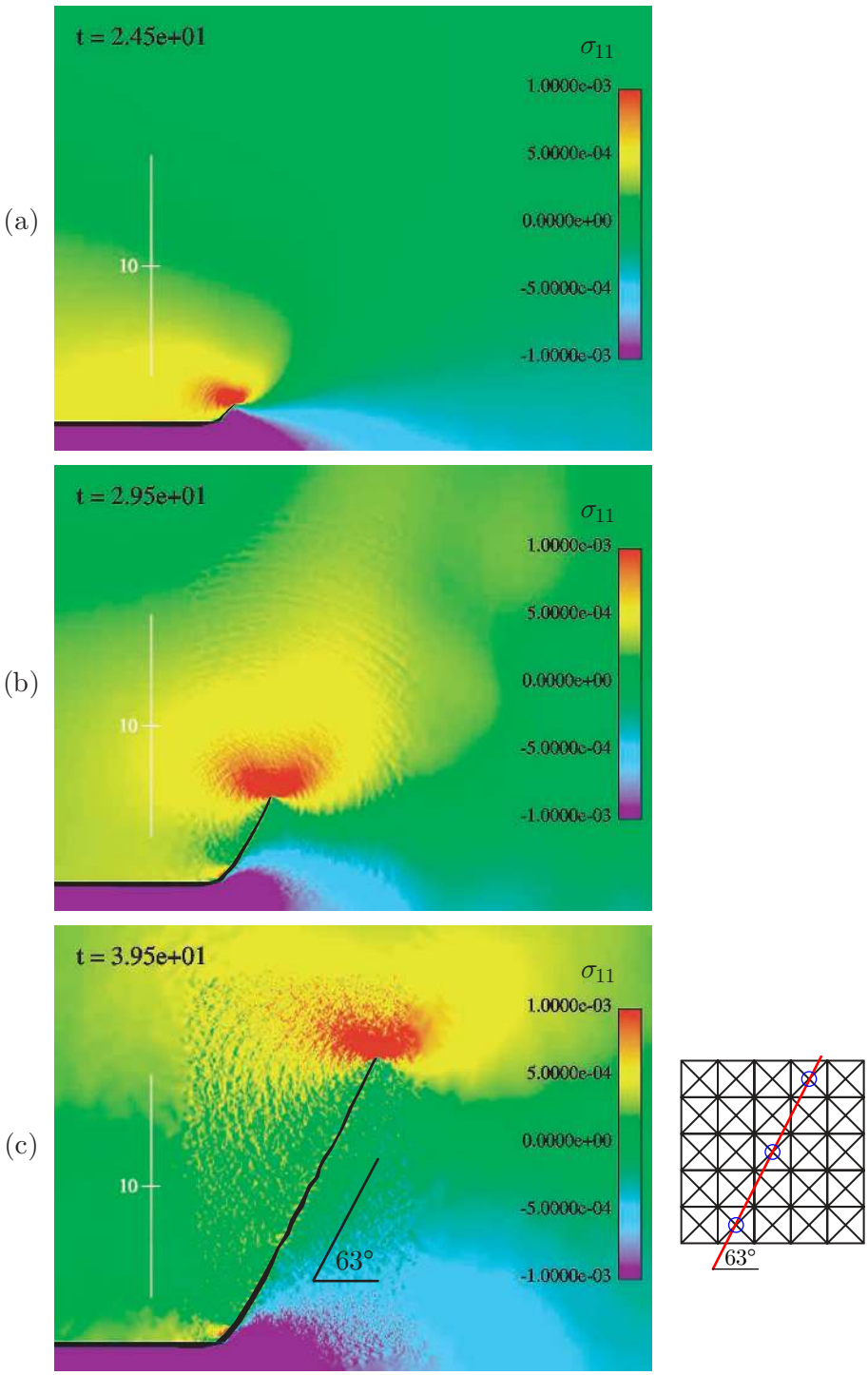


Figure 4.20: Results for the Kalthoff-Winkler simulations using VIB model with meshfree methods, on an integration grid with the texture illustrated in (c), showing the fracture path and contours of $\sigma_{11}$.

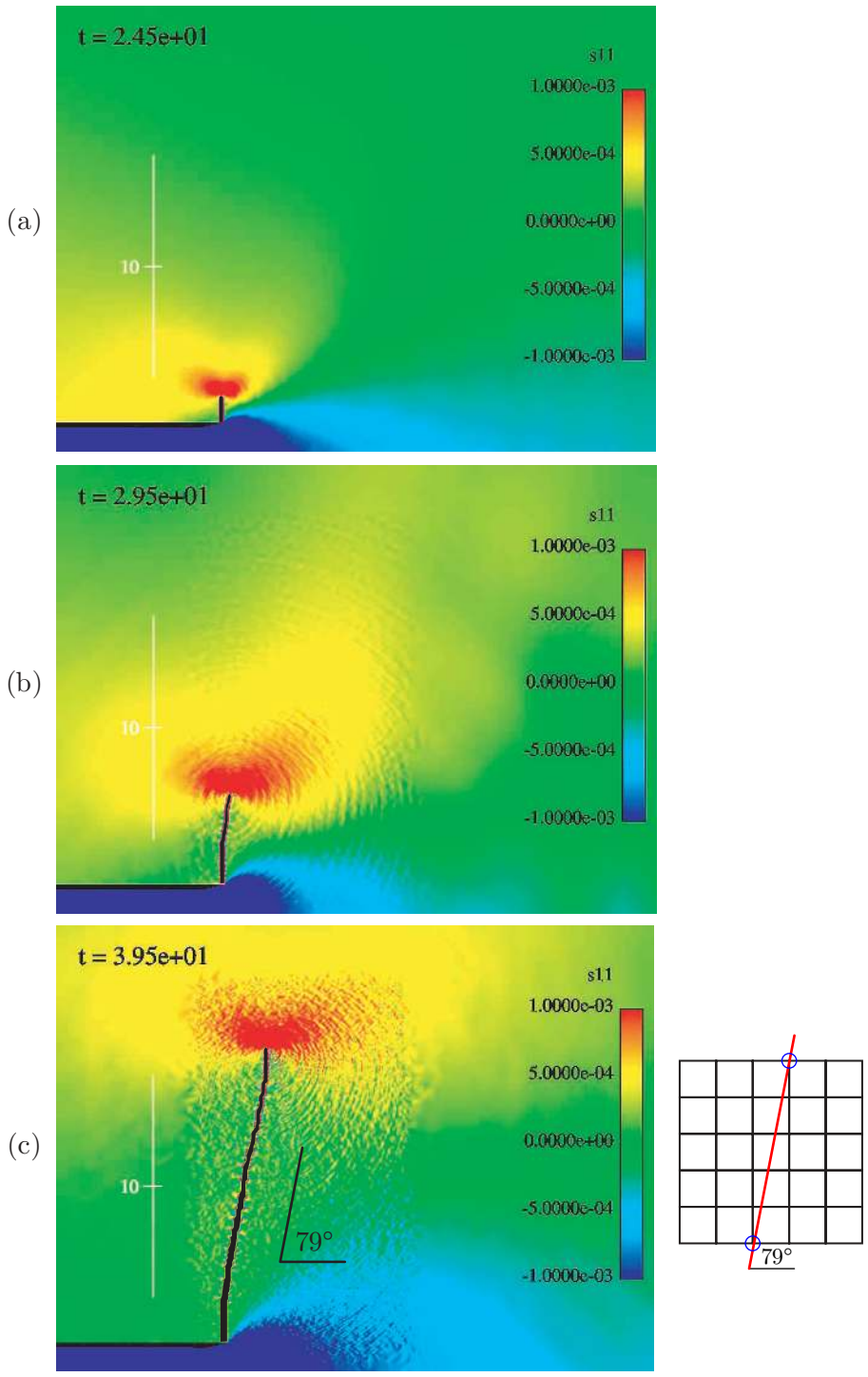


Figure 4.21: Results for the Kalthoff-Winkler simulations using VIB model with meshfree methods, on an integration grid with the texture illustrated in (c), showing the fracture path and contours of $\sigma_{11}$.

the addition of regularization for the localized mode.

## 4.4 Simulations of crack tip instabilities and branching

Cracks propagating at high speeds in brittle materials display behavior that the fracture community has yet to find consensus in explaining. Much of the current debate involves the factors that determine the terminal velocity of cracks and the cause of roughened fracture path produced under fast fracture. The experimental methods used to study dynamic fracture, some key experimental observations, as well as a review of a number of models that attempt to explain the observed phenomena are reviewed by Ravi-Chandar[74]. The theoretical limiting speed for cracks propagating under mode I loading is the Rayleigh surface wave speed $c_R$. However, experimental studies of cracks propagating through brittle materials typically find terminal crack speeds of approximately $c_R/2$, while instabilities have been observed for crack speeds as low as $c_R/3$. Detailed experiments of dynamic crack propagation through the brittle polymer Homalite-100 appear in the studies of Ravi-Chandar and Knauss[75, 76, 77, 78]. They observe the well-known "mirror-mist-hackle" appearance of the fracture surface. An image from their study[76] showing the fracture surface is reproduced in Figure 4.22.

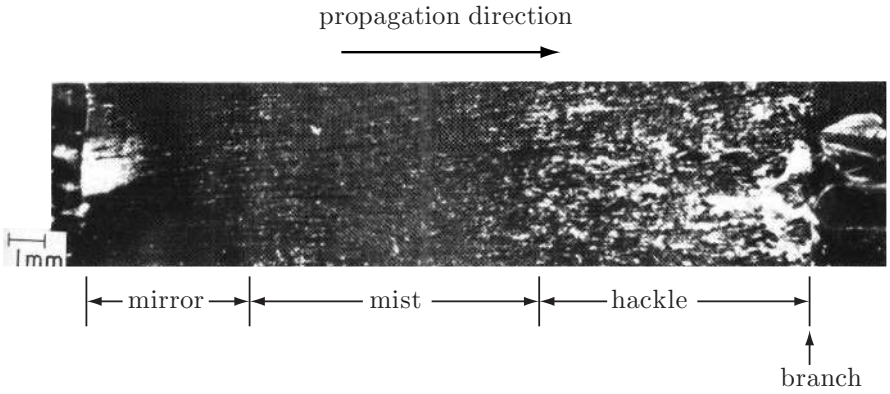


Figure 4.22: "Mirror-mist-hackle" appearance of a fracture surface observed by Ravi-Chandar and Knauss[75, 76, 77, 78].

The direction of crack propagation is from left to right in the figure. The image shows that the crack surface becomes progressively rougher as the crack extends and the crack speed gets correspondingly higher. By the method of caustics, they are able to observe distinctly different behavior in the propagating crack front that helps explain the appearance of the fracture surface. In the initial stages of growth, the crack extends by the propagation of a single, curved front, similar to what is observed under quasistatic conditions. The fracture surface appears essentially smooth, leading to its description as the "mirror" zone. As growth progresses, the crack front appears to extend by the action of multiple, smaller crack fronts. The opaque appearance of the crack surface due to fine-scale roughness leads to its description as the "mist" zone. In the "hackle" zone, the scale of the multiple crack fronts increases, leading to a larger degree of fracture surface roughening.

### 4.4.1 Theoretical analysis of branching

The emergence of crack tip instabilities under dynamic conditions was first predicted analytically in a study by Yoffe[97]. Her analysis predicts branching at 60° when the propagation speed reaches

approximately $0.6\,c_R$. Though the result is significant in demonstrating the onset of fracture path instabilities, neither the crack speed nor the branching angle agrees well with experimental observations. Branching angles typically fall between $10^\circ$ and $45^\circ$, while instabilities appear at speeds well below Yoffe's predicted value. In particular, Fineberg *et al.* [27, 28] make detailed measurements of crack propagation in PMMA, showing the onset of oscillatory behavior in the crack tip at speeds of roughly $c_R/3$. Classical theories are unable to explain the development of crack tip instabilities at these speeds. Gao[31, 32] suggests that the hyperelastic nature of crack tip deformation may be essential for understanding dynamic crack tip instabilities. Elastic softening due to hyperelastic stretching can drastically change the way acoustic waves propagate in a solid. The variation in the elastic properties with deformation referred to in this setting should not be associated with models of continuum damage. Damage models attempt to incorporate the effects of microstructural evolution in the behavior of a material, such as microcrack distributions[42] or the nucleation and coalescence of voids[38]. The elastic softening under consideration in the present context is an effect of the continuously varying stiffness of a nonlinear cohesive interaction. To illustrate this point, let us consider how a long wavelength signal propagates along an atomic chain stretched toward its cohesive limit. Before the chain is stretched, it behaves like an elastic bar along which a longitudinal wave can be transmitted with a speed of $\sqrt{E/\rho}$, where $E$ denotes the initial stiffness (Young's modulus) and $\rho$ the density of the chain. As the chain is stretched near its cohesive (fracture) limit, the tangent stiffness vanishes while a finite tension builds with a magnitude approaching the cohesive stress $T_{\max}$. At the cohesive point, the chain behaves like an elastic string along which a transverse wave can be transmitted with a speed of $\sqrt{T_{\max}/\rho}$. Note that the cohesive-state wave speed depends on the magnitude of the stress rather than the slope of the stress-strain curve. During this hyperelastic deformation, the slope of the force-displacement (or stress-strain) curve continuously decreases from its initial value corresponding to the elastic stiffness of the chain, and ultimately vanishes at the cohesive limit. Clearly, a linear theory assuming constant stiffness cannot be used to investigate the behavior of the chain near its failure point.

Generalizing the above concept, Gao[31, 32] shows that a homogeneous, isotropic, hyperelastic solid exhibits this string-like behavior near its plane strain equibiaxial cohesive stress in that the cohesive-state wave speed is equal to $\sqrt{\sigma_{\max}/\rho}$, where $\sigma_{\max}$ is the cohesive stress and $\rho$ is the density of the undeformed solid. The state of plane strain equibiaxial stress resembles the condition that a material particle experiences in front of a mode I crack tip. This observation comes directly from Irwin's[41] classic crack tip fields. This cohesive state is identified as the bottleneck state[31] for transmission of fracture signals ahead of a mode I crack tip. The crack propagation velocity is limited by how fast elastic waves can transport strain energy ahead of the crack to sustain the bond breaking processes in the fracture process zone. From this point of view, the cohesive-state wave speed leads to the concept of local limiting fracture speed[31] which has provided an explanation for the "mirror-mist-hackle" instabilities. Assuming values of $\sigma_{\max} = E/30$ and a Poisson's ratio of $\nu = 1/4$, the cohesive state wave speed is roughly $0.32\,c_R$, which is in good agreement with Fineberg's measurements. Gao's[30] wavy crack model presents a multiscale view of a dynamic crack in which the global, or apparent, crack speed is driven near $c_R/2$ to maximize the fracture energy absorbed by the advancing crack, while the microscopic tip speed may be significantly higher in response to local crack driving forces. A multiscale view may also be helpful in understanding the "mirror-mist-hackle" instabilities as the crack path begins to deviate in an attempt to circumvent the acoustic barrier presented by elastically softened material immediately ahead of the crack. Hyperelastic constitutive models that are capable of describing a material's transition to fracture

have not been available for studying these effects. As will be shown, the Virtual Internal Bond (VIB) model displays this cohesive state behavior and should therefore be capable of reproducing dynamic crack tip instabilities.

The atomistic simulations of Abraham *et al.* [2, 1] display dynamic crack instabilities reminiscent of the experimental results though at decidedly smaller length and time scales. The numerical studies of Xu and Needleman[95], employing networks of cohesive surface elements, are also successful in producing crack tip instabilities that qualitatively match the experimentally observed behavior. In their study, the continuum elements are modeled using the Kirchhoff-St.Venant constitutive relations, that do not display any softening, while the cohesive surfaces are governed by a traction-separation potential with qualitative features similar to those discussed for the potential in Section 2.2.2. Their observation of instabilities may also be explained with the local limiting speed theory since the "composite" material composed of continuum elements with intervening cohesive surfaces has the effective properties of a cohesive continuum, though with mesh dependent anisotropic characteristics.

### 4.4.2 Problem statement

We approach the simulations of dynamic crack tip instabilities and branching from two perspectives. First, we use a restricted form of the adaptive cohesive surface procedure, described in Section 3.4, in two-dimensional simulations to verify the adaptive approach under conditions of dynamic crack propagation. In order to demonstrate the capability of the VIB model to reproduce dynamic crack tip instabilities, we present two-dimensional simulations using the plane stress, isotropic VIB model and three-dimensional simulations using the VIB model in principal stretches[46]. Details of the VIB model in principal stretches are not described in this report, but we note that expressing the model in principal stretches greatly improves computational efficiency for three-dimensional problems.

The geometry of the simulation models is shown in Figure 4.23. As noted in the figure, the three-dimensional model possesses considerably more degrees of freedom although its overall dimensions are smaller. The two-dimensional model contains 159,175 nodes in 158,705 elements for a total of 318,106 degrees of freedom, accounting for the nodes with prescribed kinematic boundary conditions. The three-dimensional model contains 1,305,702 nodes in 1,260,000 elements for a total of 3,865,800 degrees of freedom. The models are loaded by symmetrically prescribed velocity boundary conditions for the nodes along the upper and lower edges of the domains. The boundary nodes are accelerated to the prescribed velocity over a time of $0.2\,\mu$s, essentially simulating an impact load. Additional boundary conditions are prescribed to prevent rigid body motion. The remaining surfaces are traction-free. Because the upper and lower surfaces of the model are displaced uniformly, this configuration nearly approximates a steady-state propagation condition for which extension of the crack may be viewed as a rigid body translation of the crack tip.

With these boundary conditions, a quasistatic analysis predicts that the crack instantaneously passes through the entire length of the sample once a critical displacement of the boundaries is reached. Unstable crack propagation also results for fracture under dead-loading, or the application boundary forces or tractions rather than fixed displacements. The intervening propagation can only be studied by dynamic analysis. The situation provides well-defined conditions under which we can study the physics governing crack tip behavior. Xu and Needleman[95] studied a similar configuration using the cohesive surface network approach. Since the network approach leads to

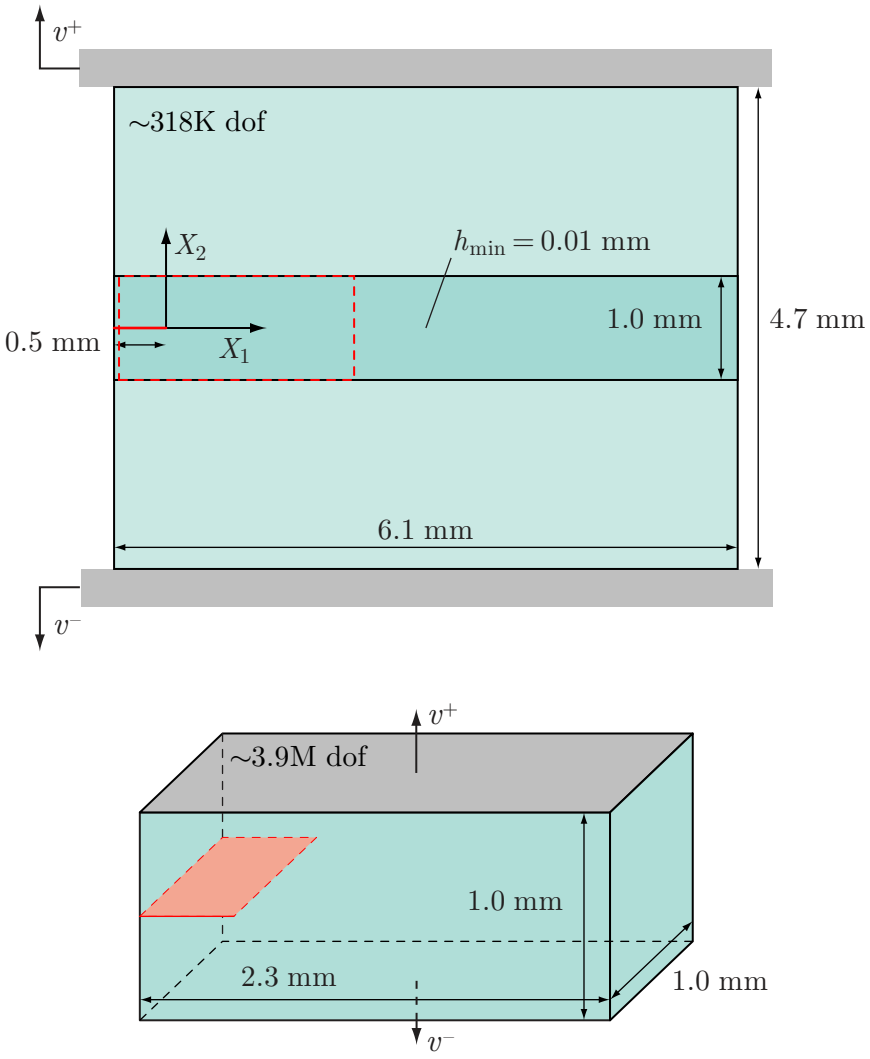


Figure 4.23: Geometry and dimensions of the two- and three-dimensional simulation models used to study dynamic crack tip instabilities. The size of the three-dimensional model is shown on the two-dimensional model with a dashed outline.

a reduction of the modulus with increased mesh refinement, as shown in Section 2.1.3, it is not suitable for predicting the terminal crack velocity. Xu and Needleman's results show a systematic decrease in the terminal velocity as the characteristic mesh size is reduced. Furthermore, the combination of hyperelastic bulk constitutive behavior with cohesive surface interactions creates results in a "composite" effective bulk response that the VIB model was specifically formulated to display. However, the VIB model does not suffer from mesh-dependent elastic anisotropy.

The two-dimensional calculations with adaptive insertion of cohesive surfaces employ a total Lagrangian formulation, allowing the meshfree RKPM shape functions to be calculated only once and recalculated locally for the field points affected by the moving crack. Propagation is limited to the straight ahead direction by sampling the insertion criterion at only a single position ahead of the crack front, a point for the two-dimensional case. The configuration of the moving crack is described in Section 3.4. In terms of the parameters illustrated in Figure 3.7, we select the crack extension increment and sampling radius as $\delta a = r = h$, where $h = 0.01\,\text{mm}$ is the particle spacing. We use the cohesive relation $\mathbf{T}(\boldsymbol{\Delta})$ given by (2.49), which displays a linear decay in the cohesive tractions with monotonic increase of the opening displacement. The cohesive strength and initial cohesive surface traction is $\sigma_c = |\mathbf{T}_0| = E/30$. A critical hoop stress $\sigma^*_{\theta\theta}$ is used to determine the insertion of cohesive surfaces. In principle, the cohesive tractions should remove the stress singularity resulting from the geometric discontinuity at the crack tip. This regularization of the stresses around the tip should eliminate convergence problems associated with the point-wise insertion criterion. To test the sensitivity of the adaptive procedure to the sampling parameters arising from the numerical implementation, we use three different values of the insertion stress $\frac{\sigma^*_{\theta\theta}}{\sigma_c} = \left\{1, \frac{3}{4}, \frac{1}{2}\right\}$. Alternatively, we could vary the sampling distance $r$ since this would also change the stresses at the sampling point. The constitutive model used for the bulk is the finite strain, isotropic model described by (4.11) through (4.13). Since the bulk behavior is hyperelastic, we would not expect the detailed form of the cohesive surfaces relations to have a strong effect on the crack growth behavior as long as mesh is sufficiently refined to capture the tractions in the fracture process zone. For the two-dimensional calculations using the VIB model, an updated Lagrangian finite element formulation is used. The three-dimensional calculations use RKPM in a total Lagrangian formulation. The equations of motion(A.28) are integrated in time using an explicit, central difference scheme from the classical Newmark family of methods. The three-dimensional calculations are performed by decomposing the model into 50 partitions by a static, graph-based scheme to minimize communication while balancing the computational load. The decomposed model is shown in Figure 4.24. Description of the parallel aspects of meshfree calculations is not a focus of this report; however, we do point out a communication issue inherent in meshfree methods. In Figure 4.24 (b), the particles are shaded to differentiate those that are involved in calculations in more than one partition. With meshfree methods, these communicated layers are "thicker" than those that would result from an analogous decomposition of the model for a standard finite element method. The width of this layer depends on the support size selected for the nodal shape functions, which is generally larger the support size of a standard finite element shape function over the same arrangement of nodes.

The material parameters are selected to be representative of PMMA, the material used in the experiments of Fineberg[27, 28], with $E = 3.24\,\text{GPa}$, $\nu$ constrained by Cauchy symmetry as described in Section 2.2.1, and $\rho = 1200\,\text{kg/m}^3$. These values produce dilatational and shear wave speeds of $c_d = 1740\,\text{m/s}$ and $c_s = 1000\,\text{m/s}$, respectively, and a Rayleigh wave speed[29] given by

$$c_R = c_s \frac{0.862 + 1.14\,\nu}{1 + \nu} = 932\,\text{m/s}. \tag{4.14}$$

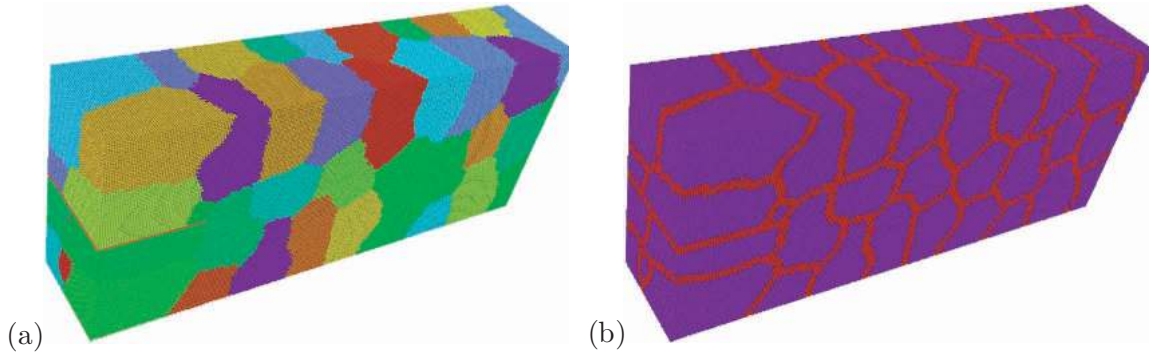


Figure 4.24: Decomposed model used for the three-dimensional simulations showing (a) the particles colored by partition and (b) the particles shaded to indicate those communicated across partitions.

The fracture energy is selected as $350\,\mathrm{J/m^2}$, and the cohesive strength is selected as $E/30$. A $J$-integral analysis can be used to show that the fracture energy depends on mesh size with the current form of the VIB model[45]. The given cohesive parameters dictate that elements in the central region of height 1.0 mm have dimension of $h = 9.2\,\mu$m. For the two-dimensional simulations, four-noded quadrilateral elements, integration cells for the meshfree calculations, are used throughout the model. The central region is meshed with a regular arrangement of square elements with dimension $9.2\,\mu$m while the elements in the outer region increase in size with distance away from the central zone. For the simulations using adaptive insertion of cohesive surfaces, the meshfree field in the central region of the specimen is coupled to finite elements in the upper and lower regions using the procedure proposed by Belytschko *et al.* [12]. For the three-dimensional simulations, the entire domain is discretized into a regular, structured grid of eight-noded hexahedral "bricks" with dimension $9.2\,\mu$m, and RKPM is used for the entire domain.

A pre-crack of length 0.5 mm ensures that propagation is initially directed along the centerline of the model, though its path is not prescribed in any way for the VIB simulations. The simulation results show that crack growth, instabilities, and branching emerge naturally from the properties of the VIB constitutive model. For the two-dimensional VIB simulations, the apparent length of the crack is monitored by tracking the elements in which the acoustical tensor (A.31) is no longer positive definite. Checking this condition requires searching all wave propagation directions to see if there are any for which the wave speeds vanish. Since the models are constrained to prevent rigid body translations, the crack length is taken as the greatest distance along $X_1$ between the original crack tip position and the centroids of localized elements in the undeformed configuration. The time step for the explicit integration scheme is selected so that $\Delta t\, c_d/h = 1/3$, where $h$ is the minimum element size, or characteristic particle spacing.

### 4.4.3 Results and discussion

The crack growth predicted by the adaptive procedure for the three different values of the insertion stress $\sigma^*_{\theta\theta}$ is shown in Figure 4.26. The prescribed velocity at the upper and lower boundaries is $v_{BC} = 5.2\,\mathrm{m/s}$. The crack length is shown as a function of time in Figure 4.26 (a). Figure 4.26 (b) shows the crack velocity, calculated by a finite difference approximation of the crack length, nor-

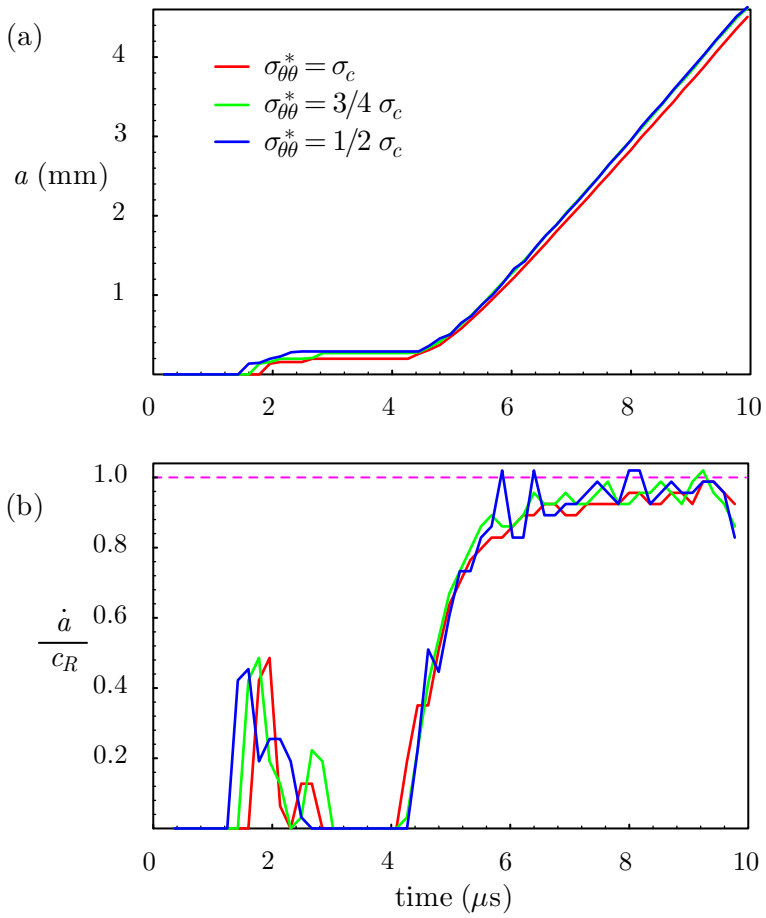


Figure 4.25: Crack length (a) and crack velocity (b) predicted by adaptive insertion of cohesive surfaces for different values of $\sigma^*_{\theta\theta}$, the stress at which new surfaces are created.

malized by the Rayleigh wave speed $c_R$. We denote the location of the peak tractions as the crack tip. There are a number of noteworthy features in the results. First, except for the initial jump in the crack length at approximately $2\,\mu$s, the results for the three different cases are relatively insensitive to the choice of $\sigma^*_{\theta\theta}$. We would expect some initial difference in the movement of the crack tip because the regularizing effects of the cohesive tractions act only after the process zone has fully formed. As the cohesive zone forms, we observe $R$-curve behavior, the fracture resistance appears to increase with crack growth. Once the cohesive zone has formed, the crack tip remains stationary until the critical energy release rate is attained. For all three cases, crack extension begins in earnest after $4\,\mu$s, indicating that the growth is controlled by the properties of the cohesive relation not by artifacts introduced by the numerical implementation. The crack velocity quickly increases to nearly $c_R$, the theoretical limiting speed for cracks propagating in mode I. However, this is nearly twice the speed observed by Fineberg *et al.* [28] in their experiments. This result indicates that the insertion procedure used for these calculation, though producing convergent results in agreement with theoretical predictions, fails to capture the physics governing the terminal

velocity of propagating cracks. In our ongoing work, we will activate additional components of the tip model, such as allowing for a wavy fracture path or crack branching, to determine the effects each of these phenomena introduces.

Figure 4.26 shows the contours of $\sigma_{11}$ and $\sigma_{22}$ surrounding the crack tip $9\,\mu$s after loading is initiated. The particles are plotted in the deformed configuration. We note the growing crack is represented by local modification of the nodal shape functions, as illustrated in Figure 3.2. No remeshing is performed. The contours of stress show that the crack tips are trailed by oscillatory features in the stress fields that decay quickly with distance away from the fracture surface. Interestingly, the source of the disturbance, the moving crack tip, is moving at the speed these waves propagate. Yoffe's[97] solution for the hoop stress around a crack tip moving at a constant velocity in a linear elastic medium indicates that peak hoop stress is not directly ahead of the tip at speeds greater than $0.6\,c_R$. The contours of both $\sigma_{11}$ and $\sigma_{22}$ indicate that strong stresses develop away from the fracture plane.

Next, we present results of the two-dimensional simulations using the VIB model for three values of the prescribed boundary velocity, $v_{BC} = \{2.6, 5.2, 10.4\}$ m/s. The crack length as a function of the simulation time for all three cases is shown in Figure 4.27. The two-dimensional calculations are performed with standard finite element methods while the three-dimensional calculations use RKPM. The time to the initiation of crack growth decreases as the impact velocity increases, presumably in response to the time required to generate the critical driving force at the initial crack tip. For the impact velocities of 2.6 m/s and 5.2 m/s, the figure shows that the crack moves forward and then stops before accelerating to the terminal velocity. Based on the dimensions of the model and the dilatational wave speed in the material, the initial loading wave reaches the crack tip from the boundaries after roughly $1.35\,\mu$s. An average terminal velocity is calculated for each case from the slope of the crack length curves $a(t)$ beyond the initial transient behavior. The terminal velocity increases from $0.48\,c_R$ to $0.53\,c_R$ as the impact velocity increases from 2.6 to 10.4 m/s.

Figure 4.28 shows the crack morphologies for the three cases. Each point along the fracture path marks an element for which the acoustical tensor condition for localization is satisfied at one or more of the element integration points. The images in the figure actually correspond to superpositions of the fracture path history over the entire simulation time. Since the VIB model is entirely elastic and does not incorporate any irreversibility in the fracture processes, secondary branches along the fracture path "heal" after the leading edge of the crack has advanced far enough to unload the material in its wake. The fracture paths indicate that the cracks initially propagate straight ahead along the symmetry line of the domain. In each case, the first deviation from straightforward propagation is marked by a symmetric branch at roughly 10-15° to the initial crack plane. This first branch occurs sooner in time and at a shorter crack length as the impact velocity is increased. The subsequent fracture path becomes more irregular as one of the two branches arrests while the other continues to propagate. Once the symmetry of the original propagation has been disrupted, the branches become more irregular. In both Figures 4.28(b) and (c), the branching angles become noticeably larger as the crack advances, reaching a maximum angle of approximately 35° in (b), and reaching almost 55° in (c).

The initial, straight ahead propagation of the crack is "mirror"-like, while the branching at later times forms a "hackle" zone. What is not evident from the fracture paths shown in Figure 4.28 is that some indication of instability appears ahead of the crack tip significantly earlier than the occurrence of the first branch, representing the "mist" mode of propagation. Figure 4.29 shows the elements in which the acoustical tensor condition is met at four instants leading to the first

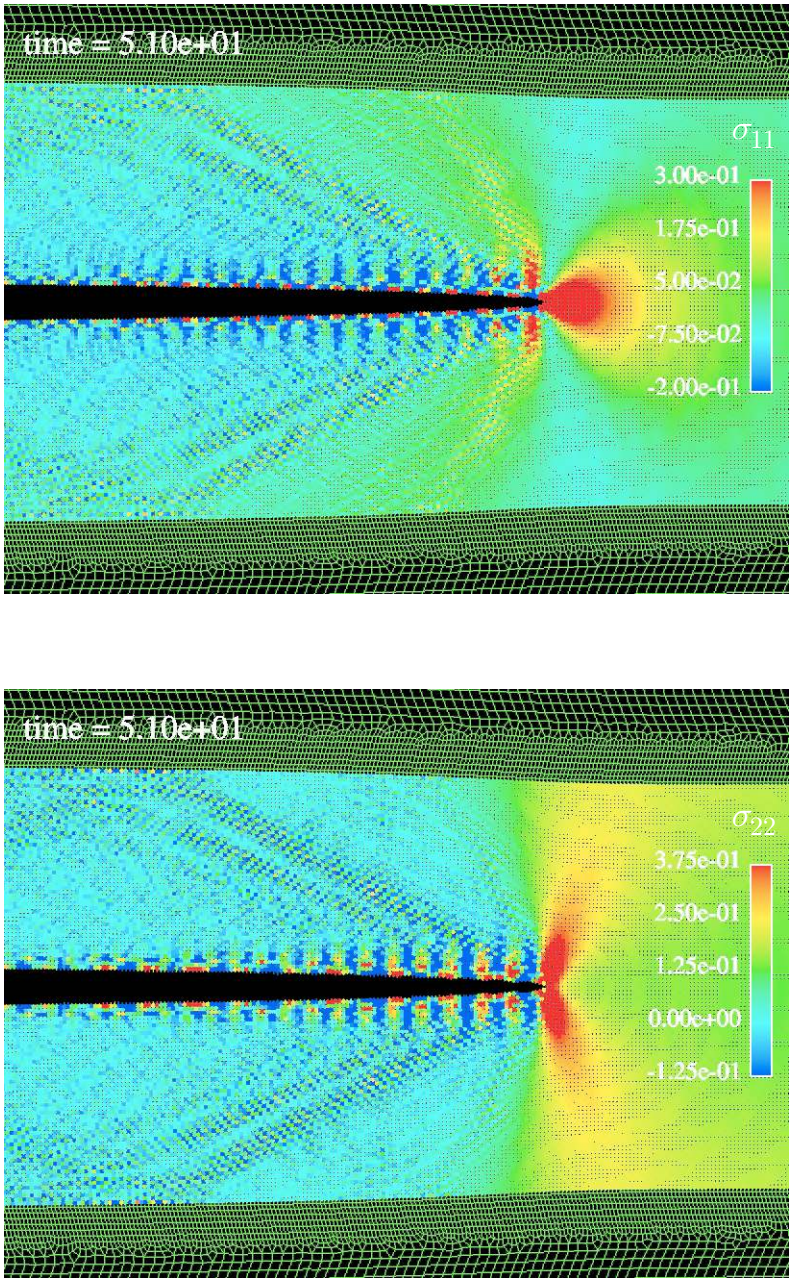


Figure 4.26: Contours of (a) $\sigma_{11}$ and (b) $\sigma_{22}$ around a crack tip traveling at nearly the Rayleigh wave speed $c_R$, 9 $\mu$s after loading is initiated, simulated by adaptively inserting cohesive surfaces ahead of the tip.

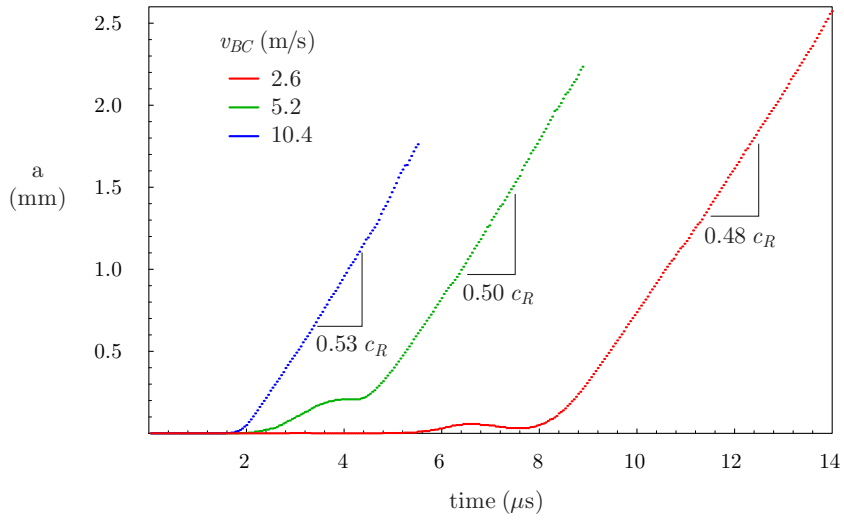


Figure 4.27: Apparent crack length over time for three different values of the imposed boundary velocity.

branch in the fracture path for the case of $v_{BC} = 5.2\,\text{m/s}$. Initially (a), all elements displaying localization lie along a straight path extending from the pre-crack. After $5.1\,\mu$s (b), the first evidence of localization in elements above and below the symmetry line appears. Based on the local limiting speed theory of dynamic crack tip instabilities, the crack has reached a speed at which the strain softened material immediately ahead of the crack is unable to maintain a sufficient rate of energy transfer, and the crack has begun to probe alternate propagation directions. Between 5.1 and $5.9\,\mu$s after impact (c), the crack continues to accelerate and the acoustical barrier ahead of the crack tip enlarges, evolving to an extended region of "damaged" material. Since deformations in the VIB model are strictly reversible, the material recovers as the tip moves away, leaving no indication of this extended region in the subsequent fracture path. At some time before $6.1\,\mu$s (d), the crack tip reaches a critical state, and the first true branch appears in the crack path. The sequence of Figures 4.29(a)–(d) bears resemblance to the "mirror-mist-hackle" progression of crack face roughness observed in experiments. The small scale roughness in the numerical results is too fine to be resolved with the current mesh dimensions, but the transition to larger scale roughness is clearly displayed.

The crack length data in Figure 4.27 can be numerically differentiated in order to calculate the apparent crack velocity as a function of time. The crack velocity, normalized by the Rayleigh wave speed $c_R$, for $v_{BC} = 5.2\,\text{m/s}$ is shown in Figure 4.30. As is evident from the crack length data, the crack moves forward at approximately $2.0\,\mu$s after the impact occurs, arrests, and then accelerates quickly to an average terminal velocity of approximately $0.5\,c_R$. As observed by Fineberg[28], the crack accelerates quickly, but continuously, instead of initiating at the terminal velocity. As the crack accelerates and rapid branching begins, the crack velocity becomes more irregular. This result qualitatively matches the experimental measurements as well as the numerical results obtained by Xu and Needleman[95]. Markers A–D indicate the times at which the crack is pictured in Figures 4.31–4.34. The four points correspond to (A) initial stages of propagation in the straight-ahead direction; (B) the point at which the small scale instabilities shown in Figure 4.29(b) appear;

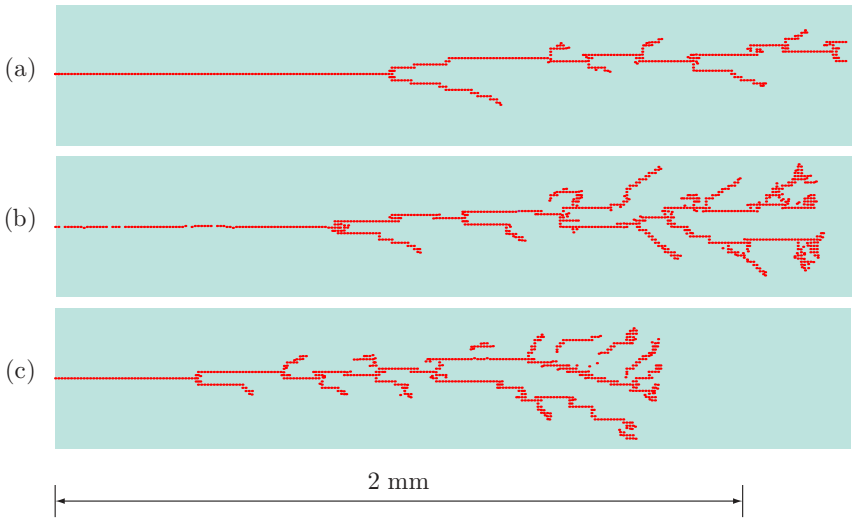


Figure 4.28: Fracture patterns for impact velocities of (a) $v_{BC} = 2.6\,\mathrm{m/s}$, (b) $v_{BC} = 5.2\,\mathrm{m/s}$, and (c) $v_{BC} = 10.4\,\mathrm{m/s}$.

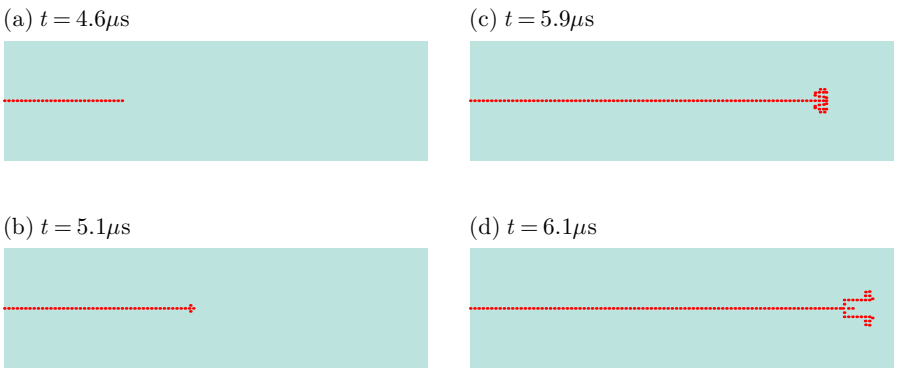


Figure 4.29: The onset of branching for $v_{BC} = 5.2\,\mathrm{m/s}$.

(C) the point shown in Figure 4.29(d) at which the first clear branch appears; and (D) propagation at the terminal velocity.

Figures 4.31–4.34 show two views of the propagating crack at the four points indicated in Figure 4.30. The upper plot (a) in each figure shows the distribution of the instantaneous shear wave speed $c_s$ for a wave traveling in the $X_1$-direction. The contours are normalized by the shear wave speed in the undeformed material $(c_s)_0$. These figures are intended to show how the highly deformed material undergoing fracture is affecting the transfer of crack driving energy to the region ahead of the tip. The shear wave speed also provides a clear indicator of the growing crack. The fracture path is more difficult to identify in the stress plots since elements are not removed from the simulation after the cohesive stress is reached. Stresses, though small, remain continuous across the crack faces, making the crack path difficult to locate. The lower plots (b) show the distribution of the crack opening stress $\sigma_{22}$, normalized by the cohesive stress $\sigma_c$. These plots show how the structure of the crack tip stress fields change as the crack propagates through the specimen.

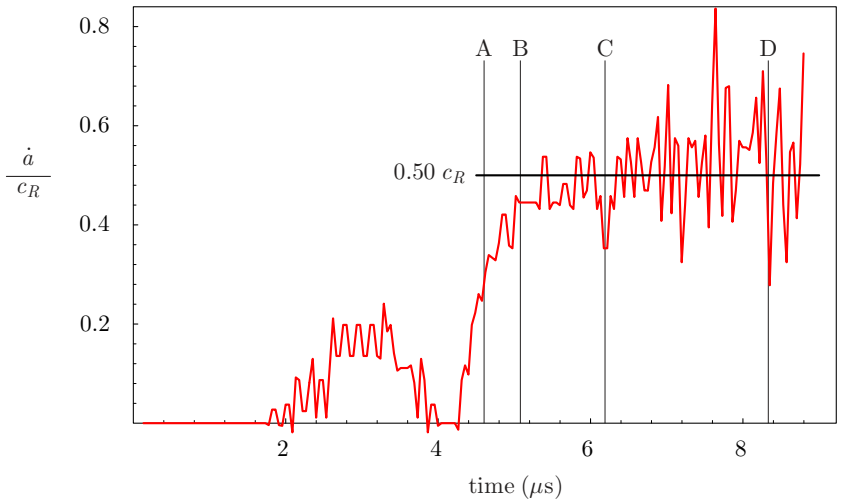


Figure 4.30: Apparent crack velocity $\dot{a}$ over time for an impact speed of $v_{BC} = 5.2\,\mathrm{m/s}$ with markers A–D indicating the times at which the crack is pictured in Figures 4.31–4.34.

Figure 4.31 shows the crack 4.6 $\mu$s after impact as it accelerates from the arrested state to a speed of approximately $0.3\,c_R$. In Fineberg's [28] results, the crack begins to display oscillatory behavior at this speed. Neither the shear wave speed distribution (a) nor the distribution of $\sigma_{22}$ (b) shows any signs of crack tip instability. The stress field, with a strong stress concentration marking the current tip position, displays the expected shape similar to the classical tip fields of Irwin[41]. Figure 4.32 shows the crack at 5.1 $\mu$s after impact, the time at which the acoustic barrier shown in Figure 4.29(b) has just started to form. The initial shape of a growing deformation-softened region is evident at the tip of the crack. The crack speed at this instant hovers around $0.4\,c_R$. Both the shear wave speed and the stress distribution display waves being emitted from the tip region in a manner that is not present in Figure 4.31. The stress fields do not display the stress oscillations seen in Figure 4.26 for the crack traveling at near $c_R$. Figure 4.33 shows the crack tip shortly after the initial branch in the fracture path. Both plots in the figure still display a high degree of symmetry. Elastic waves in the wake of the moving tip are even more evident. In the stress plot, the two tips are so close to each other that the combined stress field has a shape which resembles the field of a single tip, though the extent of the highly stressed material is much larger. Clearly, the crack tips are interacting so strongly that crack propagation criteria relying on classic $K$-field analyses are inapplicable. The final plots in Figure 4.34 show the crack in a late stage of the simulation. Several branches are clearly visible. Both plots display a degree of chaotic behavior as each tip individually seeks a fast fracture path. The highly stressed region ahead of the multiple crack tips extends over a tremendous area, and no resemblance to the classical crack tip fields remains.

In three dimensions, a standard finite element procedure proved insufficiently stable to simulate large scale branching[47]. The calculations failed due to tangling of the mesh around the moving crack front. Figure 4.35 shows the development of crack branching predicted using the VIB model with RKPM. Fracture is identified by probing the eigenvalues of the acoustical tensor (A.31), which are related to the wave propagation speeds in the material. In the figure, the surface indicates where the minimum shear wave speed has dropped to half of the value for the material in its reference state.

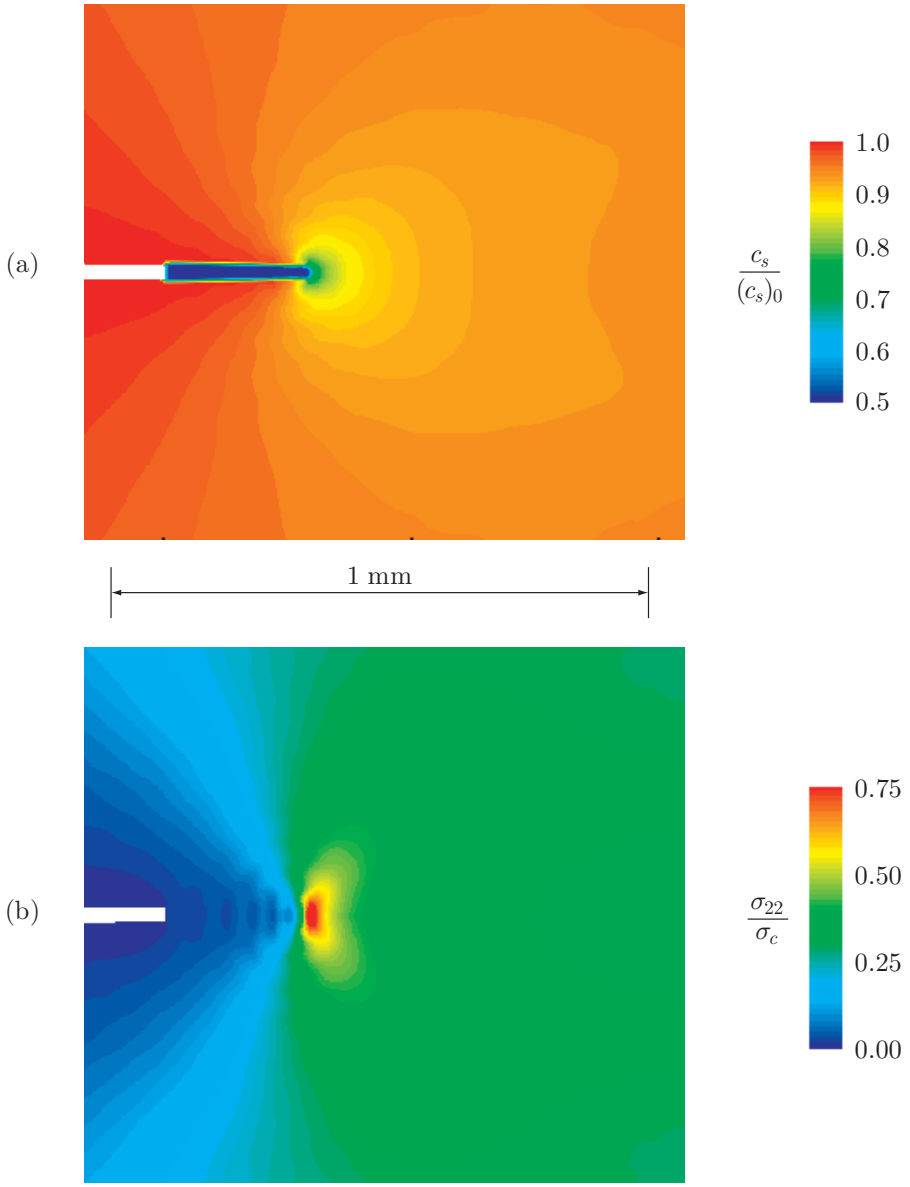


Figure 4.31: 4.6 $\mu$s after impact: (a) the distribution of the instantaneous shear wave speed normalized by the initial shear wave speed $(c_s)_0$ of a wave propagating in the $X_1$-direction and (b) the distribution of the $\sigma_{22}$ component normalized by the cohesive stress $\sigma_c$, both shown over the deformed domain.

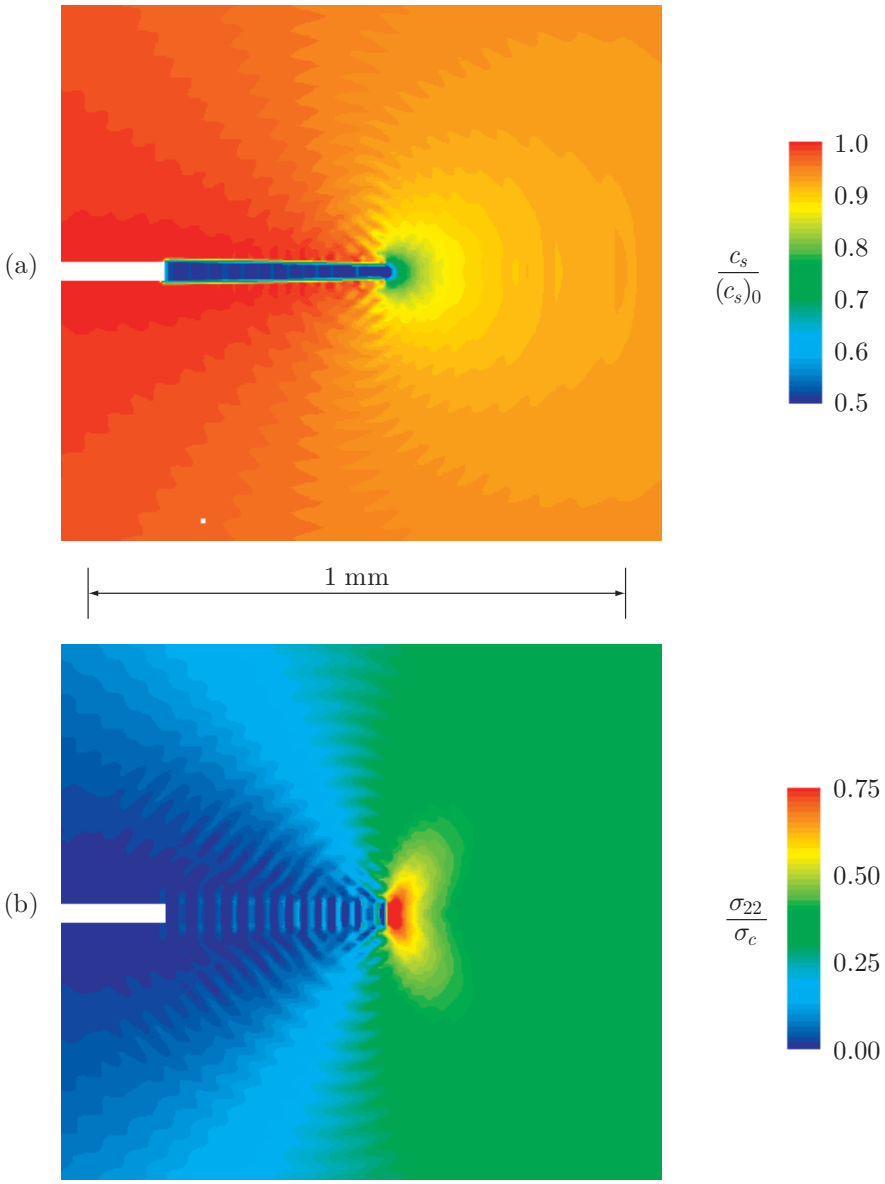


Figure 4.32: Contours of (a) the acoustical shear wave speed and (b) the opening stress 5.1 $\mu$s after impact.

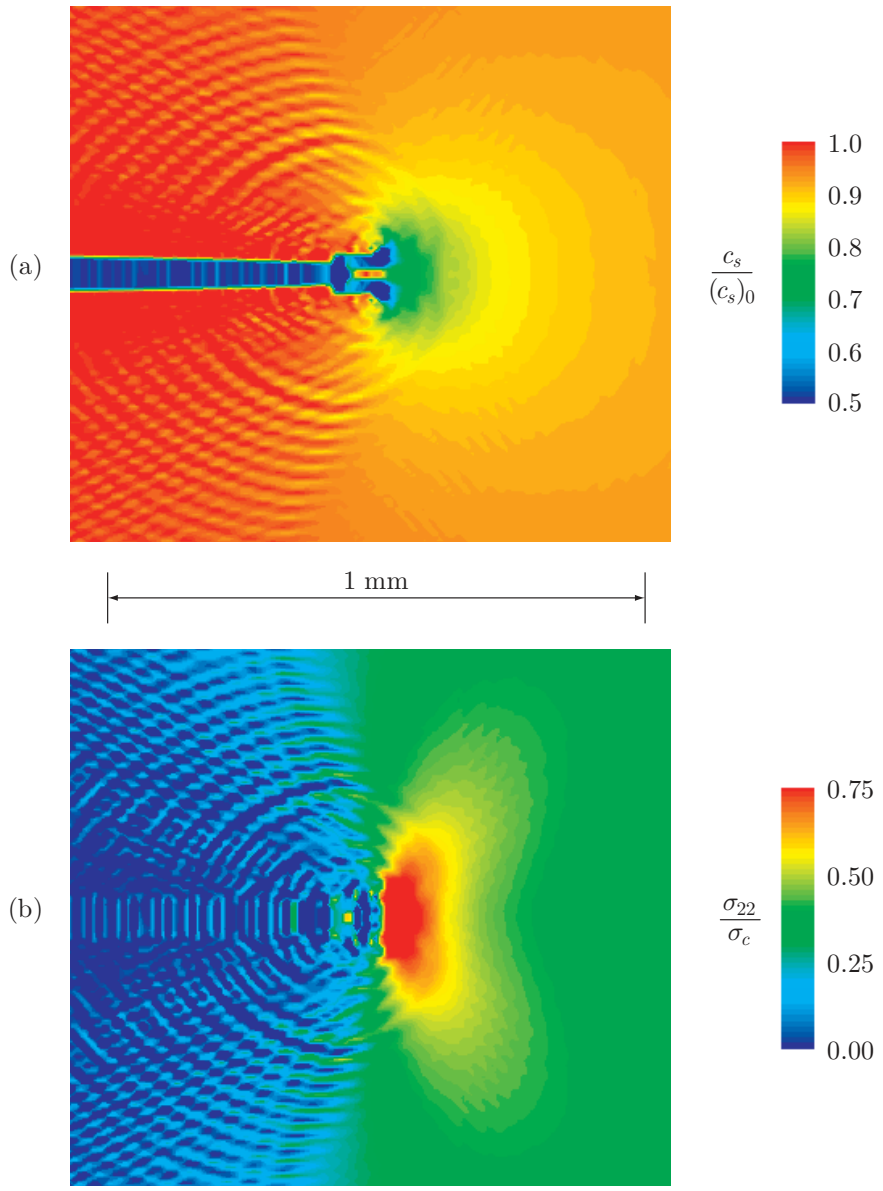


Figure 4.33: Contours of (a) the acoustical shear wave speed and (b) the opening stress 6.2 $\mu$s after impact.

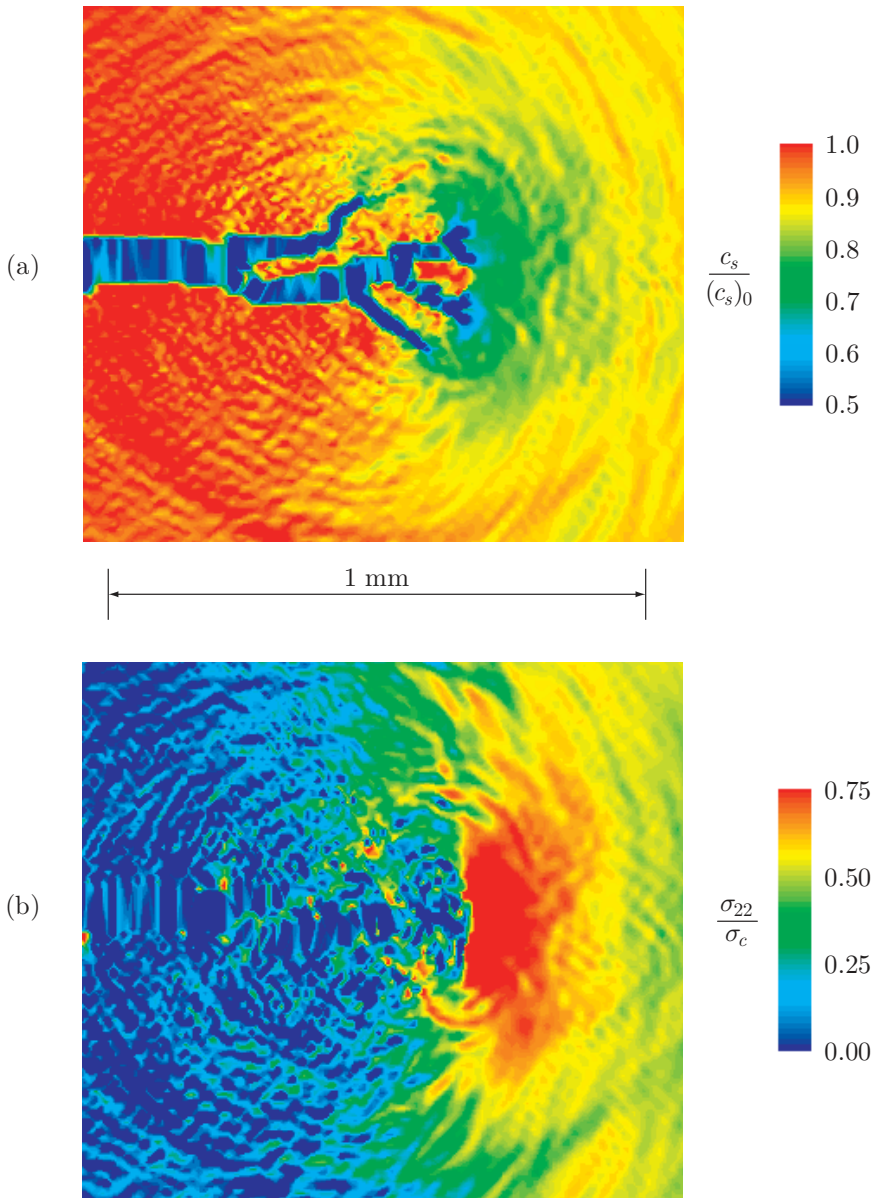


Figure 4.34: Contours of (a) the acoustical shear wave speed and (b) the opening stress 8.3 $\mu$s after impact.

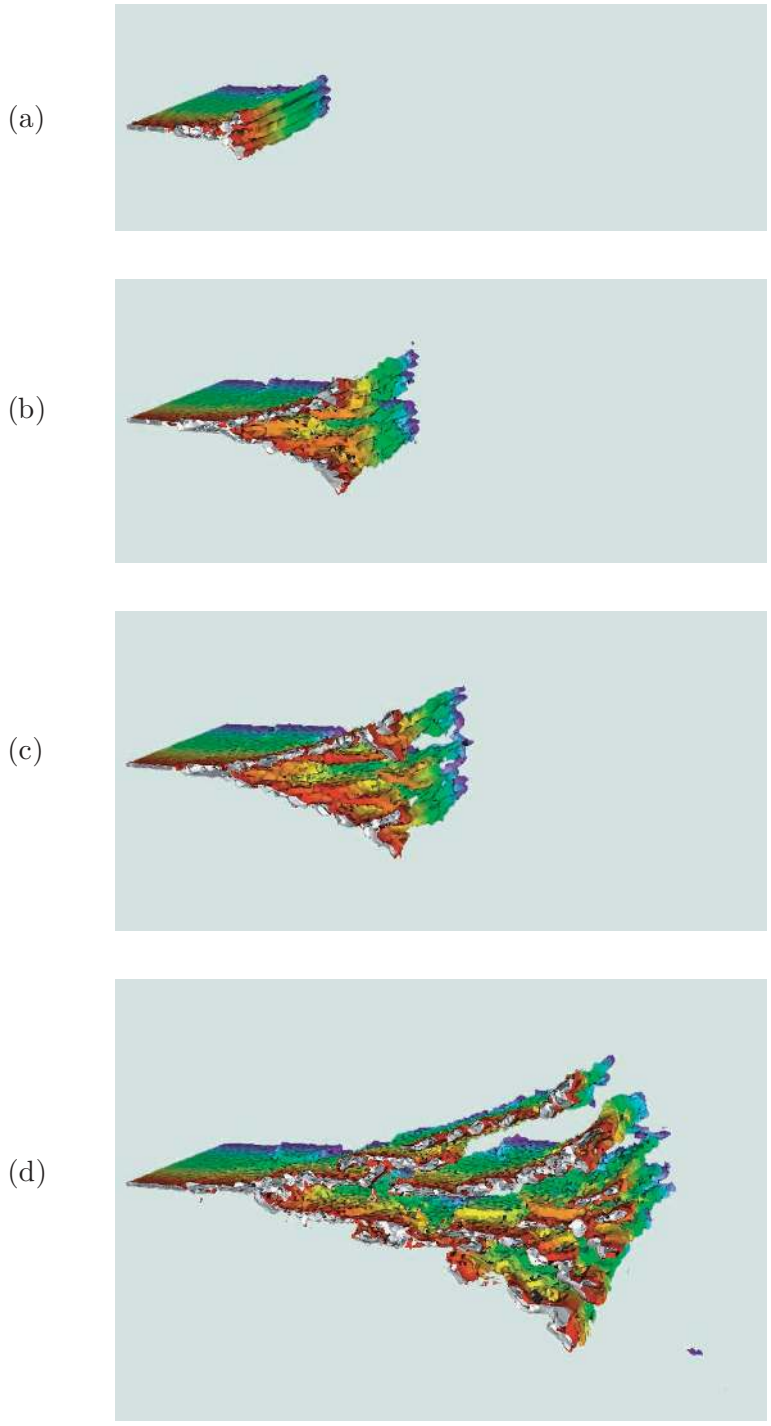


Figure 4.35: Simulations of crack branching in three dimensions.

The surface is shaded through the thickness to provide contrast for the complicated morphology that forms. Similar to the results for the two-dimensional calculations, Figure 4.35 (a) shows a pronounced region of "slow" material ahead of the propagating crack. Finite element calculations of the same conditions failed shortly after the crack reached this state. The regions of the crack front approaching the free surfaces trail behind the region of the crack front nearer the center of the domain. The first branches initiate an the free surfaces and propagate inward. Figures (b)–(d) show that further branching develops through the course of the simulation. Although the geometry and boundary conditions possess a degree of planar symmetry, the fracture patterns are clearly three-dimensional. Aside from selecting the material parameters and imposing the boundary conditions, the fracture patterns in Figure 4.35 are not prescribed in any way.

# 5 Summary

The promise of cohesive modeling is the simulation of generalized fracture without presumed fracture criteria. However, significant progress is still required in order to develop fracture simulation procedures based on this cohesive view. We limited this study to consideration of brittle fracture in an effort to isolate general issues associated with cohesive formulations and numerical procedures from the materials science issues associated with developing cohesive relations that capture the effect of specific dissipation mechanisms. Even in the idealized forms used in this study, cohesive relations for both bulk and surface models exhibit a finite strength and a finite work to fracture.

We have discussed a number of issues associated with modeling fracture using cohesive methods. First, we have presented a formulation for cohesive surfaces as a method for physically separating the evolution of fracture processes from the response of the bulk material. We have considered two methods for applying the cohesive surface approach. Following the work of Xu and Needleman[95], we studied the capabilities of the cohesive surface network approach. We have also taken advantage of the inherent adaptivity of meshfree methods to develop a procedure of adaptively inserting cohesive surfaces at arbitrary locations within a meshfree domain. Alternatively, we could have considered adaptive insertion of cohesive surfaces within a finite element setting, as in the work of Ortiz *et al.* [15, 71, 81] We have chosen not to investigate this approach because of the complications associated with adaptively modifying the mesh to account for new fracture surfaces. Also, the direct link between the fracture path and the finite element mesh clouds the distinction between crack behavior and artifacts arising due to restriction of the fracture path to element boundaries. In contrast to the surface approaches, the Virtual Internal Bond (VIB) model embeds cohesive behavior in the bulk constitutive response. The present form of the model lacks an intrinsic length scale. Despite this shortcoming, it still proves to be useful for studying generalized fracture. The model stands alone in providing a means to study the effects of nonlinear elastic response in the near tip region. With the addition of regularization through the incorporation of a theory of strain gradient elasticity, the model will provide a means for studying nonlocal effects in fracture processes.

We have considered a number of cohesive approaches because no approach has proved itself best-suited for all applications. Even with further development, we expect that the most appropriate method for modeling fracture in a particular case will depend on factors like expectations of the fracture path, the size of the structure and its relation to the size of the cracks that form, the rate of loading, and the stability of the cracks during growth. Unless the structures are small compared with the dimensions of the fracture process zone, cohesive surface approaches are the natural choice for modeling failure of interfaces or other cases in which the fracture path is known *a priori*. These cases would include modeling of intergranular fracture in polycrystalline materials. For these cases, the compliance introduced by inserting cohesive surfaces in the initial geometry is less significant and is not linked to refinement of the bulk mesh. Our three-dimensional study of fracture in a slender double-cantilever beam specimen demonstrates the capability of cohesive approaches to respond to local changes in the energy release rate along the crack front "automatically", requiring only that the cohesive tractions are well resolved by the size of the surface elements in the fracture process zone.

As the fracture path becomes less certain, so does the choice of the most appropriate modeling method. In this study, we have demonstrated that artifacts of the mesh size and texture inevitably effect the results of calculations using a network of cohesive surfaces. The mesh dependence is pathological. Furthermore, we could not determine values of the fracture parameters and mesh

size that adequately balanced the requirements of mesh resolution and minimal distortion of elastic properties. Adaptively inserting cohesive surfaces eliminates the pathological mesh dependence, but our studies of dynamic fracture indicate that simply activating new cohesive surfaces does not capture the physics governing the behavior of unstable crack growth. Our adaptive crack tip model allows introduction of wavy fracture paths and crack branching, but the conditions leading to these phenomena would need to be set by assumption. Additional scrutiny of "activation criteria" is required in order to assess their physically-based origins and to understand more completely the implications of these modeling assumptions.

With the additional of a regularization term, the VIB model would be appropriate for a wide range of simulations of generalized fracture in brittle materials, although the computational cost of the strain gradient dependence may be restrictive. Our ongoing developments include investigation of this regularization. We have demonstrated the capabilities of the model for predicting the onset of fracture path instabilities and branching. Due to the lack of an intrinsic length scale, we have not attempted to compare the characteristic scale of fracture surface features with those seen in experiments. We consider that a regularized, higher-order gradient or nonlocal bulk constitutive model will be the most appropriate choice in cases for which the scale of the fracture process zone approaches the size of other relevant length scales in the geometry or resulting from the application of boundary conditions. These cases would include fracture in MEM's or other small scale structures, or in cases of dynamic propagation where the highly deformed near tip zone may itself be determining the scale and evolution of processes governing the fracture behavior.

# 6 Continuing developments

In this study, we consider only brittle fracture. Within this scope, a number of developments would provide more insight into the phenomena governing crack propagation under static and dynamic conditions. Further study with additional capabilities of the crack tip model used for adaptive insertion of cohesive surfaces would provide more understanding of the phenomena governing the propagation of cracks under mixed-mode loading conditions. We have presented a number of criteria for initiating the failure mode. These include a critical hoop stress, a critical traction, and conditions for the emergence of discontinuous bifurcations for cases in which the bulk response exhibits "softening". We have not compared in detail which of these conditions predicts fracture paths that match experimental observations for specific materials. Under dynamic conditions, the adaptive crack tip model could also reveal the driving forces behind the development of wavy fracture paths, crack branching, and the terminal velocity of cracks propagating under unstable loading conditions.

Formulation of an intrinsic length scale for the Virtual Internal Bond (VIB) model has already been initiated by Gao *et al.* [35] The regularized model will provide a method to study the contrast between the cohesive surface approximation of fracture with a "cohesive volume" approach. We expect differences to become significant in small scale structures where the fracture process zone and structure size are comparable. This situation applies not only to fracture in MEM's devices, but also to layered, thin firm structures where film thicknesses have already entered the sub-micron regime. The tips of dynamically propagating cracks may be another situation in which the cohesive surface approximation may simply not be capable of reproducing the fracture path instabilities and branching behavior seen in experiments.

For application to more general material systems, additional dissipation mechanisms must be incorporated in the cohesive models. In moving away from a point-singularity model of the crack tip, cohesive models for brittle materials introduce just a single additional parameter, the cohesive strength, a quantity that has not been well-characterized by experimental measurements. Consideration of additional sources of dissipation, such as plasticity, that display a dependence on the level and character of the stress field provide more rigorous tests of the values selected for this parameter. Tvergaard and Hutchinson[89, 90] have studied the interaction of cohesive surface models and plasticity in the bulk. In reality, the dissipation mechanisms are not so clearly separated, and the distinction between plasticity that is considered to be inside and outside of the fracture process zone becomes difficult to establish. Validation of the modeling approach requires comparison against a number of tests with varied loading conditions and specimen geometries. With cohesive modeling, a characteristic length scale also emerges. Rahul-Kumar *et al.* [73] have demonstrated that this characteristic length scale interacts with the size scale of the viscous dissipation zone during fracture of viscoelastic materials. As seen with plasticity, interaction of a cohesive zone characteristic with the dissipation mechanisms of the surrounding material provides more rigorous tests for the modeling procedure. However, clear distinctions between the sources of viscous dissipation either inside or outside of the cohesive zone become difficult to establish.

The study is just the first step toward investigating the features of meshfree methods that make them advantageous for performing numerical simulations of fracture. Since the physics of fracture processes are not yet well understood, a flexible and robust simulation tool with a very general implementation is needed in which physically-based descriptions of the fracture process can be tested against experimental observations under both static and dynamic loading conditions.

Meshfree methods provide a large number of topics that still need further investigation. A list of selected topics that focus directly on simulation of fracture-like behavior are described below:

(1) **Adaptive propagation of cohesive surfaces in a meshfree domain.** One advantage of meshfree approaches is inherent adaptivity of geometry. Displacement discontinuities can be inserted at virtually any location and orientation within the domain. The study extended the usefulness of this characteristic by allowing tractions to be generated across the faces of the discontinuity in order to represent cohesive cracks. Further work is needed to make the implementation of these ideas more robust and general in order to handle multiple, interesting crack surfaces of arbitrary geometry. Implementation of this adaptivity for parallel execution also needs further development.

(2) **Nodal integration schemes.** Integration of the weak statement of the governing equations is performed in the most straightforward manner using numerical integration schemes developed for finite element methods. The resulting implementation may be called "semi-meshfree" because a background integration grid is required although the nodal shape functions depend only on the nodal positions. In order to be "truly meshfree", integration schemes based only on the nodal positions must be used. Nodal integration schemes published in the literature have demonstrated improved performance under extremely large deformations. They should also improve computational efficiency and reduce memory requirements, the latter improvement being especially important on limited memory machines such as the CPLANT's. Nodal adaptivity also becomes much more flexible compared with standard, grid-based integration methods. Finally, nodal integration schemes greatly facilitate the treatment of constitutive models using internal stave variables (ISV). Unlike the nodal degrees of freedom, the ISV's typically exist only at the integration points. Therefore, evaluating the material response at an arbitrary point in the domain would require separate interpolants for the field and ISV's unless the integration points and nodal points coincide.

(3) **Multi-scale methods.** The formulation of the Reproducing Kernel Particle Method (RKPM) naturally produces a multi-scale decomposition of the displacement field, that is, a decomposition into coarse and fine scale displacement features. Application of this decomposition for studying problems involving strain localization has just emerged as topic of research in the meshfree community. At the least, this decomposition provides a means in a nodal adaptivity scheme for identifying regions requiring higher densities of particles. Ultimately, this decomposition could provide a way in which localized deformation becomes regularized with the application of appropriate fine scale constitutive models in a completely "automatic" fashion. For a fracture modeling, this implies embedding cohesive behavior within simulation without needing to explicitly track propagating crack surfaces.

(4) **Contact and meshfree methods.** Under conditions of mixed-mode loading or in situations of fragmentation, fracture is often accompanied by contact. In principal, contact algorithms from standard finite element methods should also be applicable to meshfree methods. In practice, the implementation of contact algorithms will have to account for significant differences arising from a meshfree description. Key among these differences is the nonlocal character of the nodal shape functions and their lack of the so-called Kronecker delta property. This characteristic affects the imposition of essential boundary conditions and has broad implications for the treatment of contact.

(5) **Parallel scalability.** The greater degree of overlap in the supports of the nodal shape functions of meshfree methods compared with finite element methods implies increased volume of communication for parallel execution. In order to achieve optimal scalability, communication and calculation must be overlapped. Due to a lack of stability with the early versions of MPI on the CPLANT's, this strategy was not used in the current implementation. Taking full advantage of overlap requires changing the sequence calculations. Delocalizing the communication phase also requires more careful structuring of the code to handle exceptional cases that may arise during the calculation phase.

(6) **Mass lumping and accuracy/consistency issues for explicit dynamics.** Currently, explicit dynamic calculations with meshfree techniques make use of mass lumping methods developed for finite element methods. These have not been proven to be optimal in terms of accuracy or consistency.

(7) **Meshfree methods in SIERRA.** Ultimately, meshfree methods will be incorporated into the SIERRA framework. As mentioned above, a number of differences between meshfree methods and standard finite element methods raise issues in a framework that attempts to support both.

# A Preliminaries

In this section, we briefly introduce selected concepts from the mechanics of a continuum subject to finite deformations. The opening section introduces measures of deformation. A section outlining Green elastic theory. This theory serves as the basis for the Virtual Internal Bond model presented in Section 2.2. This section also presents the relations between various stress and modulus arising under finite deformations. The final section presents the governing equations for the initial, boundary value problems that serve as the framework for numerical examples presented in Section 4. These concept will be used throughout the discussions in this study.

## A.1 Kinematics of deformation

In the hyperelastic theory of continuum mechanics[67, 63], material points in the undeformed configuration are described by their reference (Lagrangian) coordinates $\mathbf{X} = (X_1, X_2, X_3)$, while points in the deformed body are described by spatial (Eulerian) coordinates $\mathbf{x} = (x_1, x_2, x_3)$. Throughout this discussion, we will make use of the convention that upper case variables refer to quantities in their material representation, while lowercase variables refer to the corresponding spatial representations. The motion of a point $X_I$ in the Lagrangian coordinates to a point $x_i$ in Eulerian coordinates is described by the motion

$$\mathbf{x}(\mathbf{X}, t) = \boldsymbol{\varphi}(\mathbf{X}, t)\,. \tag{A.1}$$

Using the motion (A.1), we can describe the deformation of a small fiber $d\mathbf{X}$ emanating from the material point $\mathbf{X}$. The deformed vector $d\mathbf{x}$ can be approximated with a Taylor expansion

$$\begin{aligned} d\mathbf{x} &= \boldsymbol{\varphi}(\mathbf{X} + d\mathbf{X}, t) - \boldsymbol{\varphi}(\mathbf{X}, t) \\ &= \left[\boldsymbol{\varphi}(\mathbf{X}, t) + \frac{\partial \boldsymbol{\varphi}(\mathbf{X}, t)}{\partial \mathbf{X}}\, d\mathbf{X} + \frac{1}{2}\, d\mathbf{X} \cdot \frac{\partial^2 \boldsymbol{\varphi}(\mathbf{X}, t)}{\partial \mathbf{X}^2}\, d\mathbf{X} + \dots\right] - \boldsymbol{\varphi}(\mathbf{X}, t)\,. \end{aligned} \tag{A.2}$$

Neglecting higher order terms in (A.2), the vector $d\mathbf{X}$ is mapped to its deformed configuration by

$$d\mathbf{x}(\mathbf{X}, t) = \mathbf{F}(\mathbf{X}, t)\, d\mathbf{X}, \tag{A.3}$$

where we have defined the deformation gradient $\mathbf{F}$ as

$$F_{iI}(\mathbf{X}, t) = \frac{\partial \varphi_i(\mathbf{X}, t)}{\partial X_I}. \tag{A.4}$$

The length of the deformed vector $d\mathbf{x}$ is

$$dx = \sqrt{d\mathbf{X} \cdot \mathbf{F}^{\mathrm{T}}\mathbf{F}\, d\mathbf{X}}, \tag{A.5}$$

which gives rise to the definition of the right Cauchy-Green stretch tensor

$$\mathbf{C} = \mathbf{F}^{\mathrm{T}}\mathbf{F}. \tag{A.6}$$

By expressing $d\mathbf{X}$ in terms of its length $dX$ and direction $\boldsymbol{\Xi}$, the deformed length can be written as

$$dx = dX\, \sqrt{\boldsymbol{\Xi} \cdot \mathbf{C}\, \boldsymbol{\Xi}}, \tag{A.7}$$

where the direction $\boldsymbol{\Xi}$ in two dimensions may be represented in polar coordinates as

$$\boldsymbol{\Xi}(\phi) = \begin{Bmatrix} \cos\phi \\ \sin\phi \end{Bmatrix} \qquad (-\pi \leq \phi \leq \pi)\,, \tag{A.8}$$

and in three dimensions using spherical coordinates as

$$\boldsymbol{\Xi}(\theta,\phi) = \begin{Bmatrix} \sin\theta\,\cos\phi \\ \sin\theta\,\sin\phi \\ \cos\theta \end{Bmatrix} \qquad (0 \leq \theta \leq \pi, -\pi \leq \phi \leq \pi)\,. \tag{A.9}$$

From a spatial description, we can map an infinitesimal vector back to its corresponding undeformed description by inverting (A.3) to give

$$d\mathbf{X}(\mathbf{x},t) = \mathbf{F}^{-1}(\mathbf{x},t)\,d\mathbf{x}. \tag{A.10}$$

The expression for the original length of $d\mathbf{x}$,

$$dX = \sqrt{d\mathbf{x}\cdot\mathbf{F}^{-\mathrm{T}}\mathbf{F}^{-1}\,d\mathbf{x}}, \tag{A.11}$$

gives rise to the definition of the left Cauchy-Green stretch tensor

$$\mathbf{b} = \mathbf{F}\,\mathbf{F}^{\mathrm{T}}. \tag{A.12}$$

Making use of the polar decomposition of $\mathbf{F}$,

$$\mathbf{F} = \mathbf{R}\,\mathbf{U} = \mathbf{V}\,\mathbf{R}, \tag{A.13}$$

where $\mathbf{R}$ is a proper orthogonal transformation, and $\mathbf{U}$ and $\mathbf{V}$ are symmetric and positive definite, we can derive

$$\mathbf{U} = \mathbf{C}^{1/2}, \qquad \mathbf{V} = \mathbf{b}^{1/2}, \quad \text{and} \qquad \mathbf{U} = \mathbf{R}^{\mathrm{T}}\,\mathbf{V}\,\mathbf{R}. \tag{A.14}$$

From the relations (A.14), we can see that the stretch tensors $\mathbf{C}$ and $\mathbf{b}$ have the same eigenvalues and that their principal directions are related by the rotation $\mathbf{R}$.

## A.2 Green elastic theory

The basic postulate of Green elastic materials is the existence of a strain energy density $\mathcal{W}(\mathbf{F})$ which defines the stress and modulus at a point $\mathbf{X}$ as a function of the local state of deformation. In order to satisfy the requirement for material frame indifference, we limit our discussion to strain energy densities which are expressed as a function of the right stretch $\mathbf{C}$, that is

$$\mathcal{W}(\mathbf{F}) = \Phi(\mathbf{C})\,. \tag{A.15}$$

To illustrate the reason for this choice, we imagine modifying a motion given by $\boldsymbol{\varphi}(\mathbf{X},t)$ with an additional rigid body motion such that the final motion is given by

$$\boldsymbol{\varphi}^{+}(\mathbf{X},t) = \mathbf{g}(t) + \mathbf{r}(t)\;\boldsymbol{\varphi}(\mathbf{X},t)\,. \tag{A.16}$$

where $\mathbf{g}(t)$ represents a rigid body translation, and $\mathbf{r}(t)$ is a rigid body rotation satisfying $\mathbf{r}^{-1} = \mathbf{r}^{\mathrm{T}}$ and $\det[\mathbf{r}(t)] = 1$. We may also interpret this situation as corresponding to observations of the

same deformation from two different material reference frames. The observation of $\boldsymbol{\varphi}^+$ can be thought of as occurring in a reference frame which is translating and rotating with respect to the frame in which we observe $\boldsymbol{\varphi}$. In this second reference frame, the deformation gradient is

$$\mathbf{F}^+ = \mathbf{r}(t)\,\mathbf{F}, \tag{A.17}$$

from which we can see that the right stretch is invariant with respect to the rigid body rotation $\mathbf{r}$ since

$$\mathbf{C}^+ = \left(\mathbf{F}^+\right)^{\mathrm{T}}\mathbf{F}^+ = \mathbf{F}^{\mathrm{T}}\,\mathbf{r}^{\mathrm{T}}\mathbf{r}\,\mathbf{F} = \mathbf{C}. \tag{A.18}$$

As we would expect, the deformation is therefore observed to be the same by observers in either frame.

From the theory of Green elastic materials, the strain energy function $\Phi(\mathbf{C})$ defines the symmetric ($2^{\mathrm{nd}}$) Piola-Kirchhoff stress tensor,

$$S_{IJ} = 2\frac{\partial \Phi}{\partial C_{IJ}}, \tag{A.19}$$

as the work-conjugate of $\mathbf{C}$. The "slope" of the $\mathbf{S}$-$\mathbf{C}$ relationship,

$$\mathsf{C}_{IJKL} = 2\frac{\partial S_{IJ}}{\partial C_{KL}} = 4\frac{\partial^2 \Phi}{\partial C_{IJ}\partial C_{KL}}, \tag{A.20}$$

is the material tangent modulus. Due to the distinction between the reference and current configurations, stress and tangent modulus are not uniquely defined. The asymmetric, $1^{\mathrm{st}}$ Piola-Kirchhoff stress tensor is defined by

$$P_{iJ} = \frac{\partial \mathcal{W}}{\partial F_{iJ}}. \tag{A.21}$$

$\mathbf{P}$ is related to $\mathbf{S}$ by

$$P_{iJ} = F_{iI}S_{IJ}. \tag{A.22}$$

The pair $\{\mathbf{P}, \mathbf{F}\}$, like $\{\mathbf{S}, \mathbf{C}\}$, is work-conjugate in the thermodynamic sense. The "slope" of the $\mathbf{P}$-$\mathbf{F}$ diagram,

$$\mathsf{B}_{iJkL} = \frac{\partial P_{iJ}}{\partial F_{kL}} = \delta_{ik}S_{JL} + \mathsf{C}_{IJKL}F_{iI}F_{kK}, \tag{A.23}$$

is the effective tangent modulus. Note that $\mathsf{B}$, unlike $\mathsf{C}$, does not possess minor symmetry with respect to its indices.

The true (Cauchy) stress tensor $\boldsymbol{\sigma}$ is uniquely determined from the traction vector

$$t_i = n_j\,\sigma_{ji}, \tag{A.24}$$

that represents the force per unit deformed area exerted on a surface element with outward normal $\mathbf{n}$. The stress tensors $\boldsymbol{\sigma}$, $\mathbf{S}$, and $\mathbf{P}$ are related by

$$J\sigma_{ij} = P_{iJ}F_{jJ} = F_{iI}S_{IJ}F_{jJ}, \tag{A.25}$$

where

$$J = \det \mathbf{F} \tag{A.26}$$

is the Jacobian determinant of deformation. Admissible states of deformation are those for which $J > 0$, meaning we do not admit deformations which "fold" the continuum over, or through, itself. The corresponding "stiffness"

$$\mathsf{c}_{ijkl} = \frac{1}{J} F_{iI} F_{jJ} F_{kK} F_{lL} \mathsf{C}_{IJKL} \tag{A.27}$$

is the spatial tangent modulus.

## A.3 Governing equations

For the simulations presented in Section 4, we solve initial boundary value problems in finite deformation elastostatics and dynamics. In its Lagrangian representation, the governing equation of elastodynamics at finite deformations is

$$\frac{\partial \mathbf{P}(\mathbf{X}, t)}{\partial \mathbf{X}} + \rho_0 \mathbf{B}(\mathbf{X}, t) = \rho_0 \frac{\partial^2 \mathbf{u}(\mathbf{X}, t)}{\partial t^2}, \tag{A.28}$$

where $\mathbf{B}$ is the body force per unit undeformed volume, $\rho_0$ is the density of the undeformed material. A plane wave propagating through the continuum is described by

$$\mathbf{u}(\mathbf{X}, t) = \mathbf{a} \exp[ik(\mathbf{N} \cdot \mathbf{X} - c\,t)], \tag{A.29}$$

where $\mathbf{u}$ is the displacement of a material particle, $i$ is $\sqrt{-1}$ in (A.29) only, $k$ is the wave number, $c$ is the wave speed, and $\mathbf{N}$ is a vector in the propagation direction defined in the reference configuration. Inserting the plane wave description (A.29) into the equation of motion (A.28) in the absence of body forces yields

$$\left[\mathbf{q}(\mathbf{N}) - \rho_0 c^2 \mathbf{1}\right] \mathbf{a} = 0, \tag{A.30}$$

where

$$q_{ik}(\mathbf{N}) = \mathsf{B}_{iJkL} N_J N_L \tag{A.31}$$

is the acoustical tensor. Nontrivial solutions of (A.30) require that the determinant of the coefficient matrix of $\mathbf{a}$ vanish, yielding the characteristic bulk wave speeds from the eigenvalues of $\mathbf{q}(\mathbf{N})$. The classical condition for strain localization states that the acoustical tensor $\mathbf{q}(\mathbf{N})$ is singular for a particular choice of $\mathbf{N}$, which then defines the normal to the surface across which a discontinuity appears. This result can be derived by admitting a deformation field containing a jump in the velocity gradient as with acceleration waves[40, 88], or by admitting a jump in the displacement field[3]. Though the details of the analyses differ, the result in these, and many other examples, is the same: the loss of positive definiteness of the acoustical tensor marks the bifurcation of the solution from a smooth field to a solution admitting discontinuous features.

## References


[1] F.F. Abraham, *On the transition from brittle to plastic failure in breaking a nanocrystal under tension (NUT)*, Europhysics Letters **38** (1997), 103–106.

[2] F.F. Abraham, D. Brodbeck, R.A. Rafey, and W.E. Rudge, *Instabilities dynamics of fracture: a computer simulation investigation*, Physics Review Letters **73** (1994), 272–275.

[3] F. Armero and K. Garikipati, *Analysis of strong discontinuities in multiplicative finite strain plasticity and their relation with numerical simulation of strain localization in solids*, International Journal of Solids and Structures **33** (1996), 2863–2885.

[4] S. Atluri and T. Zhu, *A new meshless local Petrov-Galerkin approach in computational mechanics*, Computational Mechanics **22** (1998), 117–127.

[5] A.I. Bailey and S.M. Kay, *A direct measurement of the influence of vapour, of liquid, and of oriented monolayers on the interfacial energy of mica*, Proceedings of the Royal Society of London **A301** (1967), 1464.

[6] G.I. Barenblatt, *The formation of equilibrium cracks during brittle fracture: general ideas and hypotheses, axially symmetric cracks*, Applied Mathematics and Mechanics (PMM) **23** (1959), 622–636.

[7] R.J. Bazzard, B. Gross, and J.E. Srawley, *Mode II fatigue crack growth specimen*, ASTM STP **906** (1986), 329–346.

[8] S. Beissel and T. Belytschko, *Nodal integration of the element-free Galerkin method*, Computer Methods in Applied Mechanics and Engineering **139** (1996), 49–74.

[9] T. Belytschko, Y. Krongauz, D. Organ, M. Fleming, and P. Krysl, *Meshless methods: an overview and recent developments*, Computer Methods in Applied Mechanics and Engineering **139** (1996), 3–47.

[10] T. Belytschko, Y.Y. Lu, and L. Gu, *Element-free Galerkin methods*, International Journal for Numerical Methods in Engineering **37** (1994), 229–256.

[11] T. Belytschko, Y.Y. Lu, L. Gu, and M.R. Tabbara, *Element-free Galerkin methods for static and dynamic fracture*, International Journal of Solids and Structures **17** (1995), 186–195.

[12] T. Belytschko, D. Organ, and Y. Krongauz, *A coupled finite-element, element-free Galerkin method*, Computational Mechanics **17** (1995), 186–195.

[13] T. Belytschko and M.R. Tabbara, *Dynamic fracture using element-free Galerkin methods*, International Journal for Numerical Methods in Engineering **39** (1996), 923–938.

[14] P.J. Bryant, L.H. Taylor, and P.L. Guthshall, *Cleavage studies of lamellar solids in various gas environments*, Transactions of the 10th National Vacuum Symposium, 1963.

[15] G.T. Camacho and M. Ortiz, *Computational modeling of impact damage in brittle materials*, International Journal of Solids and Structures **33** (1996), 2899–2938.

[16] ———, *Adaptive Lagrangian modelling of ballistic penetraction of metallic targets*, Computer Methods in Applied Mechanics and Engineering **142** (1997), 269–301.

[17] J.S. Chen, C. Pan, C.T. Wu, and W.K. Liu, *Reproducing kernel particle methods for large deformation analysis of nonlinear structures*, Computer Methods in Applied Mechanics and Engineering **139** (1996), 195–227.

[18] J.S. Chen, C.T. Wu, and S. Yoon, *Nonlinear version of stabilized conforming nodal integration for Galerkin meshfree methods*, International Journal of Numerical Methods in Engineering (2000), submitted for publication.

[19] J.S. Chen, C.T. Wu, S. Yoon, and Y. You, *A stabilized conforming nodal integration for Galerkin meshfree methods*, International Journal of Numerical Methods in Engineering (2000), accepted for publication.

[20] W.N. Chen and G. Ravichandran, *Dynamic compressive behavior of ceramics under lateral confinement*, Journal of Physics **4** (1994), 177–182.

[21] ———, *Static and dynamic compressive behavior of aluminum nitride under moderate confinement*, Journal of the American Ceramic Society **79** (1996), 579–584.

[22] F Costanzo and J.R. Walton, *A study of dynamic crack growth in elastic materials using a cohesive zone model*, International Journal of Engineering Sciences **35** (1997), 1085–1114.

[23] J. Dolbow and T. Belytschko, *Numerical integration of the Galerkin weak form in meshfree methods*, Computational Mechanics **23** (1999), 219–230.

[24] D.S. Dugdale, *Yielding of steel sheets containing slits*, Journal of the Mechanics and Physics of Solids **8** (1960), 100–104.

[25] F. Erdogan and G.C. Sih, *On the crack extension in plates under plane loading and transverse shear*, ASME Journal of Basic Engineering **85** (1963), 519–527.

[26] J.D. Eshelby, *Inelastic behavior of solids*, McGraw-Hill, New York, 1970.

[27] J. Fineberg, S.P. Gross, M. Marder, and H.L. Swinney, *Instability in dynamic fracture*, Physical Review Letters **67** (1991), 457–460.

[28] ———, *Instability in the propagation of fast cracks*, Physical Review B **45** (1992), 5146–5154.

[29] B. Freund, *Dynamic fracture mechanics*, Cambridge University Press, New York, 1990.

[30] H. Gao, *Surface roughening and branching instabilities in dynamic fracture*, Journal of the Mechanics and Physics of Solids **41** (1993), 457–486.

[31] ———, *A theory of local limiting speed in dynamic fracture*, Journal of the Mechanics and Physics of Solids **44** (1996), 1453–1474.

[32] ———, *Elastic waves in a hyperelastic solid near its plane strain equibiaxial cohesive limit*, Philosophical Magazine Letters **76** (1997), 307–314.

[33] H. Gao and C.-H. Chiu, *Slightly curved or kinked cracks in anisotropic elastic solids*, Journal of the Mechanics and Physics of Solids **29** (1992), 947–972.

[34] H. Gao and P. Klein, *Numerical simulation of crack growth in an isotropic solid with randomized internal cohesive bonds*, Journal of the Mechanics and Physics of Solids **46** (1998), 187–218.

[35] H. Gao, A. Vainchtein, P.A. Klein, and E.P. Chen, *Introducing a length scale into modeling of fracture via a strain-gradient elasticity theory*, Advances in Computational Engineering and Sciences (S.N. Atluri and F.W. Brust, eds.), International Conferences on Computational Engineering and Sciences, 2000, pp. 1766–1771.

[36] R.A. Gingold and J.J. Monaghan, *Smoothed particle hydrodynamics: theory and application to non-spherical stars*, Monthly Notices of the Royal Astronomical Society **181** (1977), 375–389.

[37] A.A. Griffith, *The phenomena of rupture and flow in solids*, Philosophical Transactions **221** (1920), 163–198.

[38] A.L. Gurson, *Continuum theory of ductile rupture by void nucleation and growth: PART I*, Journal of Engineering Materials and Technology **99** (1977), 2–15.

[39] J.C. Hill, J.W. Foulk, P.A. Klein, and E.P. Chen, *A three-dimensional validation of crack curvature in muscovite mica*, Proceedings of the 10th International Conference of IACMAG, 2000.

[40] R. Hill, *Acceleration waves in solids*, Journal of the Mechanics and Physics of Solids **10** (1962), 1–16.

[41] G.R. Irwin, *Analysis of stresses and strains near the end of a crack traversing a plate*, Journal of Applied Mechanics **24** (1957), 361–364.

[42] M. Kachanov, *Effective elastic properties of cracked solids: critical review of some basic concepts*, Applied Mechanics Review **45** (1992), 304.

[43] J.F. Kalthoff and S. Winkler, *Failure mode transition at high rates of shear loading*, International Conference on Impact Loading and Dynamic Behavior of Materials (C.Y. Chiem, H.D. Kunze, and L.W. Meyer, eds.), 1987, pp. 185–195.

[44] P.N.R. Keegstra, *A transient finite element crack propagation method for nuclear pressure vessels steels*, Journal of the Institution of Nuclear Engineers **17** (1976), 89–96.

[45] P. Klein and H. Gao, *Crack nucleation and growth as strain localization in a virtual-bond continuum*, Engineering Fracture Mechanics **61** (1998), 21–48.

[46] P.A. Klein, *A virtual internal bond approach to modeling crack nucleation and growth*, Ph.D. thesis, Stanford University, 1999.

[47] P.A. Klein and H. Gao, *Study of crack dynamics using the Virtual Internal Bond model*, James R. Rice $60^{\text{th}}$ Anniversary Volume of Solid Mechanics and its Applications (G.M.L. Gladwell, ed.), Kluwer Academic Publishers, in press.

[48] W.G. Knauss and G.U. Losi, *Crack propagation in a nonlinearly viscoelastic solid with relevance to adhesive bond failure*, Journal of Applied Mechanics **60** (1993), 793–801.

[49] A.S. Kobayashi, A.F. Emery, and S. Mall, *Dynamic finite element and photoelastic analyses of two fracture Homalite-100 plates*, Experimental Mechanics **16** (1976), 321–328.

[50] P. Krysl and T. Belytschko, *Element-free Galerkin method: convergence of the continuous and discontinuous shape functions*, Computer Methods in Applied Mechanics and Engineering **148** (1997), 257–277.

[51] ———, *The element free Galerkin method for dynamic propagation of arbitrary 3-D cracks*, International Journal of Numerical Methods in Engineering **44** (1999), 767–800.

[52] P. Lancaster and K. Salkauskas, *Surfaces generated by moving least squares methods*, Mathematics of Computation **37** (1981), 141–158.

[53] Y. Lee and V. Prakash, *Dynamic brittle fracture of high strength structural steels under conditions of plane strain*, International Journal of Solids and Structures **36** (1999), 3293–3337.

[54] S. Li, W. Hao, and W.K. Liu, *Mesh-free simulations of shear banding in large deformation*, International Journal of Solids and Structures **37** (2000), 7185–7206.

[55] S. Li and W.K. Liu, *Synchronized reproducing kernel interpolant via multiple wavelet expansion*, Computational Mechanics **21** (1998), 28–47.

[56] W.K. Liu and Y. Chen, *Reproducing kernel particle methods*, International Journal for Numerical Methods in Fluids **20** (1995), 1081–1106.

[57] ———, *Wavelet and multiple scale reproducing kernel method*, International Journal for Numerical Methods in Fluids **21** (1995), 901–931.

[58] W.K. Liu, Y. Chen, C.T. Chang, and T. Belytschko, *Advances in multiple scale kernel particle methods*, Computational Mechanics **18** (1996), 73–111.

[59] W.K. Liu, Y. Chen, R.A. Uras, and C.T. Chang, *Generalized multiple scale reproducing kernel particle methods*, Computer Methods in Applied Mechanics and Engineering **139** (1996), 91–158.

[60] W.K. Liu, S. Hao, T. Belytschko, S. Li, and C.T. Chang, *Multiple scale meshfree methods for damage fracture and localization*, Computational Materials Science **16** (1999), 197–205.

[61] ———, *Multi-scale methods*, International Journal for Numerical Methods in Engineering **47** (2000), 1343–1361.

[62] Y.Y. Lu, T. Belytschko, and M.R. Tabbara, *Element-free Galerkin methods for wave propagation and dynamic fracture*, Computer Methods in Applied Mechanics and Engineering **126** (1995), 131–153.

[63] J. E. Marsden and T. J. R. Hughes, *Mathematical foundations of elasticity*, Dover Publications, Inc., New York, 1983.

[64] L.E. McNeil, *Elastic moduli of muscovite mica*, Journal of Physics: Condensed Matter **5** (1993), 1681–1690.

[65] B. Nayroles, G. Touzot, and P. Villon, *Generalizing the finite element method: Diffuse approximation and diffuse elements*, Computational Mechanics **10** (1992), 307–318.

[66] J.W. Obreimoff, *The splitting strength of mica*, Proceedings of The Royal Society of London **A215** (1930), 905.

[67] R.W. Ogden, *Non-linear elastic deformations*, John Wiley and Sons, Inc., New York, 1984.

[68] D. Organ, T. Fleming, T. Terry, and T. Belytschko, *Continuous meshless approximations for nonconvex bodies by diffraction and transparency*, Computational Mechanics **18** (1996), 1–11.

[69] E. Orowan, *Fracture and strength of solids*, Reports on Progress in Physics **XII** (1948), 185.

[70] M. Ortiz and A. Pandolfi, *Finite-deformation irreversible cohesive elements for three-dimensional crack-propagation analysis*, International Journal for Numerical Methods in Engineering **44** (1999), 1267–1282.

[71] A. Pandolfi, P. Krysl, and M. Ortiz, *Finite element simulation of ring expansion and fragmentation: The capturing of length and time scales through cohesive models of fracture*, International Journal of Fracture **95** (1999), 279–297.

[72] L. Prandtl, *Ein Gedankenmodell für den Zerreißvorgang spröder Körper*, Zeitschrift für angewandte Mathematik und Mechanik **13** (1933), 129–133.

[73] P. Rahul-Kumar, A. Jagota, S.J. Benison, and S. Saigal, *Cohesive modeling of viscoelastic fracture: Application to peel testing of polymers*, International Journal of Solids and Structures **37** (2000), 1873–1897.

[74] K. Ravi-Chandar, *Dynamic fracture of nominally brittle materials*, International Journal of Fracture **90** (1998), 83–102.

[75] K. Ravi-Chandar and W.G. Knauss, *An experimental investigation into dynamic fracture: I. crack initiation and arrest*, International Journal of Fracture **25** (1984), 247–262.

[76] ———, *An experimental investigation into dynamic fracture: II. microstructural aspects*, International Journal of Fracture **26** (1984), 65–80.

[77] ———, *An experimental investigation into dynamic fracture: III. on steady state propagation and branching*, International Journal of Fracture **26** (1984), 141–154.

[78] ———, *An experimental investigation into dynamic fracture: IV. on the interaction of stress waves with propagating cracks*, International Journal of Fracture **26** (1984), 189–200.

[79] J.R. Rice, *A path independent integral and the approximate analysis of stress concentration by notches and cracks*, Journal of the Mechanics and Physics of Solids **40** (1968), 939–963.

[80] J.H. Rose, J. Ferrante, and J.R. Smith, *Universal binding energy curves for metals and bimetallic interfaces*, Physical Review Letters **47** (1981), 675–678.

[81] G. Ruiz, M. Ortiz, and A. Pandolfi, *Three-dimensional finite-element simulation of the dynamic Brazilian tests on concrete cylinders*, International Journal for Numerical Methods in Engineering **48** (2000), 963–994.

[82] G. Rydholm, B. Fredriksson, and F. Nilsson, *Numerical investigation of rapid crack propagation*, Numerical Methods in Fracture Mechanics (A.R. Luxmoore and D.J.R. Owen, eds.), Pineridge Press, 1978, pp. 660–672.

[83] T. Siegmund, N.A. Fleck, and A. Needleman, *Dynamic crack growth across an interface*, International Journal of Fracture **85** (1997), 381–402.

[84] J.C. Simo, R.L. Taylor, and K.S. Pister, *Variational and projection methods for the volume constraint in finite deformation elastoplasticity*, Computer Methods in Applied Mechanics and Engineering **51** (1995), 177–208.

[85] C.W. Smith and S.J. Wiersma, *Stress-fringe signatures for a propagating crack*, Engineering Fracture Mechanics **23** (1986), 229–236.

[86] I. Stakgold, *The Cauchy relations in a molecular theory of elasticity*, Quarterly of Applied Mechanics **8** (1950), 169–186.

[87] E.B. Tadmor, M. Ortiz, and R. Phillips, *Quasicontinuum analysis of defects in solids*, Philosophical Magazine A **73** (1996), 1529–1563.

[88] C. Truesdell and W. Noll, *The nonlinear field theories of mechanics*, Handbuch der Physik, Band iii/3 (S. Flügge, ed.), Springer-Verlag, Berlin, 1965.

[89] V. Tvergaard and J.W. Hutchinson, *The relation between crack growth resistance and fracture process parameters in elastic-plastic solids*, Journal of the Mechanics and Physics of Solids **40** (1992), 1377–1397.

[90] ———, *The influence of plasticity on mixed mode interface toughness*, Journal of the Mechanics and Physics of Solids **41** (1993), 1119–1135.

[91] K.T. Wan, S. Lathabai, and B.R. Lawn, *Crack velocity functions and thresholds in brittle solids*, Journal of the European Ceramic Society **6** (1990), 259–268.

[92] K.T. Wan, B.R. Lawn, and R.G. Horn, *Repulsive interaction between coplanar cracks in the double-cantilever geometry*, Journal of Materials Research **7** (1992), 1584–1588.

[93] J.R. Willis, *A comparison of the fracture criteria of Griffith and Barenblatt*, Journal of the Mechanics and Physics of Solids **15** (1967), 151–162.

[94] Z.C. Xia and J.W. Hutchinson, *Crack tip fields in strain gradient plasticity*, Journal of the Mechanics and Physics of Solids **44** (1996), 1621–1648.

[95] X.-P. Xu and A. Needleman, *Numerical simulations of fast crack growth in brittle solids*, Journal of the Mechanics and Physics of Solids **42** (1994), 1397–1434.

[96] ———, *Numerical simulations of crack growth along an interface*, International Journal of Fracture **74** (1996), 289–324.

[97] E.H. Yoffe, *The moving Griffith crack*, Philosophical Magazine **42** (1951), 739–750.

[98] C. Yoon and D.H. Allen, *Damage dependent constitutive behavior and energy release rate for a cohesive zone in a thermoviscoelastic solid*, International Journal of Fracture **96** (1999), 55–74.

# C DISTRIBUTION:

| | | |
|---|---|---|
| 1 | MS 0819 | K.H. Brown, 9231 |
| 1 | | J.R. Weatherby, 9231 |
| 1 | MS 0826 | W.L. Hermina, 9113 |
| 1 | MS 0826 | H.C. Edwards, 9131 |
| 1 | | J.R. Stewart, 9131 |
| 1 | | J.D. Zepper, 9131 |
| 1 | MS 0835 | K.E. Casteel, 9121 |
| 1 | | J.S. Peery, 9121 |
| 1 | | K.H. Pierson, 9121 |
| 1 | MS 0836 | J.H. Biffle, 9121 |
| 1 | MS 0841 | T.C. Bickel, 9100 |
| 1 | MS 0847 | S.W. Attaway, 9121 |
| 1 | | M.K. Bhardwaj, 9121 |
| 1 | | M.L. Blanford, 9121 |
| 1 | | B.J. Driessen, 9121 |
| 1 | | A.S. Gullerud, 9121 |
| 1 | | M.W. Heinstein, 9121 |
| 1 | | S.W. Key, 9121 |
| 1 | | J.R. Koteras, 9121 |
| 1 | | J.A. Mitchell, 9121 |
| 1 | | V.L. Porter, 9121 |
| 1 | | T.J. Preston, 9121 |
| 1 | | G.M. Reese, 9121 |
| 1 | | C.M. Stone, 9121 |
| 1 | | J.W. Swegle, 9121 |
| 1 | MS 0847 | J.B. Aidun, 9123 |
| 1 | | J.M. Caruthers, 9123 |
| 1 | | R.S. Chambers, 9123 |
| 1 | | A.F. Fossum, 9123 |
| 1 | | D.C. Hammerand, 9123 |
| 1 | | S.C. Hwang, 9123 |
| 1 | | C.S. Lo, 9123 |
| 1 | | H.S. Morgan, 9123 |
| 1 | | M.K. Nielsen, 9123 |
| 1 | | E.D. Reedy, 9123 |
| 1 | | W.M. Scherzinger, 9123 |

| | | |
|---|---|---|
| 1 | | W. Wellman, 9123 |
| 1 | MS 0889 | S.J. Glass, 1843 |
| 1 | MS 1111 | G.S. Heffelfinger, 9235 |
| 1 | | M.J. Stevens, 9235 |
| 1 | MS 1349 | J.G. Curro, 1834 |
| 1 | MS 1411 | H.E. Fang, 1834 |
| 1 | | S.M. Foiles, 1834 |
| 1 | | E.A. Holm, 1834 |
| 1 | | J.J. Hoyt, 1834 |
| 1 | | V. Tikare, 1834 |
| 1 | MS 1415 | J.E. Houston, 1114 |
| 1 | MS 9001 | M.E. John, 8000<br>Attn:<br>R.C. Wayne, 2200, MS 9005<br>J. Vitko, 8100, MS 9004<br>W.J. McLean, 8300, MS 9054<br>D.R. Henson, 8400, MS 9007<br>P.N. Smith, 8500, MS 9002<br>K.E. Washington, 8900, MS 9003 |
| 1 | MS 9042 | B.R. Antoun, 8725 |
| 1 | | D.B. Dawson, 8725 |
| 1 | | S. Graham Jr., 8725 |
| 1 | MS 9042 | M.L. Chiesa, 8727 |
| 1 | | J.A. Crowell, 8727 |
| 1 | | J.J. Dike, 8727 |
| 1 | | J.L. Handrock, 8727 |
| 1 | | Y.R. Kan, 8727 |
| 1 | | B.L. Kistler, 8727 |
| 1 | | J.P. Laufer, 8727 |
| 1 | | R. Ortega, 8727 |
| 1 | | V.D. Revelli, 8727 |
| 1 | | R.A. Radovitzky, 8727 |
| 1 | | J.E. Robles, 8727 |
| 1 | | A.M. Siebler, 8727 |
| 1 | | L.E. Voelker, 8727 |
| 1 | | S. Wu, 8727 |

| | | |
|---|---|---|
| 1 | MS 9108 | S.L. Robinson, 8414 |
| 1 | MS 9161 | E.P. Chen, 8726 |
| 15 | | P.A. Klein, 8726 |
| 1 | | J.A. Zimmerman, 8726 |
| 1 | MS 9161 | J.C. Hamilton, 8721 |
| 1 | | D.L. Medlin, 8721 |
| 1 | | A.K. Schmid, 8721 |
| 1 | MS 9401 | R. Shediac, 8729 |
| 1 | MS 9402 | L.A. Domeier, 8722 |
| 1 | MS 9402 | D.F. Cowgill, 8724 |
| 1 | | B.P. Somerday, 8724 |
| 1 | MS 9403 | N.Y.C. Yang, 8723 |
| 1 | MS 9404 | N.R. Moody, 8725 |
| 1 | | S.H. Goods, 8725 |
| 1 | MS 9405 | T.M. Dyer, 8000<br>Attn:<br>R.Q. Hwang, 8721, MS 9161<br>K.L. Wilson, 8722, MS 9402<br>J.C.F. Wang, 8723, MS 9403<br>G.J. Thomas, 8724, MS 9402<br>W.A. Kawahara, 8725, MS 9042<br>J.L. Handrock, 8727, MS 9042<br>M.W. Perra, 8728, MS 9042<br>J.M. HRuby, 8702, MS 9401 |
| 1 | MS 9405 | D.J. Bammann, 8726 |
| 10 | | J.W. Foulk, 8726 |
| 1 | | Y. Hammi, 8726 |
| 1 | | M.F. Horstemeyer, 8726 |
| 1 | | D.A. Hughes, 8726 |
| 1 | | R.E. Jones, 8726 |
| 1 | | M.T. Lyttle, 8726 |
| 1 | | E.B. Marin, 8726 |
| 1 | | R.A. Regueiro, 8726 |
| 1 | MS 9405 | Y. Ohashi, 8727 |

| | | |
|---|---|---|
| 3 | MS 9018 | Central Technical Files, 8940-2 |
| 1 | MS 0899 | Technical Library, 4916 |
| 1 | MS 9021 | Technical Communications Dept., 8815 |
| 1 | MS 9021 | Technical Communications Dept., 8815 for DOE/OSTI |